The role of Resistivity on the efficiency of Magnetic Reconnection in MHD

Master Thesis in Space Physics

by

Judit Pérez-Coll Jiménez

June, 2021

Department of Physics and Technology

University of Bergen

Acknowledgements

This thesis is the result of a two-year study in the Space Plasma Physics Group (SPPG) as a master's student in Space Physics at the University of Bergen, and it wouldn't have been possible without the significant help of a number of people.

First of all, I would like to express special thanks to my supervisor, Paul Tenfjord, for all the time invested in me and this thesis, for always being available when I had doubts, for encouraging me, and for countless other things that made this project very enjoyable for me. I would like to extend my sincere thanks to my co-supervisor, Michael Hesse, for his immense contribution to this thesis, for always making time to resolve our most difficult questions, for his patience, and for making me feel part of the group since the very beginning.

I also wish to thank the whole rest of the SPPG group, especially Cecilia Norgren, Norah Kwagala, Håkon Kolstø, Susanne Spinnangr, Therese Jorgensen, and Hidetaka Kuniyoshi, for all the interest, the discussions, and the tons of advice and comments that I got since I started. Thanks should also go to Tai Phan, Yi-Hsin Liu, Naoki Bessho, Li-Jen Chen, and Shan Wang for listening to my presentations and giving invaluable insight into this work.

I am also grateful to the other master's students in space physics at UiB, especially Amalie and Andreas, who were around during all my master's and, thanks to them, being in the office always meant having someone to talk to. Thanks also to Héctor, for reading all my thesis with interest and correcting all the typos, commas, and repetitive expressions that I had missed.

I'd also like to acknowledge the unwavering support from my international friends: Martin, Ferdinand, Varun, Ole, Simon, Guy and Victor; who arrived in Norway at the same time as me and have been doing their masters in parallel with me for the last two years, sharing much more than the stress for the deadlines, countless study sessions, two cabin trips, and residence. And thanks to my friends from home: Bea, Laia and Marc, for thinking about me and always finding time to videocall or text. Let's not forget about Risa, Aina, Haruki, Nanami, Carola, Svein Erik and Hilde, who helped to make my stay in Norway during my master's an amazing experience.

I also wish to thank my cousins, aunts and uncles for always asking about my master's, and for their willingness to play "Catan" online so often, which made me feel closer to them

even when I had to spend Christmas far from home. And a special mention should also go to Héctor's parents, Paqui and Patricio, for also thinking about me when sending food from home, which was very much appreciated.

Last, but not least, I'd like to thank my parents, Cristina and Octavi, and my sister Mar, for always caring about my well-being and supporting me (or, in the case of my sister, asking for help with her physics/math homework) from home. And I'd like to include my dog, Lin, in this long list of people, since he was my main concern when I started my master's in Norway, and he will not be home anymore when I go back.

Abstract

Magnetic reconnection is a fundamental plasma process, which can explosively convert magnetic energy to particle energy. When reconnection operates, it releases almost all of the energy stored in the magnetic field and accelerates and heats the plasma. The consequences of reconnection depend on the magnetic energy available and the process ability to rapidly release the energy. Thus, the effectiveness of reconnection, which can be quantified by the rate at which energy is converted, is a key factor in understanding consequences and implications of this universal process. It is critical to understand how effective reconnection operates. In this thesis, we investigate how the reconnection rate depends on the resistivity in the system. In our fluid-based scheme, resistivity refers, in simple terms, to the plasmas ability to diffuse across the magnetic field - allowing new magnetic topologies to form. We employ a resistive MHD model to study the fundamental physics of this question and show that, even when inserting very strong resistive spots with varying shapes, there appears to be a maximum rate of reconnection the system can support. In addition, we find that a sub-optimal choice of resistivity magnitude or shape of the resistive spot leads to lower overall reconnection rates. These results imply that the reconnection rate depends significantly on properties of the diffusion region, even if the size of that region is much smaller than the system. This is a new insight, which may be a counterpoint to the assertion that the reconnection rate is independent of the diffusion region physics. We find very strong indications that a maximum reconnection rate exists, and it appears exceedingly likely that this rate limitation is due to larger-scale system properties rather than properties of the diffusion region.

Contents

Chapter 1

Introduction

Magnetic fields are present all around the universe. From planets and stars to galaxies and beyond. Magnetism, along with gravity, is responsible for shaping and controlling the majority of dynamics observed in the cosmos. Magnetic reconnection is a universal process that plays a crucial role in nearly all regimes, by explosively converting magnetic energy to particle energy.

Magnetic fields store and carry energy, and the coupling between plasmas and magnetic fields is the source of many energetic phenomena observed in laboratories, in our magnetosphere and in the cosmos. Magnetic reconnection is the process that facilitates these events, being able to energize plasma at the expense of magnetic energy. Magnetic reconnection is not only considered a possible mechanism for the majority of phenomena exhibiting particle acceleration and heating and large magnetic geometry changes, but it is also responsible for events such as explosive stellar flares, geomagnetic storms and, thus, aurora.

To understand the implications of reconnection, it is critical to understand how effective the process can operate. For instance, a key aspect of space weather lies in the efficiency of solar wind-magnetospheric coupling and the resulting coupling to the ionosphere, which is directly correlated to the reconnection rate of the Earth's dayside magnetopause. Also, this understanding is very important in magnetically confined fusion devices or for identifying reconnection and studying its effects in places where directly measuring magnetic fields is not possible, such as in astrophysical settings [*Cassak et al.*, 2017].

The simplest way of describing magnetic reconnection is given by the model developed by *Sweet* [1958] and *Parker* [1957a]. However, the predicted reconnection rate derived from the Sweet-Parker model, which corresponds to the rate at which magnetic energy is being converted into kinetic energy of the plasma, is too slow to explain the observations. To explain the observation of, for instance, solar flares, the rate should have been orders of magnitudes larger. In the following years, many analytical theories of fast magnetic reconnection were developed to explain the observed behaviour. Today, observations and

numerical simulations in a wide variety of settings suggest that the global rate of magnetic reconnection is approximately 0.1 in normalized units. However, understanding the reason for reconnection to proceed at this rate has been a long-standing problem [*Cassak et al.*, 2017]. The present study uses a MagnetoHydroDynamic (MHD) model to investigate the fundamental physics of this question.

MHD is a proven tool for understanding the physics of magnetic reconnection from a fluid-based perspective. MHD modelling of magnetic reconnection appeared in the 1990s, enabling simulations to reproduce different analytical solutions of fast magnetic reconnection [*Petschek*, 1964; *Sonnerup*, 1970; *Vasyliunas*, 1975]. At the same time, a number of experimental devices for studying magnetic reconnection were built (e.g., Princeton MRX [*Ji et al.*, 2001], UCLA LAPD [*Gekelman et al.*, 2016]). Numerical simulations of high-temperature fusion plasma, solar dynamo generation, solar flare generation, and 3D MHD magnetospheres were used to predict the consequences of magnetic reconnection. Over time, these models have evolved to include more realistic plasma configurations, such as two-fluid effects, and additional terms that contribute to diffusion [*Kuznetsova et al.*, 2007]. Today, fluid-based models can simulate the unified consequence of a solar flare from the Sun to Earth's atmosphere [*Tóth et al.*, 2005, 2012]. Fluid models have had an enormous impact on our understanding of how reconnection shapes space.

The advantage of fluid models is that they are computationally cheap and can be used to simulate the large-scale behaviour of plasma over vast distances. However, kinetic effects beyond two-fluid descriptions cannot be described by fluid models, and other models such as Particle-In-Cell (PIC) simulations can be used for these purposes. These models can treat particle motions of billions of electrons and ions in three dimensions at timescales appropriate to the dynamical behaviour of the plasma. However, due to the enormous computational cost, particle simulations are only practical for limited spatial scales.

The purpose of this thesis is to study how effective the reconnection rate can be in a fluid-based simulation setup with varying magnitudes and shapes of resistivity. Our tool of investigation is a 2.5D (two spatial dimensions [x and z] and three velocity and field dimensions [x,y and z]) resistive MHD simulation.

In nature, reconnection is enabled and facilitated by different forces that represent resistivity. In a resistive MHD scheme, we employ an explicit resistivity, which resembles the physical mechanism that produces diffusion in reality. The ultimate goal of the process, to convert magnetic energy to particle energy, pervades - regardless of the process enabling it. The benefit of resistive MHD is that we can control the magnitude and shape of the diffusion. This enables us to study how the process behaves and resolves different scenarios. We emphasize that, in this framework, we cannot study the details of the diffusion region. Such an analysis requires a particle treatment. However, as it will be shown, we can achieve realistic reconnection rates without considering the details of diffusion. Our novel approach, therefore, allows us to determine how the overall system responds and reconfigures itself based on varying diffusion properties.

This thesis is organized as follows: in Chapter 2, the theoretical background concerning the study is presented. Important concepts such as *plasma* or *magnetic reconnection* are defined, and some processes and environments related to magnetic reconnection are introduced. In this chapter, we also present the field equations and the kinetic theory in order to derive the MHD equations. Next, we talk about some theoretical models of magnetic reconnection, giving special attention to the Sweet-Parker model, which is explained in detail. To end the chapter, the reconnection rate problem is discussed.

Chapter 3 gives a detailed explanation of the simulation used in the present study, including the set-up and the integration method that our code uses to obtain solutions to the MHD equations. We also present the scientific problem and how are we going to approach the analysis.

In Chapter 4, we present our analysis and results. We begin the chapter by discussing one of the runs in detail for the purpose of getting a general overview and understanding of the simulation layout and evolution. Then we move on to the proper study, which is split into two parts. In the first part, we study the impact of the resistivity's magnitude on the effectiveness of magnetic reconnection. In the second part, we study how the shape of the resistivity affects the reconnection rate.

Chapter 5 discusses three different aspects of interest. These are: the scaling relations in MHD, the grid resolution and the time resolution.

In Chapter 6, we summarize the work presented in the thesis and we present a collection of the key findings of our study, and Chapter 7 contains some suggestions for future work.

Chapter 2

Theory and Background

The main goal of this chapter is to give an introduction to magnetic reconnection and MagnetoHydroDynamics (MHD), which will be necessary for understanding our analysis and how we obtained our results. Sections 2.1 and 2.2 introduce some plasma environments and regimes where magnetic reconnection can operate. Sections 2.3 and 2.4 describe the concept of plasma and introduce the main equations that describe its behaviour, as well as some approximations that lead us to the equations that we will be using: the resistive magnetohydrodynamic equations. In section 2.5, the process of magnetic reconnection will be described and some theoretical models will be presented in section 2.6, paying special attention to the Sweet Parker model, which is the simplest way of describing magnetic reconnection. Finally, we will talk about the magnetic reconnection rate problem, which constitutes one of the main motivations for this thesis.

2.1 The Sun and the Solar Wind

The Sun is an ordinary magnetic star of average size in its middle age. In terms of number of atoms, it consists of 91% hydrogen, 8.9% helium, and only 0.1% of it is formed by other elements. These constituents are ionized because nuclear reactions and electrodynamic interactions create temperatures that exceed the binding energies of the atoms.

The Sun's atmosphere is divided into the photosphere, the chromosphere, and the corona. The corona extends beyond the chromosphere and into interplanetary space, reaching the most distant regions of our solar system. This expansion of the corona is called *solar wind* and appears as a way for the Sun to maintain charge neutrality. It can be explained in the following way: at the base of the corona, the temperature reaches about 1.000.000°K. At these temperatures, nearly 50% of the electrons have thermal velocities

that exceed the gravitational escape velocity of the Sun while less than 1% of the ions do. This creates a large electric field that will accelerate the protons outward, causing the expansion [*Parks*, 2004].

The solar wind is a supersonic and fully ionized plasma. Its electron-ion collision frequency is around $10^{-5}Hz$, which means that only one collision or less will occur every day. This is why it is considered a *collisionless* plasma. The solar wind streams away from the sun with velocities of around 500-1500km/s and its electron density and temperature near the Earth are generally around $n_e \approx 5\text{cm}^{-3}$ and $T_e \approx 10^5\text{K}$ [*Parker*, 1958a].

The *Interplanetary Magnetic Field* (IMF), also referred to as the *Heliospheric Magnetic Field* (HMF), is a part of the Sun's magnetic field that is carried into interplanetary space by the solar wind in a radial outflow. The interplanetary magnetic field lines are said to be *frozen in*to the solar wind plasma, meaning that they are closely tied together. Because of the 27-day solar rotation period, the IMF will not maintain the form it had in the solar corona, but will bend into an Archimedean spiral form as shown in Figure 2.1. This is also known as *Parker spiral*. The IMF value near the Earth's orbit ranges from 1 to 20nT, with an average magnitude of about 5nT and a velocity of around 400km/s [*Parker*, 1958b; *Baumjohann and Treumann*, 2012].

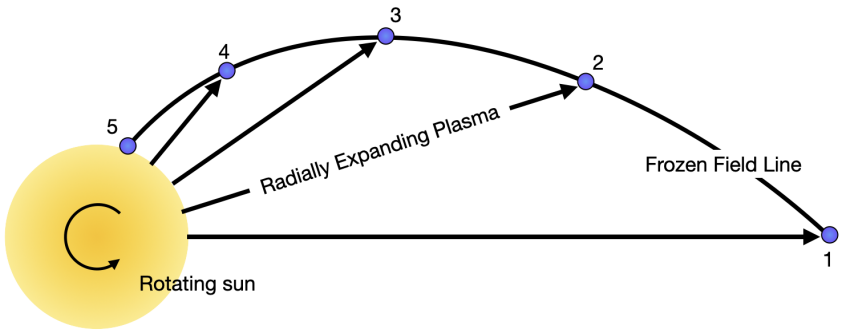

Figure 2.1: Spiral form of an interplanetary field line due to solar rotation.

2.2 The Earth's magnetosphere

According to the dynamo theory, a rotating, convecting and electrically conducting fluid can maintain a magnetic field over astronomical time scales. The Earth rotates once on its axis every 23 hours and 56 minutes, which makes it the most rapid rotator of the inner planets. It has an average radius of 6371 km and its interior consists of a mantle, a liquid core and a solid core. The energy released by the solidification of the core, through the settling of solid particles to the center of the planet, and the heat released by the freezing

process, are believed to be the principal sources of power for the dynamo, which allows our planet to have a magnetic field [*Russell*, 1993].

The Earth's magnetic field is basically a dipole, with its axis tilted with respect to the rotation axis by around 11°. This value is not constant but has been varying in magnitude and spatial orientation. The Earth's dipole points downward, and therefore the magnetic field at the magnetopause is directed northward, as it can be seen in Figure 2.2.

As mentioned in Section 2.1, the solar wind also carries a magnetic field and streams away from the Sun across the Earth's orbit and further beyond at supersonic velocities. That means that the solar wind ions flow at speeds much in excess of either their thermal speed or any wave speed the plasma can support. The electrons, by contrast, are subsonic because of their much higher thermal speed. The Earth's dipole moment of about 7.8×10^{15} Tm^3 is strong enough for its magnetic field to present an obstacle to the supersonic solar wind flow. Here, the solar wind is decelerated and deflected by a collisionless shock wave known as the *bow shock*. A bow shock forms as the supersonic solar wind encounters Earth's magnetosphere. The supersonic incoming flow cannot be deflected since information about the presence of Earth's magnetosphere cannot travel upstream until the flow has been made subsonic by a shock transition. This collisionless shock acts to change the local plasma properties allowing the incoming jet to deflect around the magnetosphere.

In its turn, the kinetic pressure of the solar wind distorts the shape of the terrestrial dipolar field, which is compressed in the dayside and stretches out in the nightside into a long *magnetotail*.

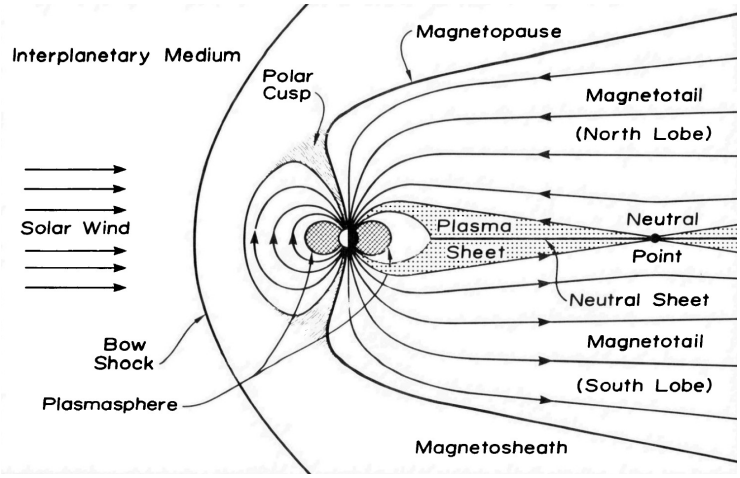

Figure 2.2: Illustration of the noon-midnight cross section of the magnetosphere [*Russell*, 1972]

The bow shock, as illustrated in Figure 2.2, is formed in front of the dayside magnetosphere, and the region of shocked solar wind plasma surrounding the magnetosphere is called the *magnetosheath*. The boundary of the magnetosphere is known as *magnetopause*

and there is very little flow of mass or momentum across it, since the magnetosphere acts as a shield from the direct influx of the solar wind. However, the shielding is not perfect and this allows solar wind plasma to enter the magnetosphere. The process that allows particles from the solar wind to enter the magnetosphere is known as *magnetic reconnection* and will be explained in detail in Section 2.5.

The redistribution of the solar wind energy in the ionosphere-magnetosphere system can lead to two different classes of geomagnetic activity, which are distinguished as *geomagnetic storms* and *substorms*. A geomagnetic storm is a major disturbance of the Earth's magnetic field caused by the solar wind. The generation of geomagnetic storms requires relatively specific conditions in the solar wind, which correlates with the level of solar activity. If the IMF is strong and steadily southward for several hours, the energy content in the magnetosphere increase significantly by loading of magnetic flux, and a geomagnetic storm may occur as a result of reconnection releasing this newly added flux [*Russell*, 2000]. The reconnection process in the magnetotail energizes the ring current and leads to energy deposition in the ionosphere. Some geomagnetic storms are triggered by the arrival of interplanetary shocks, which are characterized by large velocities and densities, leading to increased ram pressure, $P = n_{sw}v_{sw}^2$. The arrival of the shocks generally coincides with the onset of the first phase of the storm. The initial phase of the storm is followed by the main phase, in which sustained southward interplanetary fields are present. During this phase, charged particles in the near-Earth plasma sheet are energized and injected deeper into the inner magnetosphere, and multiple intense substorms occur, with the attendant auroral and geomagnetic effects. When the interplanetary field turns northward again, the rate of plasma energization and inward transport slows and the various loss processes that remove plasma from the ring current can begin to restore it to its pre-storm state. This is known as the recovery phase.

Substorms, first described by *Akasofu* [1964], can be defined as: *A magnetospheric substorm is a transient process initiated on the nightside of the earth in which a significant amount of energy derived from the solar wind-magnetosphere interaction is deposited in the auroral ionosphere and in the magnetosphere* [*Rostoker et al.*, 1980]. Several substorms can be observed during a geomagnetic storm, but they can also appear during rather quiet periods where no significant storm is in progress [*Gonzalez et al.*, 1994].

Substorms are also controlled by the interplanetary magnetic field, prevailing when it points southward, and in the simplest case, they also appear to have three phases: a growth phase in which energy is extracted from the solar wind and stored in the magnetotail, an expansion phase in which energy is explosively released, and a recovery phase in which the magnetosphere relaxes to a quiet state. However, weak auroral disturbances called pseudobreakups can occur during the growth phase, or more than one expansion phase may follow a single growth phase [*McPherron*, 1979].

2.3 Plasma Physics

2.3.1 Concept of plasma

A *plasma* is a type of ionized gas which forms as electrons are knocked free from atoms. The ionization process can be due to collisions with other atoms or molecules, or through ionizing radiation - light. Since a plasma is made up of negatively and positively charged particles that move around, both electric and magnetic fields will be generated inside a plasma. We say that a plasma has *collective behaviour* because these fields affect the motion of particles far away, meaning that motions inside a plasma do not only depend on local conditions, but also on the state of the plasma in remote regions.

Plasmas are quasineutral gases, which means that they are neutral enough so that one can take $n_e \approx n_i \approx n$, but not so neutral that all the interesting electromagnetic forces vanish. Here, n_e represents the electron density, n_i the ion density and n is a common density called *plasma density*. Any region inside a plasma subject to charge imbalance will attract particles of the opposite charge until the charge is shielded away. This is known as *Debye shielding*. The *Debye length* (λ_D) is a measure of the shielding distance. It is defined as

$$\lambda_D \equiv \frac{\epsilon_0 k_B T_e}{n e^2}, \tag{2.1}$$

where ϵ_0 is the vacuum permittivity, k_B is the Boltzmann constant, T_e is the electron temperature, n is the plasma density, and e is the electron charge. Here, the electron temperature is used, because electrons are typically the ones to do the shielding due to their high mobility. The potential due to a point-like charge will be given by:

$$\phi = \phi_0 e^{-r/\lambda_D}, \tag{2.2}$$

where ϕ_0 is the potential of the perturbing charge and r is the distance from its center. This means that the direct effect of the perturbing charge will be unimportant on scales larger than the Debye length. The typical length scale of the plasma needs to be much larger than the Debye length $L \gg \lambda_D$ in order to be quasineutral. In addition, the number of particles forming the plasma needs to be large enough to do the shielding. If N_D is the number of particles inside a sphere of radius λ_D, then $N_D \ggg 1$ must be fulfilled.

The last condition that an ionized gas needs to fulfill in order to be a plasma is related to collisions. If the collision frequency of the particles of a gas is too high, its motion will be controlled by ordinary hydrodynamic forces rather than by electromagnetic forces. In order for a gas to behave like a plasma we need $\tau\omega > 1$, where ω is the collision frequency and τ is the mean time between collisions with neutral atoms [*Chen and Torreblanca*, 2006].

2.3.2 Field equations for single particles

The motion of charged particles is strongly influenced by the presence of the electromagnetic fields, while at the same time it is also the source of the fields. In this section, we will introduce the equations that describe this coupling between electric charges and electromagnetic fields, which is considered fundamental for describing the behaviour of plasma.

If a particle of charge q moves with velocity $\mathbf{v}$ in the presence of an electric field $\mathbf{E}$ and a magnetic field $\mathbf{B}$, then it will experience a force which will modify its trajectory. Its equation of motion will then be given by:

$$m\frac{d\mathbf{v}}{dt} = q(\mathbf{E} + \mathbf{v} \times \mathbf{B}) \tag{2.3}$$

where the first term on the right-hand side is the *Coulomb force* and the second term is the *Lorentz force*. The combination of the terms inside the parenthesis represents the electric field, $\mathbf{E}' = \mathbf{E} + \mathbf{v} \times \mathbf{B}$, in the particle frame of reference.

In the presence of an externally imposed large scale magnetic field, for example the Earth's magnetic field or the IMF, and in the absence of externally imposed electric field, the motion of a particle will perform circular motions, with its central axis aligned with the magnetic field. The center of the circle is often referred to as the *guiding center* [*Alfven*, 1940]. Due to various combinations of electric and magnetic fields, the guiding center may drift, resulting in bulk flows of the plasma. Common drifts are: the $\mathbf{E} \times \mathbf{B}$ drift, which is due to the combination of electric and magnetic fields; the polarization drift, due to temporal changes in the electric field; the gradient and curvature drifts, due to gradients or curvature in the magnetic fields and the magnetization drift, due to the effects of magnetized particles in a density gradient.

Maxwell's equations

The electric and magnetic fields, though, are not independent of each other. This fact, and also the relationship between the fields and the particles is described by *Maxwell's equations*:

$$\text{Gauss's law:} \quad \nabla \cdot \mathbf{E} = \sigma/\epsilon_0 \tag{2.4}$$

$$\text{Gauss's law for magnetism:} \quad \nabla \cdot \mathbf{B} = 0 \tag{2.5}$$

$$\text{Faraday's law:} \quad \nabla \times \mathbf{E} = -\frac{\partial \mathbf{B}}{\partial t} \tag{2.6}$$

$$\text{Ampère-Maxwell's law:} \quad \nabla \times \mathbf{B} = \mu_0 \mathbf{j} + \epsilon_0 \mu_0 \frac{\partial \mathbf{E}}{\partial t} \tag{2.7}$$

where $\mathbf{j}$ is the current density, $\mathbf{j} = e(n_i\mathbf{v}_i - n_e\mathbf{v}_e)$, σ is the charge density, $\sigma = e(n_i - n_e)$, and ϵ_0 and μ_0 are the vacuum permittivity and susceptibility, respectively. Here, $\mathbf{v}_s$ is the bulk velocity, and n_s is the density of the plasma species s (typically electrons and a single ion species).

Gauss's law (eq. 2.4) states that the net flux of the electric field through any closed surface is proportional to the charge enclosed by the surface. Gauss's law for magnetism (eq. 2.5) tells us that there are no sources or sinks for the magnetic field. This is the same as stating that magnetic monopoles don't exist, and the net outflow of a magnetic field through any closed surface is zero.

From the last two equations, we can see that the electric and magnetic fields are interdependent, coupled by their spatial and temporal variations. Faraday's law (eq. 2.6) describes how a time varying magnetic field induces an electric field, while Ampère's law with Maxwell's addition (2.7) tells us that magnetic fields can be generated in two different ways: by electric currents (original Ampère's law) or by changing electric fields (Maxwell's addition, also called *displacement current*). The displacement current term ($\epsilon_0\mu_0\frac{\partial \mathbf{E}}{\partial t}$) appears when there are fast oscillations in the electric field and will be neglected in our description, since the time scales involved with it are too small to be of interest.

2.3.3 Kinetic Theory and Vlasov's equation

When considering a plasma, we must take into account a large amount of particles, which will induce some collective effects that will allow us to simplify the evolution. We can obtain a complete microscopic description of a plasma by considering the motion of each one of the particles, their charge and current densities, the electric and magnetic field they generate and the effects of these microscopic fields on the particle motion (eqs. 6.2 to 6.9 in *Baumjohann and Treumann* [2012]).

By solving all these equations, we would get the exact (with some restrictions) microscopic solution of the behaviour of the plasma. However, this calculation is practically infeasible, and we don't require all the information that it would provide us. Consequently, it's useful to develop an averaging scheme to get an expression that describes the evolution of the smoothed, averaged distribution function, f, in response to the smoothed, averaged electric and magnetic fields in the plasma. This is the so-called Klimontovich-Dupree equation [*Klimontovich*, 1969].

By assuming that space plasmas are collisionless and neglecting the correlations between the fields, the mentioned expression can be simplified to the simplest possible form of kinetic equation of a plasma, which is called *Vlasov's equation*:

$$\frac{\partial f}{\partial t} + \mathbf{v}\cdot\nabla_x f + \frac{q}{m}\big(\mathbf{E} + \mathbf{v}\times\mathbf{B}\big)\cdot\nabla_v f = 0 \tag{2.8}$$

which describes the evolution of the distribution functions. It also implies that, in the absence of collisions, the phase space density remains constant under the interaction of

the particles with the ensemble averaged self-consistent fields in the Lorentz force as it is convected with the particles. Consequently, instead of describing every particle as a single entity, it is useful to describe the distribution of particles in position and velocity space (together termed phase space) $f(\mathbf{r}), \mathbf{v}$. The phase space density, thus, describes how many particles are present at the physical coordinate $\mathbf{r}$ with the velocity $\mathbf{v}$.

The collective effect of the particle distribution described by f can be obtained by taking the velocity moments of the distribution:

$$\text{Number density: } n = \int_{-\infty}^{+\infty} f d^3v \tag{2.9}$$

$$\text{Bulk velocity: } \mathbf{v} = \int_{-\infty}^{+\infty} f\mathbf{v} d^3v \tag{2.10}$$

$$\text{Pressure: } \mathbf{P} = \int_{-\infty}^{+\infty} f(\mathbf{v} - \langle\mathbf{v}\rangle)^2 d^3v. \tag{2.11}$$

The derived macroscopic quantities no longer depends on velocity coordinates, but are only a function of space and time.

2.4 Magnetohydrodynamics (MHD)

Equation 2.8 describes how distribution functions evolve, but we are interested in a dynamical theory in which the state of our system is described by macroscopic variables, such as the ones found by taking the velocity moments of the probability distribution. Our goal will be to develop a theory that describes the plasma as a single fluid, but we will first introduce the Multi-Fluid Theory, which separates the different species in the plasma.

2.4.1 Multi-Fluid Theory

Integrating the Vlasov equation with respect to the velocity space, we can get the evolution equations for the macroscopic quantities that were mentioned in the previous subsection for each species in the plasma. While a plasma may consist of several ion species, the near-Earth environments of our interest is usually dominated by H^+ ions (protons). We will therefore consider a two-fluid plasma, with one ion fluid and one electron fluid.

Taking the zeroth moment of the Vlasov equation, we find the *continuity equation* for each component of the plasma (eq. 2.12). Its physical meaning is that the particle number density, the charge and the mass are conserved during the motion of the fluid. Written

in the conservational form it emphasizes that we neglect any possible sources, such as ionization or recombination that could be important in some plasma regimes.

$$\frac{\partial n_s}{\partial t} + \nabla \cdot (n_s \mathbf{v}_s) = 0 \tag{2.12}$$

By taking the first moment, we get the equation of motion of each fluid component, or the *momentum density conservation equation*. This equation tells us how the fluid velocity, v_s, evolves.

$$\frac{\partial (n_s \mathbf{v}_s)}{\partial t} + \nabla \cdot (n_s \mathbf{v}_s \mathbf{v}_s) + \frac{1}{m_s} \nabla \cdot \mathbf{P}_s - \frac{q_s}{m_s} n_s (\mathbf{E} + \mathbf{v}_s \times \mathbf{B}) = 0 \tag{2.13}$$

However, this equation introduces a new quantity, the pressure tensor $\mathbf{P}_s$, whose evolution we also need to know. Instead of taking a higher moment of the Vlasov equation, which would give us an equation for the evolution of the pressure tensor, but introduce another new quantity, we choose to close our set of equations by describing the pressure with an equation of state which relates the pressure to changes in the density:

$$p_s = p_{s0} \left(\frac{n_s}{n_{s0}} \right)^{\gamma} \tag{2.14}$$

where γ can take different values depending on which approximation we are considering. In a collisionless, ideal, isotropic plasma, the temperatures and densities of each species can, to a good approximation, be considered to evolve adiabatically. γ will then take the value $\gamma = 5/3$ and this is the approximation that we will make for this study. However, under the isothermal approximation it would take a value of 1, or 0 for isobaric conditions.

2.4.2 Magnetohydrodynamic equations

The *magnetohydrodynamic* (MHD) model is a *single fluid* model of a fully ionized plasma, in which the plasma is treated as a single hydrodynamic fluid acted upon by electric and magnetic forces [*Goldston and Rutherford*, 1995].

Our derivation of the magnetohydrodynamic equations will be limited to the case of a hydrogen plasma, which is composed of electrons ($q_s = -e$, $m_s = m_e$) and only one ion species with charge $+e$ and mass m_i. Since electrons are much lighter than protons ($m_e/m_i = 1/1836 \ll 1$), we will be able to simplify some expressions. We will also assume quasineutrality, so that $n_e \approx n_i \approx n$.

By adding the continuity equations for ions and electrons (eq 2.12 with $s = i, e$), and defining the mass density of the single fluid as $\rho = n_i m_i + n_e m_e \approx n m_i$ and the mass

velocity as $\mathbf{v} = (n_i m_i \mathbf{v}_i + n_e m_e \mathbf{v}_e)/\rho$ we obtain the *mass continuity equation*:

$$\frac{\partial \rho}{\partial t} + \nabla \cdot (\rho \mathbf{v}) = 0. \tag{2.15}$$

The continuity equation is the evolutionary equation of the mass density, expressing that the temporal change in mass density inside of a volume is equal to the transport of mass in or out of the volume.

By doing the same with the equations of motion (eq. 2.13 with $s = i, e$), we obtain the *single fluid equation of motion*:

$$\rho\left(\frac{\partial \mathbf{v}}{\partial t} + \mathbf{v} \cdot \nabla \mathbf{v}\right) = -\nabla \cdot \mathbf{P} + \mathbf{j} \times \mathbf{B}. \tag{2.16}$$

The term in the left-hand side represents the net change of momentum density of a fluid element. The term $\nabla \cdot P$ is the thermal pressure tensor, which is commonly assumed to be isotropic. The term $\mathbf{j} \times \mathbf{B}$ is the Lorentz force of the combined species. The momentum equation does not depend on the electric field, since any separation between ions and electrons would instantly be neutralized, so that the plasma remains, to a very good approximation, quasi charge-neutral.

The equation of state for the single fluid can be written as:

$$\frac{d}{dt}\left(\frac{p}{\rho^\gamma}\right) = 0, \tag{2.17}$$

where $\gamma = 5/3$ is the adiabatic index, as explained above.

Finally, to quantify the difference in the ion and electron motion, we can subtract the two species (2.13) from each other to obtain the *Generalized Ohms Law*:

$$\mathbf{E} + \mathbf{v} \times \mathbf{B} = \eta \mathbf{j} + \frac{1}{ne}\mathbf{j} \times \mathbf{B} - \frac{1}{ne}\nabla \cdot \mathbf{P}_e + \frac{m_e}{ne^2}\frac{\partial \mathbf{j}}{\partial t} \tag{2.18}$$

which is written in its full form for completeness.

Adding Maxwell's equations (eqs 2.4 to 2.7) to this set of equations, we get what we call the *Governing MHD equations*.

2.4.3 Resistive MHD

The Generalized Ohms Law (eq. 2.18) allows us to determine $\mathbf{E}$ by plasma dynamics; $\mathbf{E}$ will assume the value it must have in order to prevent a differential acceleration of ions and electrons that would separate charges too much [*Vasyliunas*, 2005].

The last term in equation 2.18 represents the electron inertia and can be safely neglected, as the electrons, with a mass 1/1840 of the protons, respond much quicker com-

pared to the overall dynamics of the system. $\nabla \cdot \mathbf{P}_e$ is the electron pressure tensor, while the term with $\mathbf{j} \times \mathbf{B}$ is called the Hall term and accounts for two-fluid effects [*Vasyliunas*, 1975]. These two terms can also be neglected if the ion Larmor radius is very small compared to the scale-length of the fluid motion, which will be our case. Employing these approximations leads to what is called *Resistive MHD*, and Ohms Law, in this case, reduces to:

$$\mathbf{E} + \mathbf{v} \times \mathbf{B} = \eta \mathbf{j} \tag{2.19}$$

in which the remaining term in the RHS, the resistive term, can be thought of as a term that allows for the diffusion of plasma across the magnetic field. It is often referred to as "Ohmic dissipation" since its form resembles diffusion caused by collisions between charged particles. One can intuitively imagine that collisions can make a particle gyrating about a field line diffuse (by collisions) to another field line. If we consider that the plasma has an infinite conductivity, equation 2.19 reduces to

$$\mathbf{E} + \mathbf{v} \times \mathbf{B} = 0, \tag{2.20}$$

which is referred to as *Ideal MHD*, where no appreciable electric field will exist in the frame of the plasma. The consequence of this will be that the plasma will be completely tied to the magnetic field lines, not being able to move across different field lines. This is known as the *frozen-in* condition [*Alfvén*, 1942]. This implies that the magnetic field has to move with the plasma; i.e. the only change of $\mathbf{B}$ is by means of $\mathbf{v}$. As we will show in the next section, the diffusive terms (terms on the right-hand side of eq. 2.18) will be important for enabling changes in the magnetic field topology, resulting in explosive energy transfer from the magnetic field to the plasma through the process of *magnetic reconnection*.

2.5 Magnetic reconnection

In a highly conducting plasma ($\eta \to 0$), we can consider Ideal MHD (eq. 2.20), which implies that the large-scale magnetic fields are transported bodily with the bulk motion of the plasma (frozen in condition). If the frozen-in approximation is not violated, any IMF impinging on our magnetopause would deflect and flow around without mixing of magnetospheric and solar wind plasma.

However, we do observe solar wind particles in the Earth's magnetosphere, and the process that allows this to happen is called *Magnetic Reconnection* or magnetic field line merging.

Magnetic reconnection, first proposed by *Giovanelli* [1947] to explain solar activities, can be defined as the process by which magnetic field lines of opposite polarity reconfigure to a lower-energy state, with the release of magnetic energy to the surroundings in the form

of plasma kinetic and thermal energy. The reconnection process occurs where the frozen-in condition is violated, and an interconnection between the initially unlinked, antiparallel components of the magnetic fields is possible. This is illustrated in Figure 2.3.

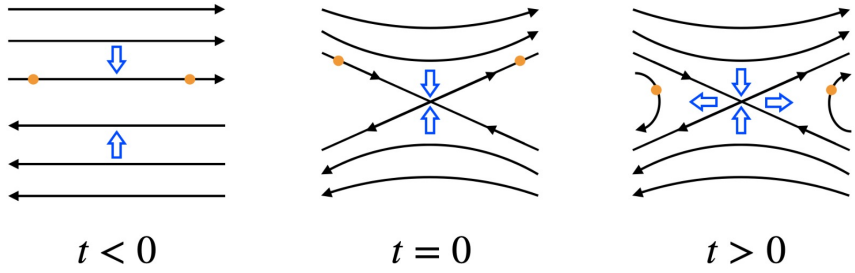

Figure 2.3: Evolution of magnetic field line merging. The dots represent two plasma elements. Before reconnection is initiated, the two plasma elements label the same field line. After magnetic reconnection is initiated, the two plasma elements are no longer labelling the same field line.

Magnetic reconnection is made possible by the existence of a *diffusion region*, where ideal MHD is no longer valid. In fluid-based descriptions, most studies of magnetic reconnection are based on the resistive MHD equations, mentioned in Section 2.4.3, where a resistivity will be responsible for the breakdown of the frozen-in condition [*Cai and Lee*, 1997; *Gonzalez and Parker*, 2016].

2.5.1 Magnetic reconnection in the magnetosphere

Dungey [1961] proposed a model to explain how magnetic reconnection between the interplanetary and terrestrial magnetic fields could explain the magnetospheric dynamics. Figure 2.4 shows the basics of this model, which is known as *the Dungey cycle*.

The Dungey cycle begins when a southward-directed interplanetary field line encounters the magnetopause and reconnects with a closed terrestrial field line (lines marked with number 1 in Figure 2.4). The merged field lines split into two open field lines (2) and are transported tail-wards by the solar wind (3-6). At the nightside, the two open field line halves meet again and reconnect (7), leaving a stretched closed field line connected to the earth and a field line with both ends connected to the solar wind (8). The closed field line will relax getting closer to the Earth and eventually going back to the dayside, completing the cycle.

It is important to notice that we are conveniently talking about open and closed field lines even though magnetic field lines have no ends. We will talk about a closed field line when, if followed through space from the surface of the earth, it returns to the surface of the earth within a finite path length. Otherwise, we will talk about open field lines [*Russell*, 1972].

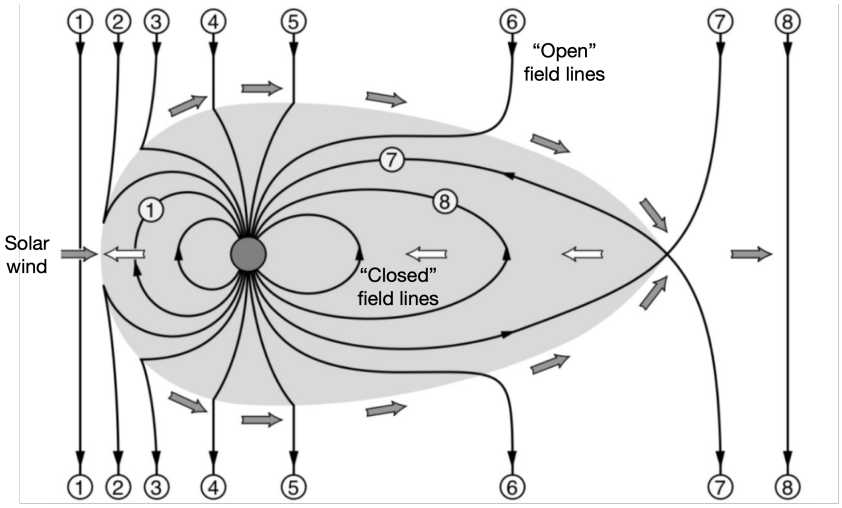

Figure 2.4: Field line merging and reconnection at the magnetopause. Edited from *Baumjohann and Treumann* [2012].

We also note that, contrary to our two-dimensional cartoons, the opposing magnetic fields only rarely are exactly antiparallel. More commonly they have shears below 180 deg. The component that does reverse from one side to the other is often referred to as the reconnection component (this is what is depicted in Figure 2.3), while the component that reduces the shear (which would be directed into or out of the plane in Figure 2.3) is called the guide field.

We call the line along which reconnection occurs the *X line* or *neutral line*. The first name is due to the topology resembling the X letter that the field lines adopt along this line (see Figure 2.3). The second name is given because the reconnecting magnetic field strength vanishes at the X line, turning the X line into a neutral line. In figures 2.3 and 2.4, this line would go into and out of the plane if we were in a 3D system. In a 2D system, the X line can be called X point instead.

2.5.2 The magnetic reconnection process

As we mentioned in the previous subsection, in the magnetosphere we can distinguish three classes of field lines: open field lines, closed field lines and interplanetary field lines. The regions of space traversed by the different classes of field lines are bounded by a surface made up of field lines called the *separatrix*. The separatrix has two branches that will intersect along the X-line as it is shown in Figure 2.5.

Whenever there is an increase or decrease in the amount of magnetic flux connecting from the Earth to the interplanetary magnetic field, a magnetic flux transport across the separatrix will be required. This will imply a flow of plasma across the separatrix and, thus, the breaking of the frozen-in condition. This is often used as a definition for magnetic reconnection [*Vasyliunas*, 1975]. The magnitude of the plasma flow will be a measure of

the merging rate.

For a given magnetic field configuration, the rate at which magnetic energy is being converted into other forms is given by the rate at which the magnetic flux is being transported across the separatrix, and is proportional to the plasma flow. This means that the merging rate is also a measure of the energy conversion rate.

The coupling between the flow of plasma and the transport of magnetic flux arises from the equation for the electric field, **E**, which corresponds to equation 2.20 for most regions in space plasmas. This equation implies that, in steady-state, any plasma flow perpendicular to a magnetic field is associated with an electric field, and the same goes for a flow across the separatrix. Thus, if there exists an electric field at the separatrix, this means that magnetic reconnection is occurring.

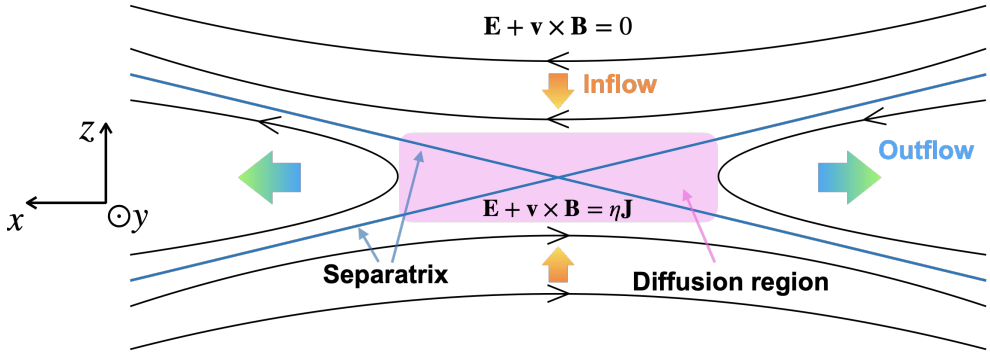

Figure 2.5: Illustration of the magnetic field lines around the X point as black solid lines, the separatrix as blue lines and the diffusion region as the pink region. The arrows indicate the inflow (orange) and outflow (blue).

However, at the neutral line, the term $\mathbf{v} \times \mathbf{B}$ vanishes, and ideal Ohm's law is no longer appropriate. In this region around the X line, we will have to use equation 2.19, and it will be the term $\eta\mathbf{j}$ that will contribute to the electric field. The region around the X line, where $\mathbf{v} \times \mathbf{B}$ is very small compared to $\mathbf{E}$ and where the term $\eta\mathbf{j}$ dominates, is called the *diffusion region* or the *resistive region*. In Figure 2.5, the diffusion region has been illustrated as a pink rectangle.

Using Faraday's law (equation 2.6), it can be proven that E_y inside the diffusion region is the same as E_y outside the diffusion region, where eq. 2.20 applies. Since E_y outside the diffusion region is related to the plasma flow across the separatrix, this means that the electric field along the X-line is also a measure of the reconnection rate [*Vasyliunas*, 1975].

The reconnection rate is also conventionally measured by the dimensionless ratio (Alfvén Mach number)

$$M_A \equiv \frac{v_0}{v_{A0}} \tag{2.21}$$

where v_0 is the magnitude of the plasma flow speed towards the diffusion region, but far away from it, and $v_{A0} \equiv B_0/(4\pi\rho)^{1/2}$ is the Alfvén speed in the inflow region.

During the merging process, plasma flows into the field reversal region from both sides. This plasma flow is usually called *inflow*, and the region in which the plasma flows towards the reconnection point is called *inflow region*. Since plasma cannot accumulate there indefinitely, it must somehow flow out of the region as well (*outflow*). We will assume that the outflow is perpendicular to the neutral line and to the inflow, as shown in Figure 2.5. The *outflow region* will contain the plasma moving away from the X point.

2.5.3 Magnetic Lundquist number

Inserting the electric field given by the resistive Ohm's law, $\mathbf{E} = -\mathbf{v} \times \mathbf{B} + \eta\mathbf{j}$, inside Faraday's Law (eq. 2.6) in its dimensionless form, we obtain the *induction equation*:

$$\frac{\partial \mathbf{B}}{\partial t} = \nabla \times (\mathbf{v} \times \mathbf{B}) - \eta \nabla^2 \mathbf{B} \tag{2.22}$$

where we have used that $\mathbf{j} = \nabla \times \mathbf{B}$ and considered a uniform resistivity. The first term on the right side of this equation represents the convection of the magnetic field by the plasma flow, and the second represents the diffusion of the field due to a finite resistivity. The *Lundquist number*, S, tells us about the relation between the timescales of these two processes: τ_c for the convection and τ_d for diffusion.

By doing a scaling analysis of these two terms we can write that

$$\frac{B}{\tau_c} \sim \frac{v_A B}{\lambda} \quad ; \quad \frac{B}{\tau_d} \sim \frac{\eta B}{\lambda^2}$$

where λ represents the length scale of the region where we calculate the Lundquist number. The Lundquist number is defined as $S \equiv \frac{\tau_d}{\tau_c}$, so we can write it as:

$$S = \frac{\lambda v_A}{\eta} \tag{2.23}$$

High Lundquist numbers indicate highly conducting plasmas, while low Lundquist numbers indicate more resistive plasmas. Laboratory plasma experiments typically have Lundquist numbers between $10^2 - 10^8$ [*Ji and Daughton*, 2011], while in space, Lundquist numbers can be greater than 10^{20}. In the solar corona, for example, $S \approx 10^{12} - 10^{14}$ [*Huang and Bhattacharjee*, 2013].

2.6 Theoretical models of magnetic reconnection

Several models based on a hydromagnetic approach have been developed since *Giovanelli* [1947] proposed the concept of magnetic reconnection. In this section, we will discuss some common aspects of this approach before introducing the model proposed by *Sweet* [1958] and developed further by *Parker* [1957b, 1963]. Their model neglected entirely the magnetic field in the outflow, and the reconnection rate obtained by it is orders of magnitude smaller than observed. *Petschek* [1964] argued that the neglect of the downstream magnetic field is not justified, except in a small part of the system, and he presented another model that accounted for high enough reconnection rates. Different models have also been presented by *Sonnerup* [1970] and *Yeh and Axford* [1970], but they will not be discussed in this thesis.

Let d be the half-width and L the half-length of the box enclosing the diffusion region, and let v_1 and v_2 be the inflow and outflow velocities near the box, respectively (see Figure 2.6). Applying the conservation of mass (equation 2.15) in steady-state ($\partial\rho/\partial t = 0$), we find that the relation between the inflow and outflow velocities is given by

$$v_1 L = v_2 d \tag{2.24}$$

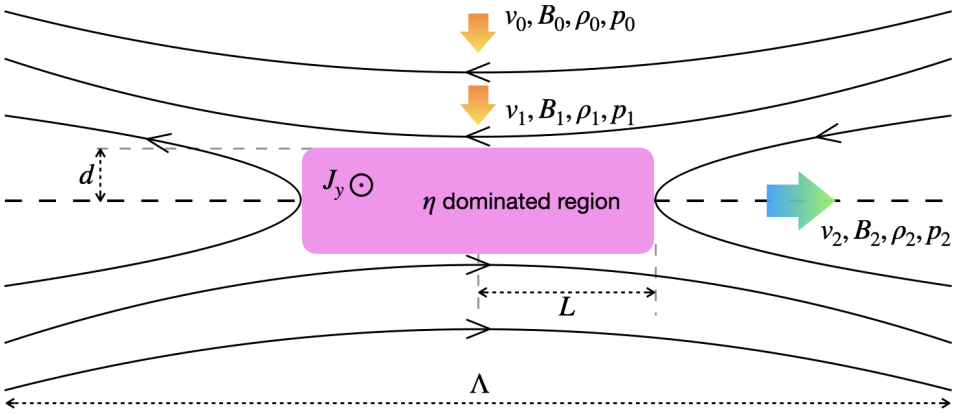

Figure 2.6: Illustration of the diffusion region together with the different parameters. Subscripts 0, 1 and 2 mean far from the diffusion region, inflow region and outflow region respectively.

As it has been pointed out before, for strictly anti-parallel reconnection, the magnetic field in the neutral line is zero, but its curl is not. This means that a j_y will arise inside the diffusion region (see equation 2.7) as a consequence of Amperes law:

$$j_{NL} = \frac{B_1}{\mu_0 d} \tag{2.25}$$

This current density will be the main contributor to the electric field inside the diffusion region, which will have to be the same as the electric field outside. From the resistive Ohm's Law (2.19) we get:

$$E_0 = -v_1 B_1 = v_2 B_2 = \eta j_{NL}. \tag{2.26}$$

Thus, outside the diffusion region, the electric field is determined by the bulk velocity, but inside the diffusion region, where both the flow velocity and the magnetic field go towards zero, the resistive component dominates.

2.6.1 Sweet-Parker Theory

The Sweet-Parker model description is the simplest way of describing magnetic reconnection. As it has been pointed out before, magnetic reconnection is a process in which magnetic energy is converted into mechanical energy. In this model, it is considered that the kinetic energy in the inflow region, and the magnetic energy in the outflow region, are negligible. Moreover, it is assumed that all the magnetic energy is converted into kinetic energy, and thermal energy is not considered.

Sweet-Parker theory from a momentum perspective

Let us examine the force balance between the inflow region and the X line by examining the z-component of eq. 2.16 and Ampère-Maxwell's equation (eq. 2.7) without the displacement current ($\mathbf{j} = \frac{1}{\mu_0}\nabla \times \mathbf{B}$):

$$\mathbf{j} \times \mathbf{B} - \nabla p = \frac{1}{\mu_0}\mathbf{B} \cdot \nabla \mathbf{B} - \nabla \frac{B^2}{2\mu_0} - \nabla p = \rho \mathbf{v} \cdot \nabla \mathbf{v} \approx 0 \tag{2.27}$$

This force balance is approximately simply a balance between the inward-directed magnetic pressure, and the outward-directed plasma pressure at the center:

$$\frac{\partial}{\partial z}\left(\frac{B^2}{2\mu_0} + p\right) = 0 \quad \Rightarrow \quad \frac{B_1^2}{2\mu_0} = p_{NL} \tag{2.28}$$

where p_{NL} is the pressure at the neutral line. On the other hand, in the outflow region, the magnetic field is considered weak enough to be neglected, which means that

$$\rho \mathbf{v} \cdot \nabla \mathbf{v} = \mathbf{j} \times \mathbf{B} - \nabla p \approx -\nabla p$$

and

$$\frac{\rho_2 v_2^2}{2} = p_{NL} \tag{2.29}$$

If we assume that the density is the same everywhere outside the diffusion region ($\rho_0 = \rho_1 = \rho_2 = \rho$) and putting equations 2.28 and 2.29 together we get that

$$\frac{\rho v_2^2}{2} = \frac{B_1^2}{2\mu_0}$$

In terms of energy, this expression means that *all* the magnetic energy is converted into kinetic energy, leaving out the thermal energy as it was mentioned before. This expression leads us to the following expression for the outflow speed:

$$\boxed{v_2 = \frac{B_1}{\sqrt{\mu_0 \rho}} \equiv v_{A1}} \tag{2.30}$$

Thus, the outflow velocity is equal to the Alfvén speed in the inflow region and does not depend on the size or shape of the diffusion region. This result implies that the velocity at which the magnetic field lines are being processed is limited by the Alfvén speed.

Let us see what happens to the inflow speed next. Putting together equations 2.26, 2.25 and 2.30, and using eq. 2.24, we get:

$$v_1 = -\eta \frac{1}{\mu_0 d} = \frac{\eta}{\mu_0} \frac{v_2}{v_1 L} = \frac{\eta}{\mu_0} \frac{v_{A1}}{v_1 L} \quad \Rightarrow \quad \frac{v_1^2}{v_{A1}^2} = \frac{\eta}{\mu_0 v_{A1} L},$$

which can be written in terms of the inflow Lundquist number or the inflow Mach number as:

$$\left| \frac{v_1}{v_{A1}} \right| = \frac{1}{\sqrt{S_1}} = M_1$$

This can be related to the properties far upstream (labelled with 0 in Figure 2.6) by $v_1 B_1 = v_0 B_0$, leading us to the following expression:

$$v_0 = -v_{A1} \frac{d}{L} \frac{B_1}{B_0} \tag{2.31}$$

However, the Sweet-Parker model assumes that the diffusion region is *thin and extended*, so that $L \approx \Lambda$, where Λ is a characteristic MHD scale length. This condition gives a largely homogenous external region, so that we can consider $B_1 \approx B_0$. v_0 will then also have the same value as v_1.

For a finite-sized diffusion region, though, the effective inflow (v_1) would not be equal to the ambient conditions (v_0). The shape of the diffusion region controls how the field is deformed as it expands towards the diffusion region. More on this will be discussed in the results.

In the case that we are discussing, we can safely assume $v_0 = v_1$, so that the reconnection

rate becomes

$$M_{A0} = \frac{1}{\sqrt{S_0}} \sim \sqrt{\eta} \tag{2.32}$$

This result, for space plasmas, gives a value that is too small compared to the real reconnection rate. The main factors that keep the reconnection rate so low in this model are the aspect ratio of the diffusion region and the magnitude of η or the mechanism that generates it. If we consider that the aspect ratio is around $\frac{d}{L} \sim 0.1$, then we obtain a reconnection rate of around 0.1 which is of the order of what we observe.

Sweet-Parker theory from an energy perspective

As mentioned, the Sweet-Parker scaling derived from an energy perspective emphasizes that all the magnetic energy is converted into bulk energy. The Poynting theorem describes how magnetic energy is converted into mechanical energy:

$$\frac{\partial}{\partial t}\frac{B^2}{2\mu_0} + \nabla \cdot \mathbf{S} = -\mathbf{E} \cdot \mathbf{j}. \tag{2.33}$$

The first term represents the energy stored in the magnetic field and the second term represents electromagnetic energy flow and is contained in the Poynting vector $\mathbf{S} \equiv \frac{\mathbf{E}\times\mathbf{B}}{\mu_0}$. The term on the right-hand side represents the rate per unit volume of electromagnetic energy conversion. If the quantity $\mathbf{E} \cdot \mathbf{j}$ is positive, it means that electromagnetic energy is being converted to mechanical energy, and the other way round if it is negative.

The mechanical energy includes both the energy of kinetic bulk flow and thermal motions. Its conservation equation is given by:

$$\frac{\partial}{\partial t}\left(\frac{\rho v^2}{2} + \frac{p}{\gamma - 1}\right) + \nabla \cdot \left[\left(\frac{\rho v^2}{2} + \frac{\gamma}{\gamma - 1}p\right)\mathbf{v}\right] = \mathbf{E} \cdot \mathbf{j} \tag{2.34}$$

where for an adiabatic approximation, $\gamma = 5/3$ would be used (see eq. 2.17). By assuming ideal MHD, $\mathbf{E} = -\mathbf{v} \times \mathbf{B}$, our Poynting vector becomes $\mathbf{S} = \frac{B^2}{\mu_0}\mathbf{v} - \frac{\mathbf{v}\cdot\mathbf{B}}{\mu_0}\mathbf{B}$. Then, combining equations 2.33 and 2.34, we obtain the following expression:

$$\frac{\partial \epsilon}{\partial t} = -\nabla \cdot \left[\left(\epsilon + p + \frac{B^2}{2\mu_0}\right)\mathbf{v} - \frac{\mathbf{v} \cdot \mathbf{B}}{\mu_0}\mathbf{B}\right] \tag{2.35}$$

for the evolution of the total energy, $\epsilon = \frac{\rho v^2}{2} + \frac{p}{\gamma - 1} + \frac{B^2}{2\mu_0}$, [*Birn and Hesse*, 2005].

Let's consider a stationary case, so that the time derivative in the left-hand side of equation 2.35 is 0, and apply the divergence theorem, so that we obtain the following:

$$\oint_S \left[\left(\epsilon + p + \frac{B^2}{2\mu_0}\right)\mathbf{v} - \frac{\mathbf{v} \cdot \mathbf{B}}{\mu_0}\mathbf{B}\right] \cdot \hat{s} dS = 0 \tag{2.36}$$

where S is the surface of our diffusion region, of length $2L$ and height $2d$, and $\hat{s}$ points out

of the box as it can be seen in Figure 2.7.

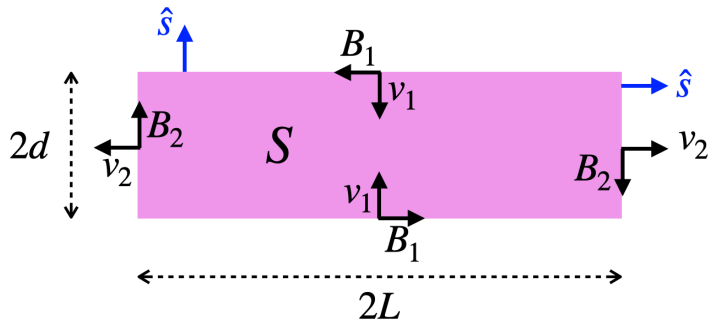

Figure 2.7: Illustration of the diffusion region as a surface to be integrated

By assuming that the thermal pressure, p, doesn't play any role in the energy conversion process, we can evaluate the integral in our box. The inflow is dominated by the magnetic field and the outflow by kinetic energy. With these assumptions eq. 2.36 reduces to:

$$L\left(\frac{B_1^2}{2\mu_0}v_1\right) = d\left(\frac{\rho v_2^2}{2}v_2\right) \tag{2.37}$$

Which can be simplified by applying the relation from equation 2.24 to:

$$\frac{B_1^2}{2\mu_0} = \frac{\rho v_2^2}{2}$$

This leads us to the same expression written in 2.30:

$$v_2 = \frac{B_1}{\sqrt{\mu_0 \rho}} = v_{A1}$$

The derivation based on energy conservation emphasizes that the original derivation only considered magnetic energy to kinetic bulk acceleration. It assumes a quasi-steady state, incompressible flow (eq. 2.24), and that the thermal enthalpy does not play any role in the energy conversion.

2.7 The reconnection rate problem

Observations and numerical simulations in a wide variety of settings suggest that the global rate of magnetic reconnection is approximately 0.1 in normalized units [*Comisso*

and Bhattacharjee, 2016; *Cassak et al.*, 2017]. This has been known for many years, but it has been extremely challenging to develop a theoretical understanding of why it is like this.

Knowing what controls the reconnection rate in various settings is crucial for many applications. For instance, a key aspect of space weather lies in the efficiency of solar wind-magnetospheric coupling and the rate at which the global convection pattern occurs, which is directly related to the reconnection rate of the Earth's dayside magnetopause. Also, this understanding is very important in magnetically confined fusion devices or for identifying reconnection and studying its effects in places where directly measuring magnetic fields is not possible, such as in astrophysical settings.

Observational evidence for the 0.1 reconnection rate can be obtained using plasma parameters observed at macroscopic scales. Let us consider two regions of magnetic field coming together and reconnecting, as shown in Figure 2.8, and let the time over which significant energy release via reconnection occurs be Δt. Suppose the reconnecting mag-

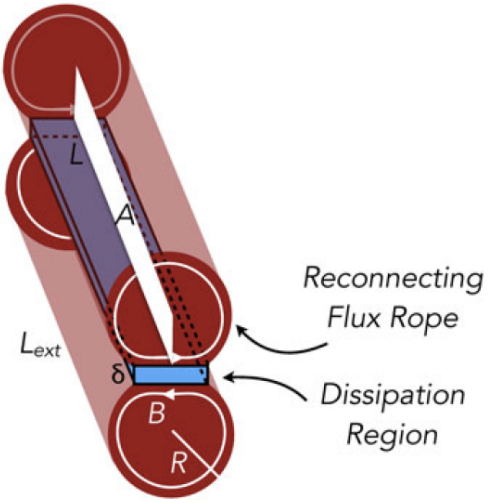

Figure 2.8: Sketch of two reconnecting flux ropes in red, with reconnecting magnetic field lines in white. The flux rope radius R and out-of-plane extent L_extt are shown. The dissipation region of thickness δ and length L is in blue. The white surface of area A denotes the location of the magnetic field that reconnects in a time Δt [*Cassak et al.*, 2017].

netic field has a characteristic strength B, threading a region of characteristic radius R and out-of-plane extent L_{ext}, each assumed uniform for simplicity. Then, the magnetic flux processed per unit time by reconnection is $BA/\Delta t$, where $A \sim RL_{ext}$. From Faraday's law, this must be associated with an electric field extending over a distance L_{ext} out of the reconnection plane. This will be the reconnection electric field. In SI units, the relation is

$$E \sim \frac{BA}{L_{ext}\Delta t} \sim \frac{BR}{\Delta t}, \tag{2.38}$$

which can be normalized by the reconnecting magnetic field B and the Alfvén speed c_A, and presented as a dimensionless quantity, E':

$$E' = \frac{E}{Bc_A} \sim \frac{R}{c_A \Delta t}. \tag{2.39}$$

Using this expressions and taking the needed plasma parameters, we can infer the reconnection rate in several different processes. Some of the values that have been obtained are $E' \simeq 0.053$ for geomagnetic substorms, $E' = 0.075$ for solar flares or $E' \simeq 0.21$ in magnetically confined fusion devices [*Cassak et al.*, 2017].

Regarding the numerical and theoretical efforts, studies on this problem have typically been performed using simplified systems like the one sketched in Figure 2.5. One of the first inputs on this matter is the Sweet-Parker theory, where *Parker* [1957b] showed that the reconnection rate scales as

$$E \sim \frac{d}{L} v_{out} B \tag{2.40}$$

where d and L are the thickness and length of the diffusion region respectively (see Figure 2.6) and v_{out} is the outflow speed, which scales like the Alfvén speed c_A. The local reconnection rate, normalized to B and c_A is

$$E' \sim \frac{d}{L} \tag{2.41}$$

which is proportional to $1/\sqrt{S}$ when the mechanism allowing the magnetic topology to change is a uniform resistivity. As it has been explained before, this prediction is too slow to account for the rates observed in solar flares and other phenomena [*Parker*, 1963], and the failure of this theory lies in the fact that the exhaust region closes down into an elongated region. Since the outflow is constrained to leave at the Alfvén speed, conservation of mass requires the inflow speed to be small.

The *Petschek* [1964] model uses a more localized diffusion region and manages to provide a more open exhaust region than the Sweet-Parker model, which leads to reconnection rates closer to the observed values. Even though many aspects of this model are believed to be essentially correct, the model was found out to not be self-consistent in the MHD model with a uniform resistivity [*Biskamp*, 1986]. However, some progress was made when it was realized that a fluid model with a localized resistivity could produce a Petschek-like reconnection with the associated high rates [*Ugai and Tsuda*, 1977]. If there is a region of higher diffusion near the X point, the magnetic field lines bend in, which gives an open outflow exhaust [*Kulsrud*, 2001]. But it is not clear what could physically be the origin for the existence of a localized resistivity.

Later, other numerical studies focused on steady-state collisionless reconnection found that the local reconnection rate was approximately 0.1, independent of the electron-to-ion mass ratio and the ratio of system size to ion inertia length [*Shay et al.*, 1999]. The Geospace Environment Modeling (GEM) Challenge study carried on to compare simula-

tions with different models, and found that all models with the Hall term (second term in the right-hand side of equation 2.18) had rates comparable to 0.1 [*Birn et al.*, 2001].

Since then, other systems have also been found to have a similar reconnection rate of approximately 0.1, even without the Hall term or a localized resistivity. This leads us to what is called the reconnection rate problem: what is the mechanism that causes the reconnection rate to be such? Is it a coincidence that so many different studies containing different mechanisms give rise to the same rate or is there something more fundamental causing the reconnection rate to be approximately 0.1?

NASA's Magnetospheric Multiscale (MMS) mission was launched on March 12, 2015, in order to study magnetic reconnection [*Burch and Torbert*, 2016; *Burch et al.*, 2016]. It consists of four spacecraft which travel directly through areas near Earth known to be magnetic reconnection sites. The spacecraft fly in an adjustable pyramid formation that enables them to measure magnetic field lines, charged particles and, thus, the structure of magnetic reconnection, in three dimensions. One of the main outstanding questions that MMS plans to answer is what determines the rate at which reconnection occurs, which means that, in synergy with modelling, the MMS mission might help us understand the inner workings of this fundamental question.

Chapter 3

The scientific problem and approach

Magnetic reconnection plays an important role in the dynamics of the magnetosphere. It allows particles and energy from the solar wind to enter the magnetosphere and the magnetospheric topology to change depending on the direction of the IMF. In a resistive magnetohydrodynamic description, it is the dissipation region that controls the rate of reconnection [*Birn et al.*, 2001].

The purpose of this thesis is to study how fast can the reconnection rate go in a fluid-based simulation setup with varying levels and shapes of resistivity. Our tool of investigation is a 2.5D (two spatial dimensions [x and z] and three velocity and field dimensions [x, y and z]) resistive MHD simulation, invariant in the y direction, which will be used to obtain solutions to the magnetohydrodynamic equations presented in the previous chapter. The variation of the reconnection rate as well as some other output variables will be analyzed while changing the value of two different parameters: the magnitude and the shape of the resistivity.

In this chapter, we will present the main goal of this thesis and describe the method that has been used to study it, as well as the steps made to obtain the results.

3.1 Approach to the problem

Magnetic reconnection in two dimensions in a simple Harris sheet equilibrium has been previously investigated using different simulation models, including MHD, Hall MHD, hybrid (electrons are treated as fluid and ions as particles), and full particle (particle-in-cell ions and electrons) [*Birn et al.*, 2001].

In this thesis we intend to study how the reconnection rate responds to modifications

of the magnitude and shape of a localized resistive region. For the goal of this study it is sufficient and more practical to use a resistive MHD simulation.

3.1.1 Simulation set up

The code, written in Fortran, solves the time dependent resistive MHD equations using an explicit finite-difference method. More on this has previously been described in detail by *Birn and Hones Jr.* [1981], but an overview of the numerical procedure will be presented in the following section.

The whole simulation takes place in a domain large enough so that any boundary effects will not intervene with the reconnection process. This corresponds to a box of 400×200, with x going from 0 to 400 and z from -100 to 100. For most of the runs, these dimensions correspond to a resolution of 3200×1600 cells. The boundary conditions consist of solid and ideally conducting walls at the top and bottom of the box, while the left and right walls have been defined with periodic conditions. To visualize the characteristics of these boundaries let's imagine a plasma element moving towards the left wall. For periodic boundaries, a plasma element crossing the left boundary reappears on the right side boundary with the same properties. Such boundary conditions means that the properties across the boundaries are periodic, and the simulation domain can be visualized as a torus. For the top and bottom boundaries, any plasma element with an outbound velocity will be reflected. In such a simulation setup, no mass, momentum or energy is lost through the boundaries.

The code runs on the Alfven timescale, where $t = L/v_A$. L is the characteristic length, which corresponds to the distance an Alfvén wave can travel in a time unit. The computation is done every timestep $dt = 0.0125$.

The total resistivity, η, consists of a background resistivity (η_0) plus an exponential function in the center of the box. It is given by

$$\eta/\omega = \eta_0 + \eta_1 e^{-\left[\left(\frac{x-x_0}{L_x}\right)^2 + \left(\frac{z-z_0}{L_z}\right)^2\right]}, \tag{3.1}$$

where η_1 determines the peak magnitude of the resistivity. $z_0 = 0$ and $x_0 = x_{max}/2$ determine the location of the resistive region, and L_x and L_z determine the shape of the resistive spot. If they both have the same value, the resistivity will have a circular shape, and it will turn to an ellipse in the x or z direction if one is larger than the other. The parameter ω is used as a scaling factor for the resistivity and will remain invariant during the whole study.

Figure 3.1b shows the profile of the resistive spot as a function of x, with the values written in table 3.1.

Apart from the resistivity, which is time independent, some initial configurations for the magnetic field, pressure, current density and mass density will be imposed. These will

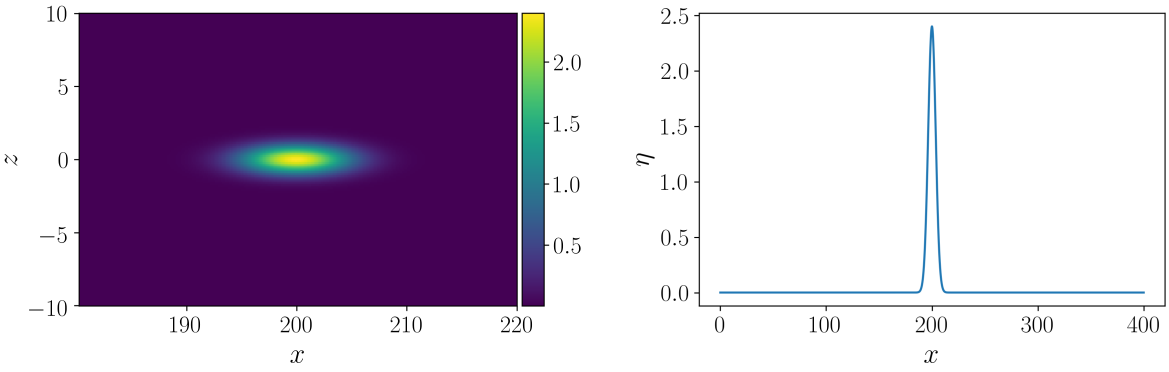

(a) $\eta(x, z)$ (b) $\eta(x)$

Figure 3.1: To the left, magnitude of the resistive spot given by equation 3.1 as a function of x and z. To the right, profile of the magnitude of the resisitive spot as a function of x. Both with the values written in table 3.1

ω	η_0	η_1	x_0	z_0	L_x	L_z
0.3	0.005	8	$x_{max}/2$	0	5	1

Table 3.1: Values taken for the resistivity corresponding to equation 3.1.

follow a simple Harris sheet equilibrium, which will be explained in more detail in Section 3.2.

3.1.2 Scientific approach

The goal of this thesis is to determine how fast can the reconnection rate go, by modifying the finite resistivity that has been described in the previous subsection. In order to do so, we approach the problem from two different perspectives.

First, we study the impact of changing the magnitude of the resistivity. This means giving different values to the parameter η_1 defined in the equation 3.1. 16 different values are taken inside the range 0.01-8 to perform this study.

The second approach to the problem is to change the aspect ratio of the resistive spot. As it can be seen from the expression 3.1, it is the parameters L_x and L_z that should be modified in order to achieve what we want. L_z is kept constant with a value $L_z = 1$ and 16 different values of L_x are studied within the range 0.5-40.

Figure 3.2 shows the values of η_1 and L_x for all the runs made. The study in which we change the value of the magnitude of the resistivity is represented in color orange. The aspect ratio taken for this study is equal to 5 ($L_x = 5$ and $L_z = 1$). The blue stars represent the study in which the aspect ratio is being modified, and the value of η_1 for this study is taken at 8.

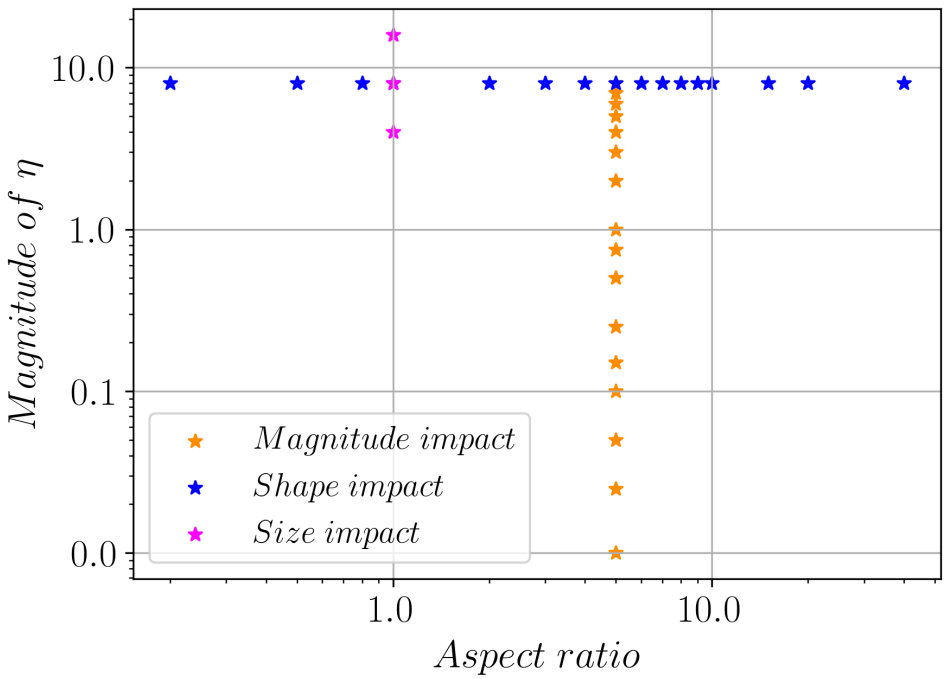

Figure 3.2: Distribution of the runs as a function of the aspect ratio (L_x/L_z) and magnitude (η_1) of their resistive spot. In orange, the runs corresponding to the first study, in which the magnitude is changed. In blue, the runs corresponding to the second study, in which the aspect ratio is varied. In magenta, the runs in which the size of the resistive spot is changed keeping a constant Lundquist number.

The three runs marked in color magenta in Figure 3.2 are discussed in Chapter 5. They are taken with a constant Lundquist number but changing the size of the resistive spot. Thus, the aspect ratio is kept the same and the value of η is varied with the value of λ (or L_z in our case) so that S is kept constant (see equation 2.23).

3.2 Overview of the numerical procedure

In this section we will describe the initial conditions of our simulation, and we will explain the integration method that is used in order to obtain solutions to the equations.

Some additional literature on the numerical approach of resistive MHD models can be found in *Schindler* [1972]; *Birn et al.* [1975]; *Birn* [1980].

3.2.1 Initial conditions

As we mentioned before, the initial magnetic field configuration is a two-dimensional Harris-type equilibrium [*Birn et al.*, 1996]. Its components are given by

$$B_x = \tanh(z) \tag{3.2}$$

$$B_y = B_z = 0 \tag{3.3}$$

This initial magnetic field has only x-component, which is positive above the X-line and negative below it. It can be visualized like the case $t < 0$ in Figure 2.3. Note that the magnitude of the magnetic field, as well as the length unit are normalized to 1. Normalized quantities are being used in the whole code since MHD allows us to work in adimensional quantities.

Since $\mathbf{j} = \nabla \times \mathbf{B}$, the initial current density and, thus, the particle density must be of the form

$$j_y = \frac{1}{\cosh^2(z)} \tag{3.4}$$

$$\rho = \frac{1}{\cosh^2(z)} + \rho_{lobe} \tag{3.5}$$

Figure 3.3 shows the current density before any reconnection is happening. It follows the dependence with z written in equation 3.4.

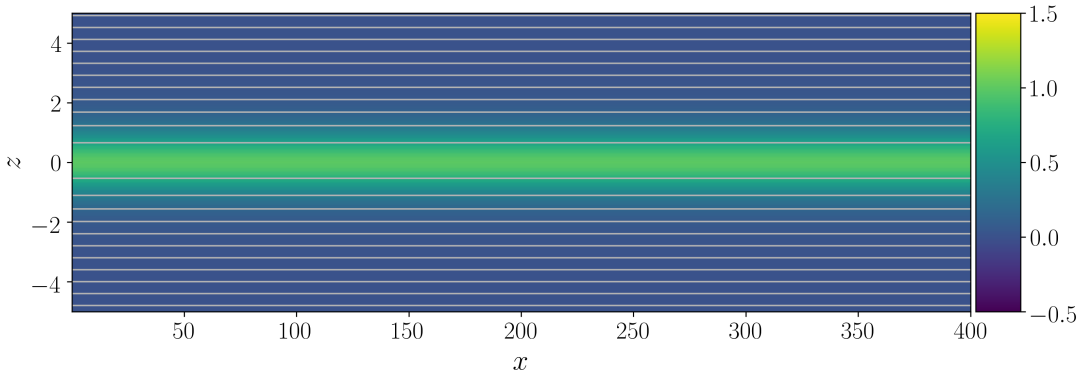

Figure 3.3: Current density and magnetic field lines at t=0.

The plasma pressure is given by $p = \rho T$, where T is the sum of the electrons and ions temperature, $T = T_i + T_e$, and it's taken equal to 0.5. Then we are left with

$$p = \frac{1}{2}\frac{1}{\cosh^2(z)} + p_{lobe} \tag{3.6}$$

where $p_{lobe} = T\rho_{lobe}$ is the pressure in the lobes. Assuming force balance, the plasma

pressure together with the magnetic pressure, p_B, must stay constant (see equation 2.27), so that $\nabla(p + B^2/2) = 0$. It can be seen how the dependence on z vanishes by calculating the magnetic pressure:

$$p_B = \frac{B_x^2}{2} = \frac{1}{2}\tanh^2(z) = \frac{1}{2}\left(1 - \frac{1}{\cosh^2(z)}\right)$$

3.2.2 Integration method

As mentioned, our code uses an explicit finite difference scheme to solve the resistive MHD equations. In this section, we present the equations in the form that the code uses them, and we will show how they are solved inside the program.

The magnetohydrodynamic (MHD) equations have been presented in Section 2.4. They consist of equations 2.15 to 2.18, which correspond to the mass continuity equation, the equation of motion, Ohm's law and the equation of state, which are coupled to Maxwell's equations (equations 2.7 to 2.4). In this section, we will write all the needed equations in their conservational form, in order to perform spatial discretization in the integration scheme.

The first equation that we need is the one for the conservation of mass, which is equation 2.15, already written in the conservational form. We rewrite it here:

$$\frac{\partial \rho}{\partial t} + \nabla \cdot (\rho \mathbf{v}) = 0 \tag{2.15}$$

ρ is the mass density.

The next equation that we will need is the momentum conservation equation, which is equivalent to equation 2.16. Written in the conservational form it looks like the following expression:

$$\frac{\partial}{\partial t}(\rho \mathbf{v}) = \nabla \cdot (\rho \mathbf{v}\mathbf{v}) - \nabla \cdot \mathbf{P} + \mathbf{j} \times \mathbf{B} \tag{3.7}$$

This equation can be simplified a lot by defining two quantities. First, lets define the momentum flux density tensor of the bulk velocities as $\mathbf{S} \equiv \rho \mathbf{v}\mathbf{v}$. The last term can also be written as the divergence of a tensor. To do so, we need to replace the current density using Ampères law, $\mathbf{j} = \nabla \times \mathbf{B}$, so that the last term in equation 3.7 is just $(\nabla \times \mathbf{B}) \times \mathbf{B}$. By doing some algebra, we are able to write this quantity as the divergence of a tensor defined as following:

$$M_{ij} \equiv \frac{1}{\mu_0} B_i B_j - \frac{1}{2\mu_0} B^2 \delta_{ij} \tag{3.8}$$

This is the so called *Maxwell Stress Tensor*.

Equation 3.7 can then be written as:

$$\frac{\partial}{\partial t}(\rho \mathbf{v}) - \nabla \cdot \big(\mathbf{S} - \mathbf{P} + \mathbf{M}\big) = 0 \tag{3.9}$$

which now has the same form as equation 2.15.

Our study is based on resistive MHD, which means that the third equation that we will use will not be the Generalized Ohm's Law (eq. 2.18), but equation 2.19. However, we also want it in a conservational form, so we will need to combine it with Faraday's Law. Thus, inserting equation 2.19 into 2.6 we obtain the time variation of the magnetic field:

$$\frac{\partial \mathbf{B}}{\partial t} = -\nabla \times \mathbf{E} = \nabla \times (\mathbf{v} \times \mathbf{B} - \eta \mathbf{j})$$

This equation is known as the *Induction equation*:

$$\frac{\partial \mathbf{B}}{\partial t} = \nabla \times (\mathbf{v} \times \mathbf{B}) - \eta \nabla \times \mathbf{j} - \nabla \eta \times \mathbf{j}. \tag{3.10}$$

where the second term in the RHS can also be written as $\eta \nabla^2 \mathbf{B}$ using Ampères law.

The only equation that we are missing is the equation of state (eq. 2.17), which tells us that the pressure evolves in a similar way as the density. Combining the equation of state (remember that the total derivative is defined as $\frac{d}{dt} = \frac{\partial}{\partial t} + \mathbf{v} \cdot \nabla$) with the mass conservation equation (eq. 2.15), we obtain the following expression:

$$\frac{\partial p}{\partial t} + \mathbf{v} \cdot \nabla p + \gamma p \nabla \cdot \mathbf{v} = 0 \tag{3.11}$$

which describes the ideal evolution of the pressure, without considering sources or sinks. However, there is a contribution of a dissipation term in the evolution of the thermal energy that we need to account for. The conservation law for the thermal energy is written as:

$$\frac{\partial}{\partial t} \frac{p}{\gamma - 1} + \nabla \cdot \left[\Big(\frac{\gamma}{\gamma - 1} p \Big) \mathbf{v} \right] + \mathbf{v} \cdot \nabla p = \mathbf{j} \cdot \mathbf{E}' \tag{3.12}$$

where $\mathbf{j} \cdot \mathbf{E}'$ is the dissipation term which accounts for all the non-ideal terms in the Ohm's law. In resistive MHD simulations like ours, the dissipation term is represented by *Ohmic heating*, ηj^2. This fact is easy to see, since the only non ideal term in the Ohms law is the resistive term, so that $\mathbf{E}' = \eta \mathbf{j}$. Rewriting equation 3.12 in the same form as 3.11 we obtain:

$$\frac{\partial p}{\partial t} + \mathbf{v} \cdot \nabla p + \gamma p \nabla \cdot \mathbf{v} = (\gamma - 1) \eta j^2 \tag{3.13}$$

In order to get an equation in a conservational form, the code introduces a new quantity, u, as:

$$u = p^{1/\gamma} \tag{3.14}$$

which can be thought of as the internal energy. Applying this change of variable to the expression written in 3.13, we get the expression that is solved in the code:

$$\frac{\partial u}{\partial t} = -\nabla \cdot (u\mathbf{v}) + \frac{\gamma - 1}{\gamma} u^{1-\gamma} \eta j^2$$

Let's gather all the equations that the code will be solving:

$$\textcircled{1} \quad \frac{\partial \rho}{\partial t} = -\nabla \cdot (\rho \mathbf{v}) \tag{3.15}$$

$$\textcircled{2} \quad \frac{\partial}{\partial t}(\rho \mathbf{v}) = \nabla \cdot \big(\mathbf{S} - \mathbf{P} + \mathbf{M}\big) \tag{3.16}$$

$$\textcircled{3} \quad \frac{\partial \mathbf{B}}{\partial t} = \nabla \times (\mathbf{v} \times \mathbf{B}) + \eta \nabla^2 \mathbf{B} - \nabla \eta \times \mathbf{j} \tag{3.17}$$

$$\textcircled{4} \quad \frac{\partial u}{\partial t} = -\nabla \cdot (u\mathbf{v}) + \frac{\gamma - 1}{\gamma} u^{1-\gamma} \eta j^2 \tag{3.18}$$

In order to solve these equations, the code uses an explicit finite difference method. This means that we will use the present values of the variables on the right hand side to find the future values of the variables on the left hand side of equations 3.15 to 3.18. Let's try to explain this using equation ① as an example.

Let us define

$$s_i^n(x,z) \equiv \rho^n(x,z) v_i^n(x,z) \; ; \quad i = x, y, z \tag{3.19}$$

to simplify things. Note that n represents the current timestep and (x, z) represents the current location in the grid. Equation 3.15 in the method that we are using will then be written as:

$$\frac{\rho^{n+1}(x,z) - \rho^n(x,z)}{\Delta t} = -\frac{s_x^{n+1/2}(x+1,z) - s_x^{n+1/2}(x-1,z)}{2\Delta x} - \frac{s_z^{n+1/2}(x,z+1) - s_z^{n+1/2}(x,z-1)}{2\Delta z} \tag{3.20}$$

Which means that to find the future value $(n+1)$ of the mass density at the location (x, z) we will have to compute the following:

$$\rho^{n+1}(x,z) = \rho^n(x,z) - \Delta t \left[\frac{s_x^{n+1/2}(x+1,z) - s_x^{n+1/2}(x-1,z)}{2\Delta x} + \frac{s_z^{n+1/2}(x,z+1) - s_z^{n+1/2}(x,z-1)}{2\Delta z} \right] \tag{3.21}$$

and loop around the whole grid in order to get the value of ρ in the entire the simulation domain. Note that, to find the future value of ρ, we are using the values of s_x and s_z at an intermediate time $n+1/2$, which is between n and $n+1$. The code resolves every timestep using two integration steps (or iterations). The first step pushes the variables from $n-1/2$ to $n+1/2$ using the values at n, and the second step uses the value of $n+1/2$ to push the variables from n to $n+1$. In Figure 3.4 we have illustrated this leapfrog-method, where the left panel represents the current timestep, together with the values at $n+1/2$, and the right panel represents the future timestep.

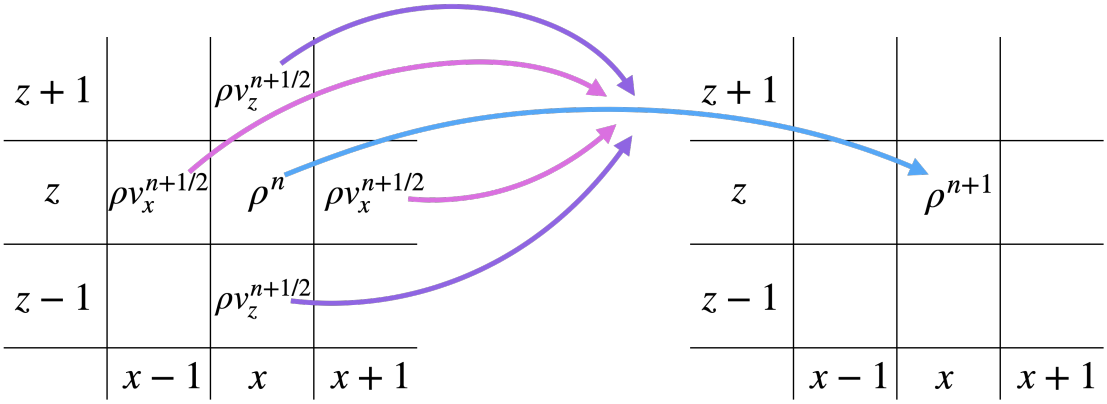

Figure 3.4: Illustration of the explicit finite difference method. The grid to the right represents the future value, extrapolated from all the present values in the left grid using the relation 3.21.

The code solves the equations in the order in which we have written them in ① to ④. First, it pushes the value of ρ forward using the current value of $\rho\mathbf{v}$ as we just explained. Then, with equation 3.16, it finds the future value of $\rho\mathbf{v}$ using the present values of $\mathbf{B}$, $\rho\mathbf{vv}$ and P. This step is split into two parts. First, it adds the contribution of the pressure and the second half of the Maxwell stress tensor as written in 3.8 to the future quantity, and then it proceeds to add the contribution of the bulk velocities tensor and the second half of the Maxwell stress tensor (see expression 3.25).

Next, it calculates the new value of $\mathbf{B}$ with the current values of $\mathbf{v}\times\mathbf{B}$, $\mathbf{B}$ and $\mathbf{J}$ using the relation written in 3.17, and finally, using equation 3.18, it updates the value of the pressure. After all these steps, the future velocities are easily set by using the value of $\rho\mathbf{v}$ found with 3.16 and dividing by the value of ρ found in 3.15 as following:

$$v_i^{n+1}(x,z) = \frac{s_i^{n+1}(x,z)}{\rho^{n+1}(x,z)}\ ; \quad i = x,y,z. \tag{3.22}$$

Regarding the current density, $\mathbf{j}$, there is not an actual "push" of this quantity. It is calculated from $\mathbf{B}$ by Ampères law ($\mathbf{j} = \nabla\times\mathbf{B}$) every time that it is used. The components

are computed as written in equation 3.23.

$$\begin{aligned} j_x^n =& -\frac{B_y^n(x,z-1) - B_y^n(x,z+1)}{2\Delta z} \\ j_y^n =& \frac{B_x^n(x,z-1) - B_x^n(x,z+1)}{2\Delta z} - \frac{B_z^n(x-1,z) - B_z^n(x+1,z)}{2\Delta x} \\ j_z^n =& \frac{B_y^n(x-1,z) - B_y^n(x+1,z)}{2\Delta x} \end{aligned} \tag{3.23}$$

The expressions written in 3.24 to 3.27 intend to illustrate which quantities are used and which quantities are pushed forward at each timestep. The numbers ① to ⑤ relate them to the equations 3.15 to 3.18 and 3.22 and indicate the order in which the code solves them.

$$① \quad \left.\begin{matrix} \rho^n \\ \nabla\cdot(\rho\mathbf{v})^{n+1/2} \end{matrix}\right\} \Rightarrow \boxed{\rho^{n+1}} \tag{3.24}$$

$$② \quad \left.\begin{matrix} (\rho\mathbf{v})^n \\ \nabla p^{n+1/2} \\ \nabla (B^{n+1/2})^2/2 \end{matrix}\right\} \Rightarrow (\rho\mathbf{v})'^{n+1} \; ; \quad \left.\begin{matrix} (\rho\mathbf{v})'^{n+1} \\ \nabla\cdot(\rho\mathbf{v}\mathbf{v})^{n+1/2} \\ \nabla\cdot B_i^{n+1/2} B_j^{n+1/2} \end{matrix}\right\} \Rightarrow \boxed{(\rho\mathbf{v})^{n+1}} \tag{3.25}$$

$$③ \quad \left.\begin{matrix} \mathbf{B}^n \\ \nabla\times(\mathbf{v}^{n+1/2}\times\mathbf{B}^{n+1/2}) \\ \eta\nabla^2 B^{n+1/2} \\ \nabla\eta\times j^{n+1/2} \end{matrix}\right\} \Rightarrow \boxed{\mathbf{B}^{n+1}} \Rightarrow \mathbf{j}^{n+1} \tag{3.26}$$

$$④ \quad \left.\begin{matrix} u^n \\ \nabla\cdot(u^{n+1/2}\mathbf{v}^{n+1/2}) \\ \frac{\gamma-1}{\gamma}(u^n)^{1-\gamma}\eta(j^{n+1})^2 \end{matrix}\right\} \Rightarrow \boxed{\mathbf{u}^{n+1}} \Rightarrow \mathbf{p}^{n+1} \tag{3.27}$$

In Figure 3.5, we have drawn a flow chart. The numbers represent the equations ① to ⑤ and the green arrows indicate in which order they are being solved in the code, going from one run (n) to the next one$(n+1)$. The orange arrows indicate which quantities are being used for the computation of the other quantities, following the expressions 3.24 to 3.27.

3.2.3 Output

We have now explained which are the initial conditions of our simulation and how does the code solve the equations. The equations are solved pushing the quantities a $dt = 0.0125$ forward each time, and the code runs to a maximum time of $t = 150$. If we were to have a data file for each timestep, this would result in a larger amount of data than the one we can process. For this reason, the code prints a data file every $dt = 2$, which gives us a total

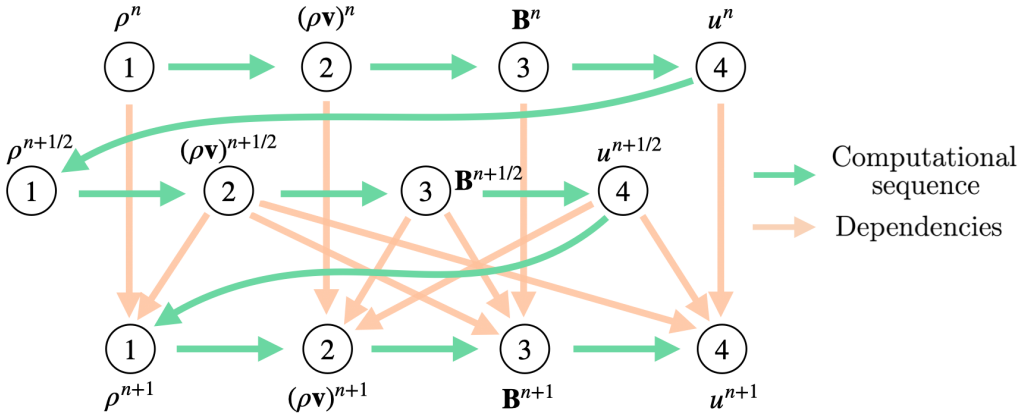

Figure 3.5: Integration method flow chart. The green arrows indicate the order in which the equations are solved. The orange arrows indicate which variables are used to compute the new quantities, as written in the expressions 3.24 to 3.27.

of 76 data files.

The content of these files consists on encrypted values, arrays and matrices of the quantities computed by the method described in the previous subsection. The quantities that appear in the output files as matrices of $n_x \times n_z$ (most of the times corresponding to 1600×3200) are:

- The resistivity: η
- The mass density: ρ
- The velocity components: v_x, v_y, v_z
- The magnetic field components: B_x, B_y, B_z
- The internal energy: u

The rest of quantities, such as the current density, the energy or the reconnection rate, will be calculated afterwards in order to carry out the analysis.

Chapter 4

Results

In this chapter, we perform an analysis of the data obtained from the different runs of the simulation mentioned previously. We perform two different sets of runs. In the first set, we vary the magnitude of the resistive spot while leaving the size of the diffusion region invariant. In the second set of runs, we vary the shape of the resistive spot, making it more circular or elongated, while leaving the magnitude of the resistivity invariant.

We begin this chapter by showing the general behaviour of a sample run to demonstrate how the ensemble of runs is analyzed. This includes describing the time evolution of the current density, the conversion of magnetic energy into kinetic and thermal energy, and the origin of E_y in the different regions of the box. Additionally, we analyze how the reconnected flux and the reconnection rate vary for each set of runs, and we explain their behaviours with the study of the profile of j_y, as well as the variation of the different components of the magnetic field. Finally, we analyze the opening angle of the separatrix for 4 different aspect ratios, and we compare the results to the ones obtained by *Liu et al.* [2017].

4.1 Sample evolution

In this section, one of the runs will be discussed for the purpose of getting a general overview and understanding of the simulation layout and evolution. The run presented has $\eta_1 = 8$ and an aspect ratio of 5. This run is included in our analysis of how the magnitude impacts the rate, and in the analysis of how the shape influences the rate (Figure 3.2). The additional quantities needed to define η are written in table 3.1.

Figure 4.1 shows the out-of-plane current density j_y (color) and the in-plane magnetic field (B_x, B_z) lines for four different stages of the evolution. At $t = 2$, we can already

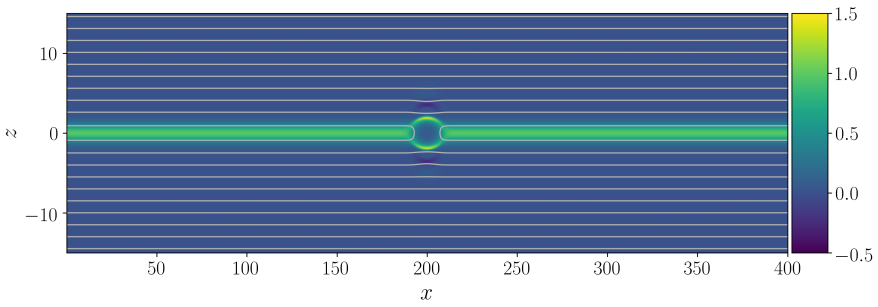

(a) t=2

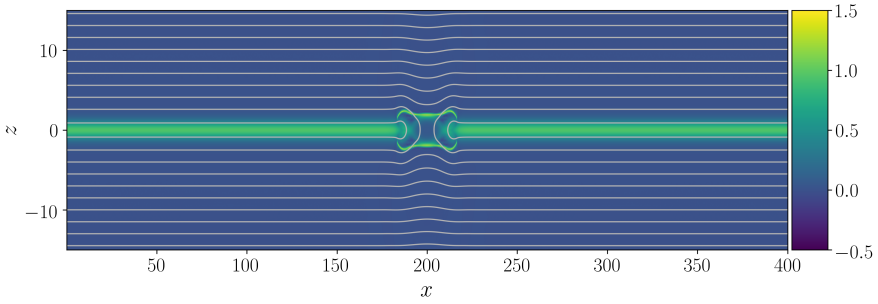

(b) t=10

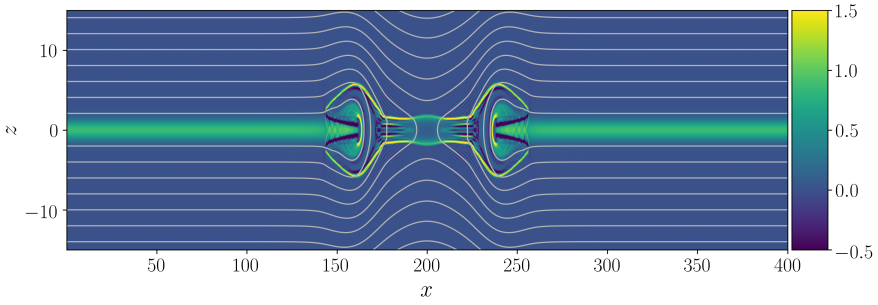

(c) t=40

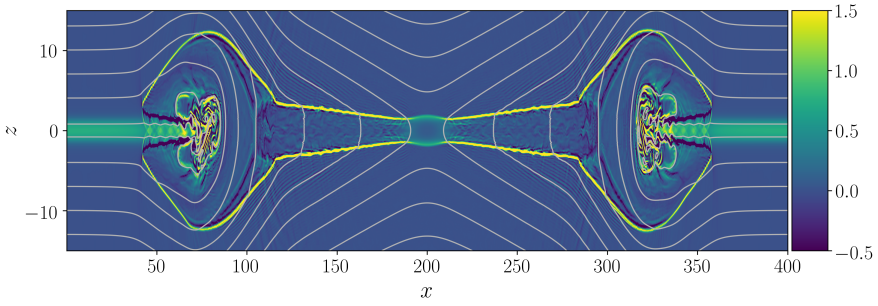

(d) t=100

Figure 4.1: j_y with magnetic field lines for different stages of the evolution.

observe a perturbation of the current sheet at the X point due to the high resistivity present. For later timesteps, the perturbation has evolved, and a reconnection region has developed. At $t = 10$ an outflow region has formed. The reconnection process is now in the so-called fast phase. The reconnection rate peaks at about $t = 26$. Fresh magnetic field lines with plasma from the inflow region are dragged in to compensate for the plasma pressure convected away by the outflow. Later, at $t = 40$, we see clear outflow structures moving towards the two sides. At this time the inflowing magnetic field lines are considerably deformed as a consequence of their expansion towards the reconnection region. This effect is amplified by the outflow structures expanding outward into the inflow region. At $t = 100$ the outflow structures are approaching the boundaries of our simulation domain. The reconnection process has, at this time, converted a significant amount of the available magnetic energy in the inflow region, which results in a consistently slower and slower rate.

Our primary interval of investigation is between $t = 10$ and $t = 40$, which is when the system reaches its peak rate. In addition, our interest lies in the diffusion region and its nearest surroundings, and we will not focus on the outflow dynamics and structures. More on this has been studied and described by *Zenitani et al.* [2009].

Taking a closer look at the central region, where the reconnection process operates, and plotting the inflow and outflow velocities (see Figure 4.2), we can clearly see how the plasma moves towards the reconnection point above and below the current sheet (Figure 4.2a), and how it moves away from the X point with much higher velocities in the outflow region (Figure 4.2b). This means that a process inside this region accelerates the plasma. This acceleration has to be at the expense of magnetic energy.

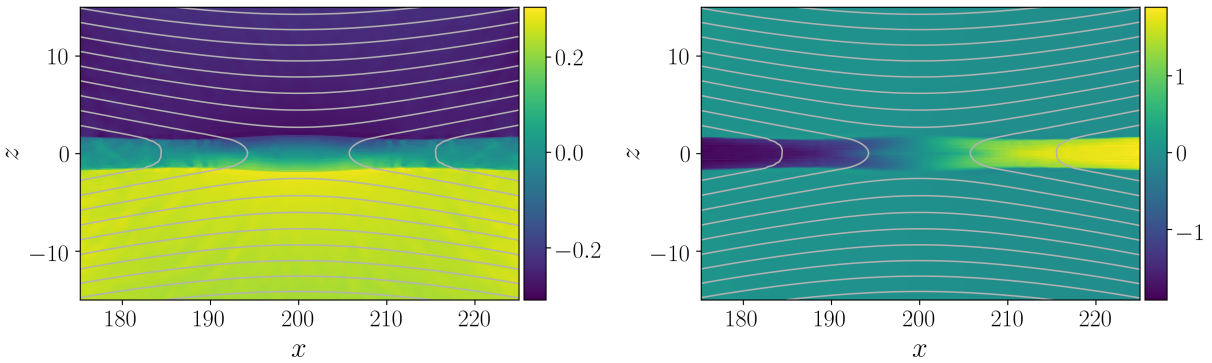

(a) v_z (b) v_x

Figure 4.2: Inflow and outflow velocities at the timestep 50

.

As we mentioned in Section 2.5, reconnection is a process for which magnetic energy is converted into kinetic and thermal energy. Thus, the increase in kinetic energy shown in Figure 4.2 has its origin in the magnetic energy reservoir in the inflow region. Figure 4.3a

shows the magnetic energy, which is defined as $\frac{B^2}{2\mu_0}$ ($\frac{B^2}{2}$ in our case), to prove that in the inflow region it is much higher than in the outflow region. In this figure we can also point out that the magnetic field is close to zero along the entire current sheet, as a result of the field reversal (the normal component of the magnetic field, B_z, is small).

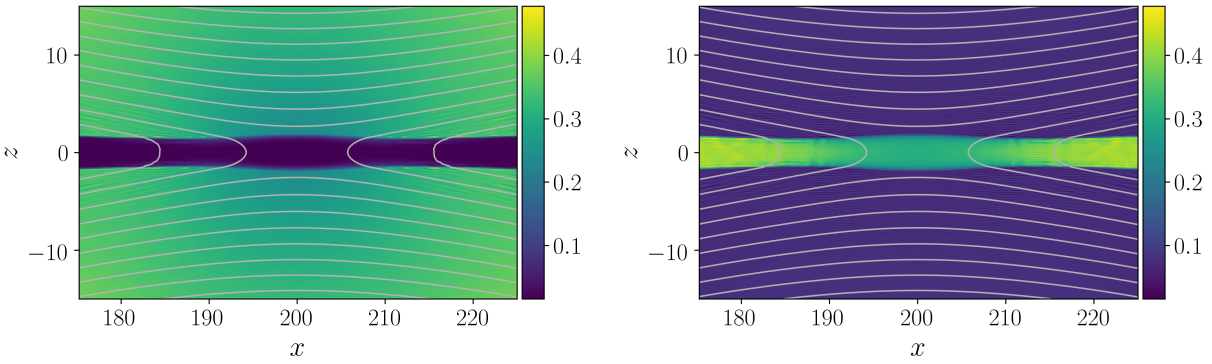

(a) $B^2/2$ (b) p

Figure 4.3: Magnetic energy and pressure at the timestep 50.

Figure 4.3b shows that the pressure and, consequently, the thermal energy are dominating in the current sheet. The magnetic energy outside is balanced by the pressure in the current sheet. This force balance is described in Section 2.6.

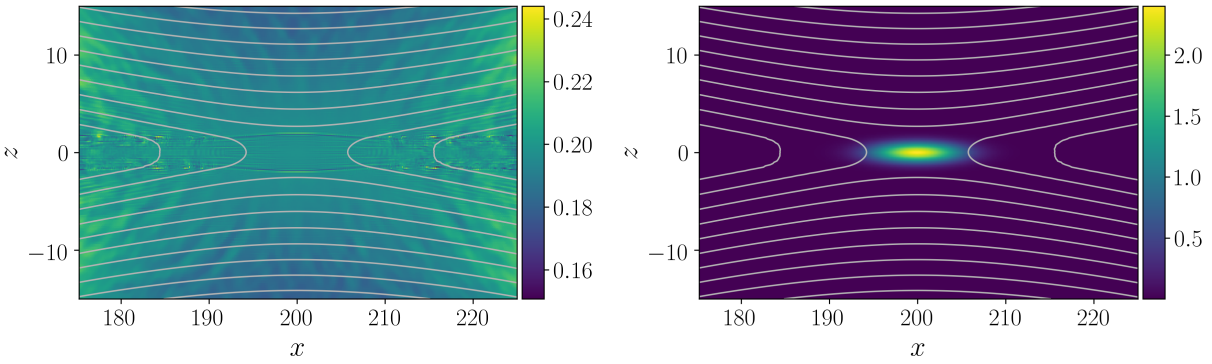

(a) E_y (b) η

Figure 4.4: y component of the electric field and resistivity at the timestep 50.

In Figure 4.4a we have plotted the y component of the electric field obtained using the resistive Ohm's Law: $E_y = \eta j_y - (\mathbf{v} \times \mathbf{B})_y$. We can observe a rather uniform behaviour of it, even though we have a very high resistivity in the center of the box (Figure 4.4b). Due to the fact that there is a resistivity in the center, the term that dominates E_y inside the diffusion region is ηj_y. Outside the diffusion region, the term that dominates E_y is $\mathbf{v} \times \mathbf{B}$,

which goes to zero at the X point and decreases significantly around it at the same rate at which ηj_y increases.

This fact can be more clearly seen in Figure 4.5, where the profile of both terms and the sum of them at the two cuts that pass through the center of the box in the x and z directions have been plotted. In both plots, we can appreciate a similar behaviour of the three quantities: the terms ηj_y and $\mathbf{v} \times \mathbf{B}$ have the same profile with the same magnitude, but one opposite to the other, so that when $\mathbf{v} \times \mathbf{B}$ is at its maximum (outside of the diffusion region) then ηj_y is zero, and vice-versa. As a consequence, E_y is practically constant, with some instabilities around where its two components intersect each other. In the region where $\mathbf{v} \times \mathbf{B}$ dominates, the magnetic field is convected with the plasma. This means that the term ηj_y is crucial for reconnection to occur, allowing the magnetic field to diffuse across the plasma and, thus, new magnetic connections to be formed.

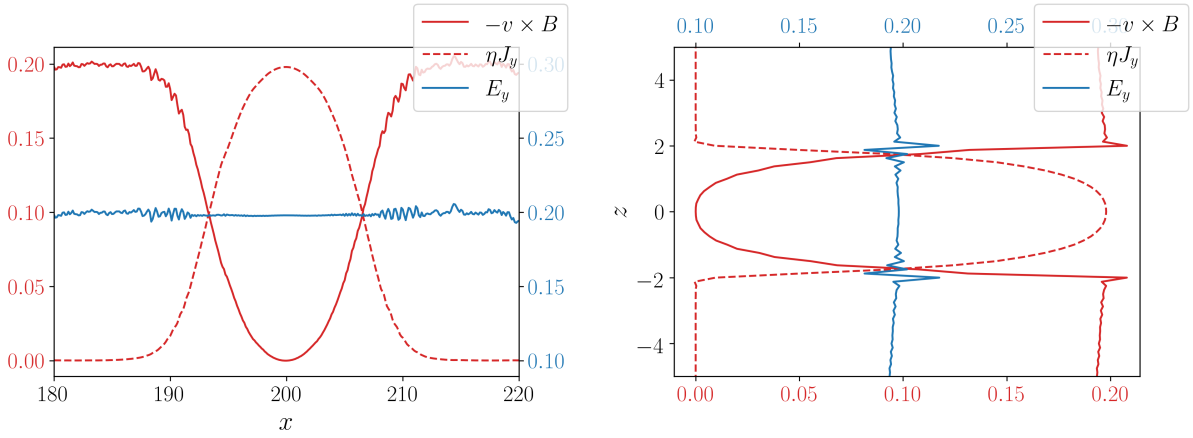

(a) Cut at $z = 0$

(b) Cut at $x = 200$

Figure 4.5: Terms of the resistive Ohm's Law as a function of x and z in the center of the box for the timestep 50.

4.2 Impact of the magnitude of the resistive spot

Our goal is to study how does the reconnection rate vary by changing the magnitude and the shape of the resistive region. In this section, we will vary the magnitude of the resistive spot and analyze which effects these variations have on the system.

The resistivity in our problem is given by equation 3.1. We will change its magnitude by changing the value of η_1, taking values between 0.01 and 8, like explained in Section

3.1.2. The rest of the values which define η will be the same as the ones written in table 3.1.

4.2.1 Reconnection rate vs amplitude of the resistivity

In this section, we study the influence of the magnitude of the resistive spot on the reconnection rate. We vary the magnitude of η from 0.003 ($\eta_1 = 0.01$) to 2.4 ($\eta_1 = 8$), corresponding to slightly less and more resistive plasmas, respectively. The magnetic flux through a surface A is given by the following expression:

$$\phi = \int_A \mathbf{B} \cdot \hat{A} dA \tag{4.1}$$

Thus, the amount of magnetic flux that has reconnected can be calculated as the change of magnetic flux in the inflow region from $t = 0$.

The reconnection rate can be derived using different methods, as mentioned in Section 2.5. Here we define it as the time derivative of the reconnected flux, $d\phi/dt$.

$$\text{Reconnection rate} \equiv d\phi/dt \quad (= E_y = \eta j_y) \tag{4.2}$$

In Figure 4.6, we have plotted the reconnected flux, ϕ, as a function of time for all the different values of η_1. From this plot, we can extract two main behaviours. The first is that, as the magnitude of η gets larger, the flux reconnects faster. This means that for the same amount of time, there will be a higher amount of reconnected flux for larger magnitude of the resistivity.

The second behaviour that we can observe from Figure 4.6 is that for values of η_1 larger than 4, the slope does not change significantly. We can observe a similar behaviour when we plot the reconnection rate for each of the values of η_1 as a function of time (see Figure 4.7). The reconnection rate is higher for larger magnitudes of the resistivity, but as we increase η_1, the reconnection rate seems to stop increasing, reaching a maximum at around 0.2.

In Figure 4.7, we can also see that for the lowest values of η_1, the maximum reconnection rate is reached much later than for higher values. Thus, for our lowest value of η_1, 0.01, the peak in the reconnection rate is reached after timestep 100, while for $\eta_1 = 8$ the peak is reached at around $t = 24$.

Due to a finite amount of magnetic flux in our simulation domain, the rate consistently decreases after reaching its peak value. Another source of the decrease is back-pressure from the outflow region. The latter is generally not a problem, at the times of our investigation, due to the relative large size of our simulation domain. In both figures (4.6 and 4.7), the data has been cut at timestep 120 and, for some runs (see data for the lowest values of η_1 in Figure 4.7), even before that. The reason for this is that the runs develop some numerical instabilities after some time.

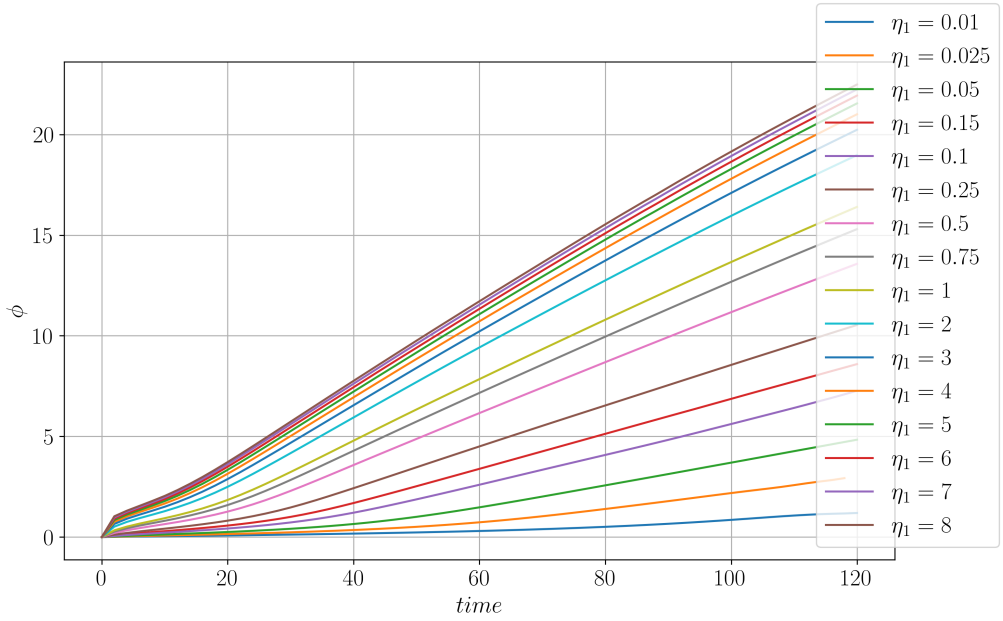

Figure 4.6: Reconnected flux, as a function of time, for different values of the magnitude of the resistive spot

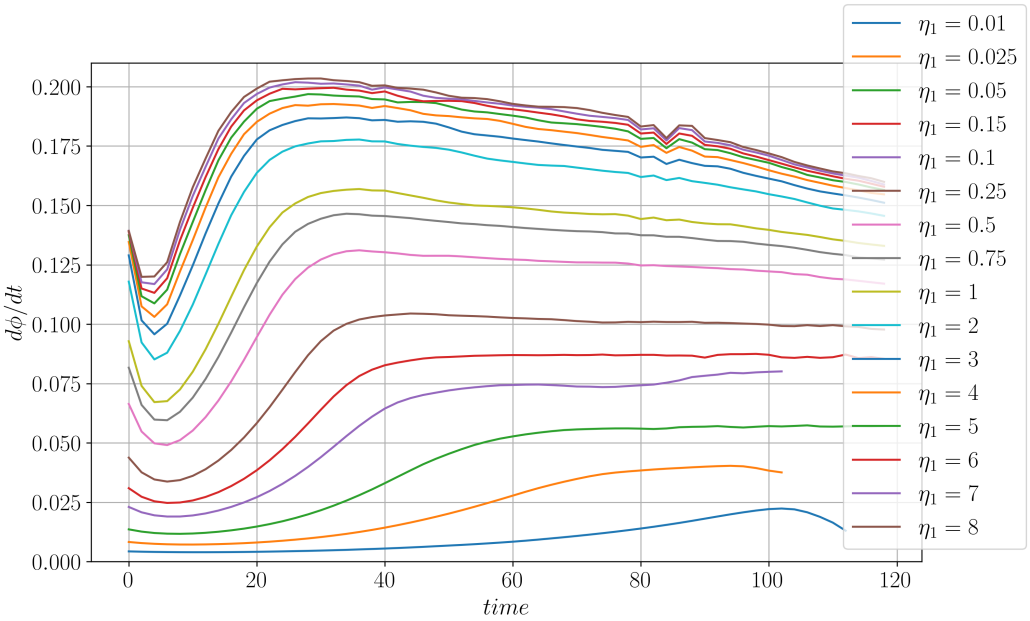

Figure 4.7: Reconnection rate, as a function of time, for different values of the magnitude of the resistive spot

To demonstrate the relationship between the peak reconnection rate and the magnitude of the resistivity, we show in Figure 4.8 the peak rate as a function of η_1. Our estimation of the reconnection rate based on the change of magnetic flux coincides with the more direct measure of extracting E_y at the center of the box, shown in Figure 4.8 as blue and red dots, respectively.

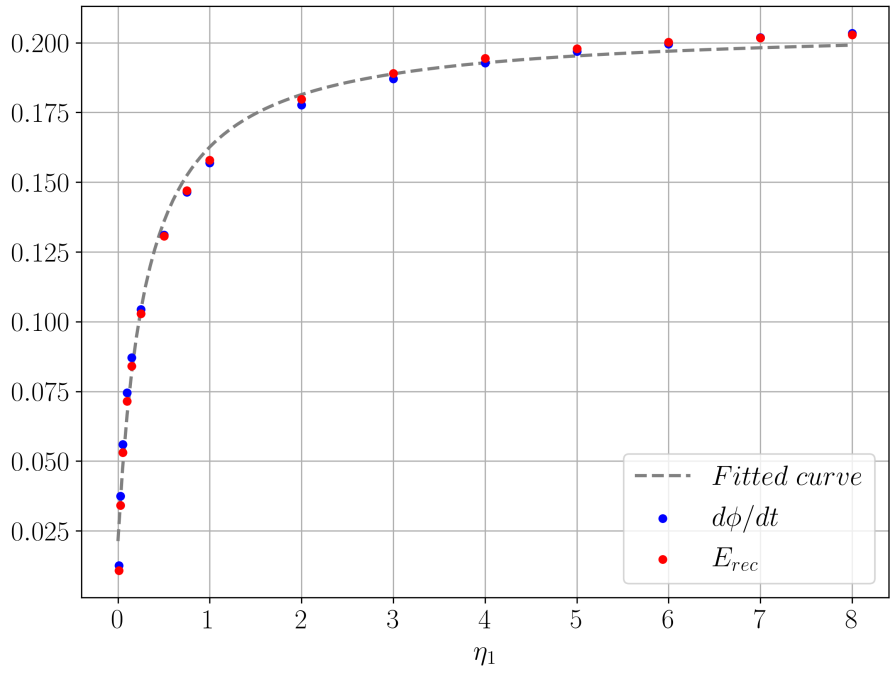

Figure 4.8: Peak reconnection rate, as a function of η_1, as blue dots, peak reconnected electric field, as a function of η_1, as red dots and fitted function as the grey dashed line

In Figure 4.8, we have also plotted as a dashed grey line a function which fits the dots. Equation 4.3 represents this function.

$$f(\eta_1) = a\frac{\eta_1}{b+\eta_1} + c \tag{4.3}$$

where $a = 0.184$, $b = 0.307$ and $c = 0.021$. The functional form is chosen empirically, and thus does not have a direct physical interpretation. However, one can speculate on the physical significance of the obtained values. The value of a relates to the maximum reconnection rate and must have dimensions corresponding to the electric field. The value of b determines how quickly the function converges, and must have dimensions corresponding to η. One can also speculate whether the constant c is related to the uniform background

resistivity, signifying a constant energy conversion throughout the simulation domain. This would correspond to $\eta_1 \to 0$ which would equal to c.

To summarize, for low values of η_1 the reconnection rate is slow, but increases rapidly as η_1 increases. For larger values ($\eta_1 \gtrsim 1$), the rapid increase ceases, and the rate saturates at approximately 0.2. This behaviour illustrates that the effect of increased resistivity can significantly influence the reconnection rate, but only to a certain level. For large values of η_1, the reconnection rate appears to be controlled and limited by other processes. To understand why the rate saturates for high values of η, we investigate the profile of ηj in the next section.

4.2.2 Study of the diffusion region for different peak η

Figure 4.8 showed that the reconnection rate stops increasing significatively even if the magnitude of the resistivity keeps getting larger. The reconnection rate can be written as ηj_y at the center of the box. The fact that the rate saturates while η increases means that j_y must decrease at the center. We will now investigate the current density profiles for 4 different values of η_1.

Figure 4.9 shows 4 different panels in which we have plotted j_y, ηj_y and η, as a function of z, for four different values of η_1. The data is taken along the line $x = 200$, which corresponds to a vertical cut through the X point. For each plot, the two first quantities are represented in color red (j_y in a solid line and ηj_y in a dashed line) with their scale corresponding to the red ticks at the bottom, while the last quantity, η, is plotted as a blue solid line with the magnitude scale given by the blue ticks on the top. The limits are equal in the 4 cases.

From these plots, we can easily see a significant change in magnitude of the resistivity as the value of η_1 increases (blue solid line), as well as a change in ηj_y (red dashed line). The value of ηj_y in the center corresponds to the rates shown in Figure 4.3. However, the most interesting feature of these plots is the current density profile (red solid line).

For $\eta_1 = 0.5$ (panel 4.9a) the current density peaks at the X point, and the relative contribution of j_y to the product ηj_y dominates over that of η. As the value of η_1 starts increasing, however, the current density profile exhibits two distinct peaks, both of which have a higher magnitude than the center value. This bifurcation illustrates that the current density is forced outwards from the center. For panel 4.9b, the relative contribution of η and j_y to ηj_y is approximately the same, but in the last two panels (4.9c and 4.9d), the magnitude of η is so large that j_y has been considerably reduced in the center. Here, the relative contribution of η to the product, is much larger than the one of j_y.

In panels 4.10a and 4.10b, we show 2D plots of the current density for $\eta_1 = 0.5$ and for $\eta_1 = 8$, respectively. This illustrates the bifurcation of the current sheet in the center region for high values of η.

In Figure 4.9, we saw that, for large resitivity, the current density has its maximum at

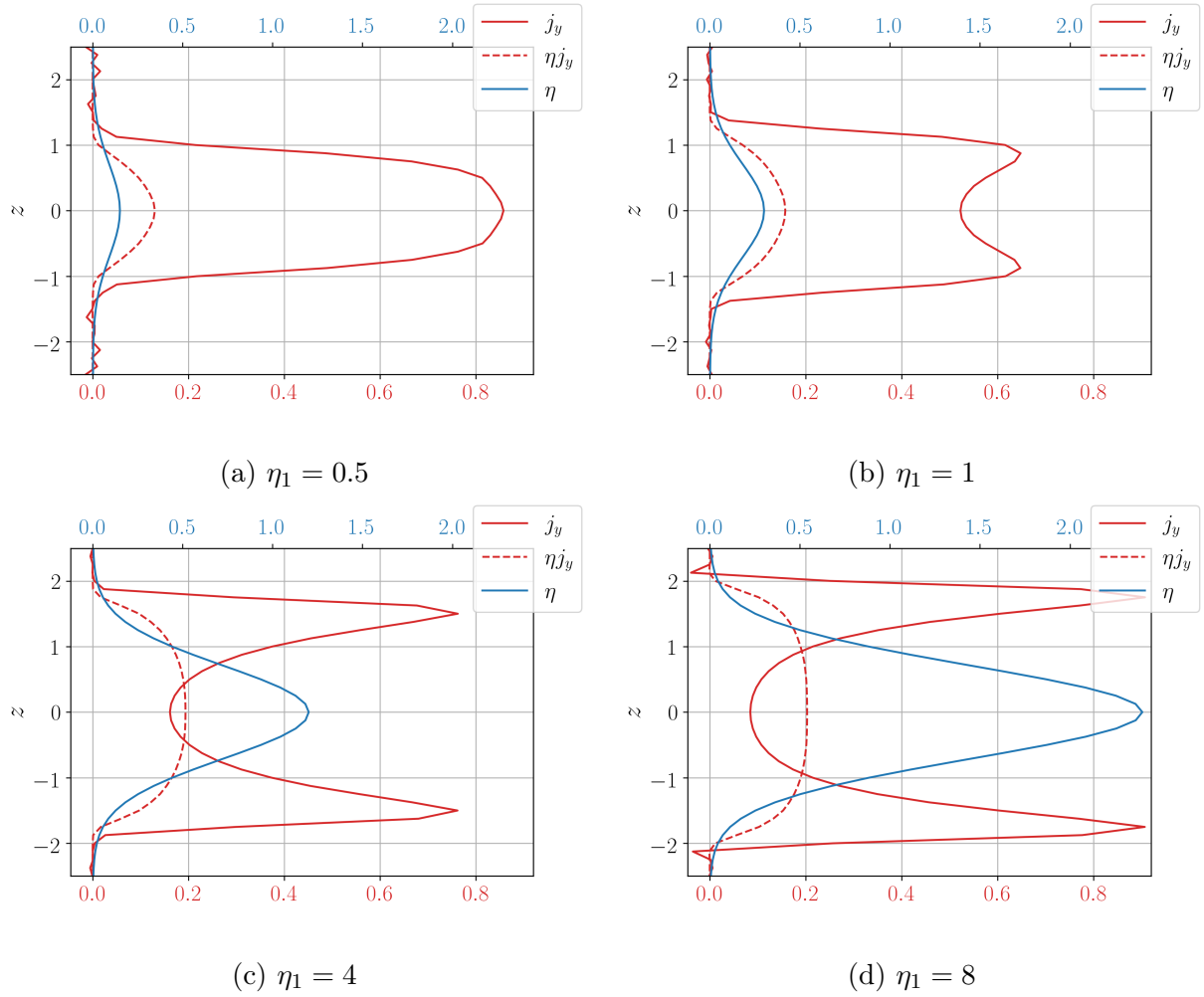

(a) $\eta_1 = 0.5$

(b) $\eta_1 = 1$

(c) $\eta_1 = 4$

(d) $\eta_1 = 8$

Figure 4.9: Resistivity as the blue solid line, current density as the red solid line and reconnection rate as the red dashed line. All of them plotted at x=200 at the time when the reconnection rate is maximum.

the boundary of the resistive region. These current densities are a result of the restructuring of the magnetic field gradients by $\mathbf{j} = \frac{1}{\mu_0}\nabla \times \mathbf{B} \Rightarrow \mu_0 j_y \sim \partial B_x/\partial z$ (equation 2.7). For low values of the resistivity, the gradient is monotonically increasing towards the center.

To determine how the system reorganizes the current density profiles, we investigate the contributions from the different terms in the induction equation. The equation was derived in Section 3.2 by combining Faraday's law (equation 2.6) with the resistive Ohm's Law (equation 2.19). The induction equation (equation 3.10) is stated again for convenience:

$$\frac{\partial \mathbf{B}}{\partial t} = \nabla \times (\mathbf{v} \times \mathbf{B}) - \eta \nabla \times \mathbf{j} - \nabla \eta \times \mathbf{j} \tag{3.10}$$

This equation can help us understand why there is a bifurcation of the current sheet

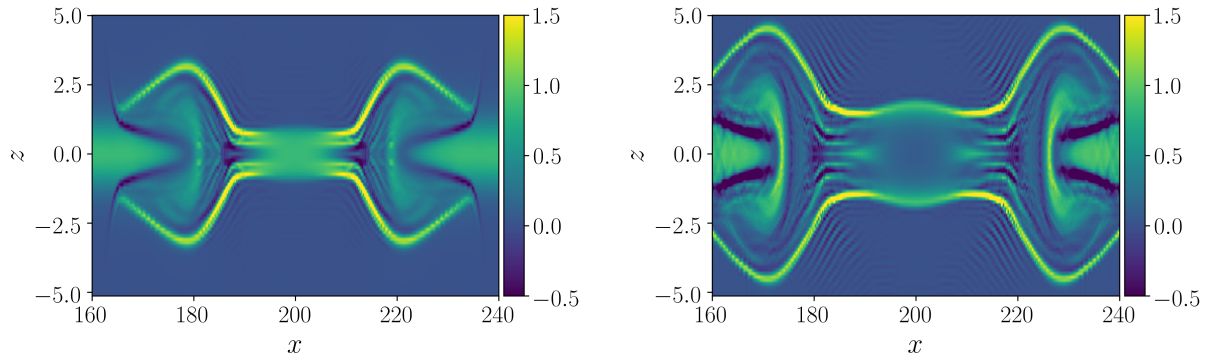

(a) $\eta_1 = 0.5$ (b) $\eta_1 = 8$

Figure 4.10: j_y and magnetic field lines at their peak reconnection rate for two different values of η_1.

for large magnitudes of the resistivity. The first term on the right-hand side represents advection of magnetic flux, while the two remaining terms correspond to its diffusion.

Figure 4.11 shows the contribution of each of the terms in equation 3.10 and the total variation of the magnetic field for two different values of η_1 at the times of peak reconnection rate. During these times, the temporal change of B_x (black line) is small and negligible. This is expected, as the system has already established the magnetic field and associated current structure, neither of which move or change significantly in magnitude. The green line shows the contribution from advection of magnetic flux. This term has a positive contribution for $z > 0$ for both cases, which means that it tries to increase B_x by transporting fresh field lines into the region. The blue and orange lines show the

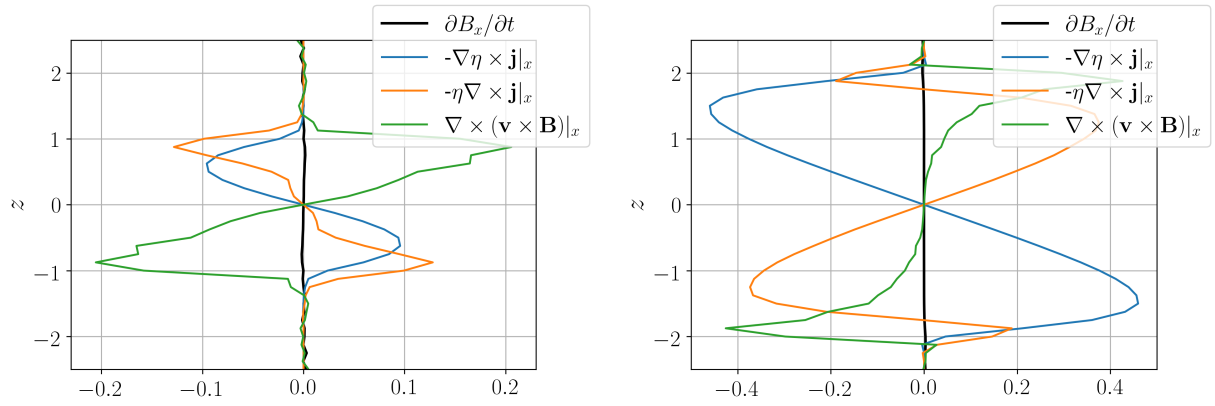

(a) $\eta_1 = 0.5$ (b) $\eta_1 = 8$

Figure 4.11: Contribution of the terms of the induction equation (eq 3.10) for two different magnitude values of η at their peak reconnection rate.

contribution from diffusion of magnetic flux. The diffusion in B_x enables the creation of new magnetic connections, and will result in an increase in B_z in the outflow region. Since the sum of the different terms $(\partial B/\partial t)$ is approximately zero, it means that the advected flux into the region is diffused at an equal rate. If we look at the two diffusive terms individually, there are clear differences between the low and high resistivity case.

For $\eta_1 = 0.5$ (panel 4.11a), both diffusive terms try to reduce B_x, as expected. This results in a constant decrease in the advection term for $1 > z > 0$. The resulting current profile, shown in Figure 4.9a, is therefore a result of advection of B_x into the current sheet, together with a finite diffusion across the current sheet. For $\eta_1 = 8$ (panel 4.11b), both diffusive terms attempt to reduce the magnetic field strength around $z = 2$, but just below this value, the term $-\eta\nabla \times \mathbf{j}$ turns positive, trying to increase B_x. This behaviour matches with the bifurcation of the current density, which experiences a considerable reduction after the peak around $z = 1.8$ (see panel 4.9d). For this case, panel 4.11b shows an important reduction in the advective term around $z = \pm 1.8$. The resistivity is in this case so large that it diffuses the magnetic field over a very short spatial scale, and so quickly that the advective contribution decreases rapidly. However, since the current density decreases rapidly after its peak at $z = 1.8$, the diffusive term $-\eta\nabla \times \mathbf{j}$ has a positive contribution to the magnetic field (for $z > 0$). This term ensures that a gradient of the magnetic field exists at the center of the current sheet, which is needed to maintain the reconnection rate. For even larger values of η_1, the spatial extent of the bifurcated current density peaks would be even shorter (in the z-direction), while the current in the center, required to maintain the maximum rate of 0.2 would consequently be even smaller.

Figure 4.12 shows the profile of B_x as a function of z for $\eta_1 = 0.5$ and $\eta_1 = 8$. To illustrate the restructuring and the origin of the bifurcated current density, we have added schematic arrows as magnetic field lines to illustrate this mechanism. In the left figure,

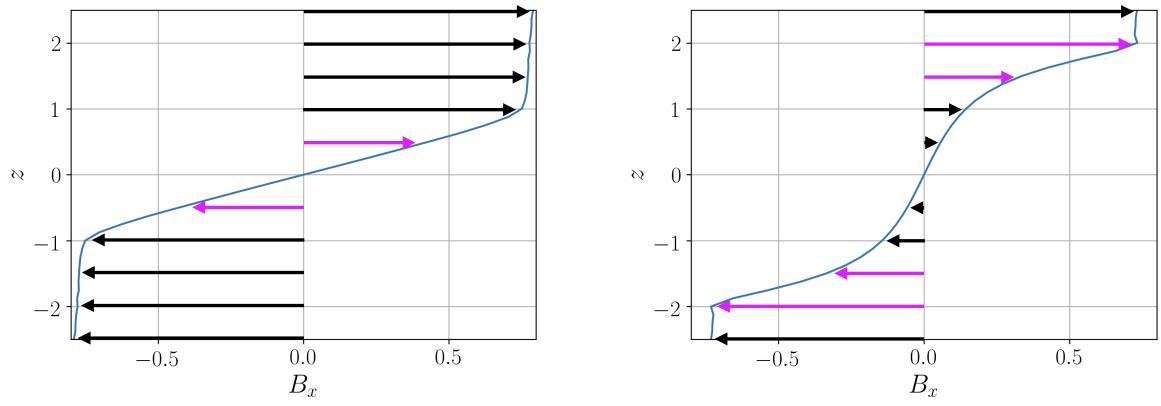

(a) $\eta_1 = 0.5$ (b) $\eta_1 = 8$

Figure 4.12: B_x as a function of z and schematic representation of the magnetic field lines for two different values of η_1

the largest gradient is around $z = 0$, which corresponds to the peak of j_y in Figure 4.9a. In the right figure, which corresponds to $\eta_1 = 8$, the largest gradient in B_x is not around $z = 0$. In this case, the magnetic field around the neutral line has been strongly diffused, and the largest gradients occur at around ± 1.8. These are indicated in panel 4.12b with magenta arrows. At these locations will then be where the curl of $\mathbf{B}$ is strongest and, as a consequence, where we will have the peaks in $\mathbf{j}$.

To summarize, increasing the magnitude of the resistivity in our system results in an increased reconnection rate, but only up to a point. At around 0.2, the reconnection rate saturates, even if we keep increasing the magnitude of η. The rate is limited by the bifurcation of the current sheet density, resulting in a smaller current density at the center. Intuitively, what happens is that the gradient of the magnetic field is pushed towards the boundary of the resistive region. The amount of current required is dictated by the asymptotic change in B_x between the two inflow regions, but the system has the freedom to change the distribution of the magnetic field gradient, and therefore also the current density profile.

It remains uncertain why the system wants to prevent the reconnection rate from increasing above 0.2. This limitation is likely due to macroscopic conditions such as the inflow or outflow velocity. Whenever one of them cannot keep up with the other one, the reconnection rate will slow down so that they are balanced, and the magnetic field lines don't pile up. It is known that the opening angle of the separatrix has a great impact in the forces driving the inflow and outflow. This will be discussed in more detail in the next section.

4.3 Impact of the shape of the resistive spot

In this section, we want to find out if changing the shape of the resistive spot can make the reconnection rate go even faster. To accomplish this, we are running the code with the highest value of η_1 analyzed in the last section ($\eta_1 = 8$), while changing the value of L_x introduced in equation 3.1. This will be the same as changing the aspect ratio of the diffusion region.

We take values of L_x in the range from 0.5 to 40, while L_z is kept constant at 1. The rest of the values which define η remain unchanged from the ones specified in table 3.1.

Figure 4.13 shows the colormaps for two different values of L_x. For low values of L_x, which means small aspect ratio, the resistive region takes a circular-like shape (Figure 4.13a). As we increase L_x, it becomes more elliptical. Eventually, for very large values of L_x, the resistive spot will be long and thin, and we will expect our reconnection rate to be similar to the one obtained by a Sweet Parker approximation (see Section 2.6).

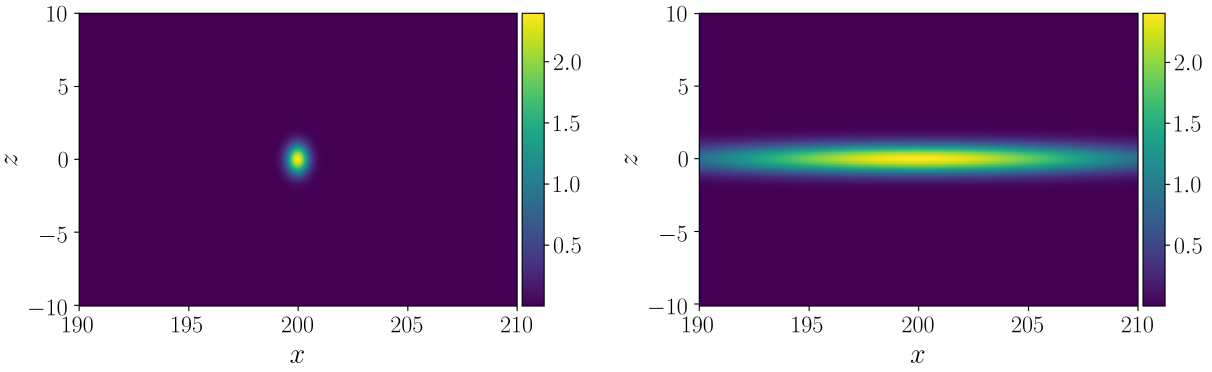

(a) $L_x = 0.5$ (b) $L_x = 10$

Figure 4.13: Shape of the resistivity or diffusion region for two different values of L_x

4.3.1 Reconnection rate vs aspect ratio

Figure 4.14 shows the reconnected flux as a function of time for the different values of L_x that we have considered. We notice a clear trend in the amount of reconnected flux depending on the aspect ratio; large values of L_x, which correspond to an elongated resistive region, reconnect significantly less magnetic flux compared to smaller values of L_x. However, this trend does not hold for $L_x \lesssim 2$, where the amount of reconnected magnetic flux decreases again. The highest amount of reconnected flux is reached for an aspect ratio of 2 ($L_x = 2$).

We also note that, in the beginning of the simulation (time 0 to 15), the flux seems to reconnect faster for elongated resistive regions, which would indicate that a larger aspect ratio makes it easier to start reconnection. Although this difference is not very significant from $L_x = 40$ to $L_x = 2$, it is made very evident for the 2 smallest aspect ratios ($L_x = 1$ and $L_x = 0.5$), where the reconnected flux is less than for the other values during the early timesteps.

In Figure 4.15, we plot the time derivative of the reconnected flux as a function of time, which is equivalent to the reconnection rate. Here, we observe that the peak reconnection rate is reached for an aspect ratio of 2, and its peak value is around 0.25. This is even higher than what we obtained in the previous section, where the aspect ratio was 5.

As expected, the lowest reconnection rate is reached for the largest values of L_x, as the shape of our resistive spot becomes a very long and thin resistive layer. This resembles the original Sweet-Parker description, where the length of the diffusion region is comparable to the system scale. The rate becomes very small since there is no significant tension ($\mathbf{j}\times\mathbf{B}$) on the reconnected field line to transport the flux away. Reconnection for such configurations is no longer explosive in nature, and can be considered as magnetic annihilation.

Figure 4.16 shows the time derivative of the reconnected flux ($\frac{d\phi}{dt}$) as blue dots and

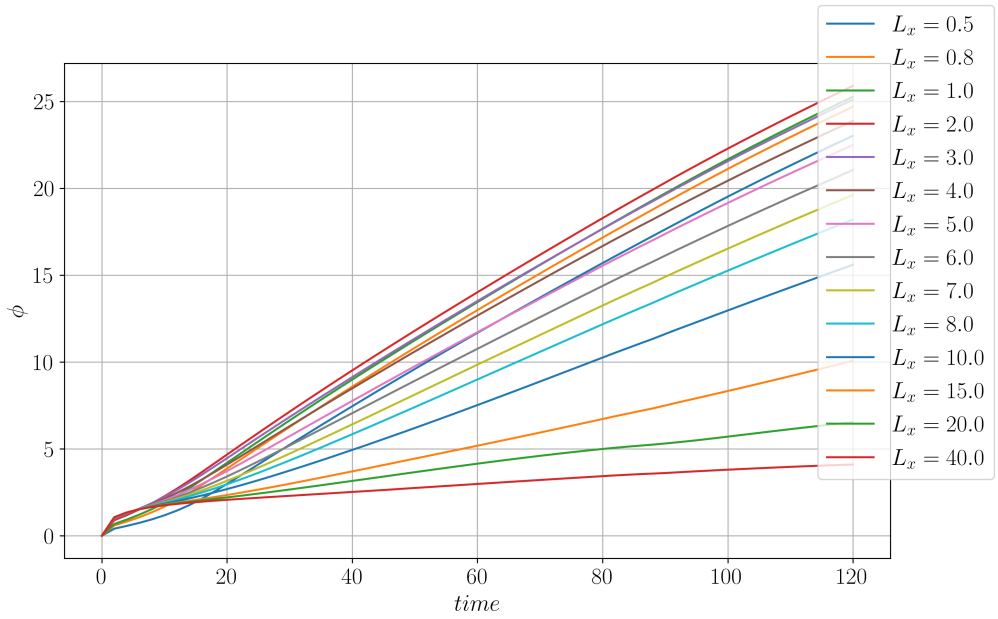

Figure 4.14: Reconnected flux, as a function of time, for different aspect ratios of the diffusion region.

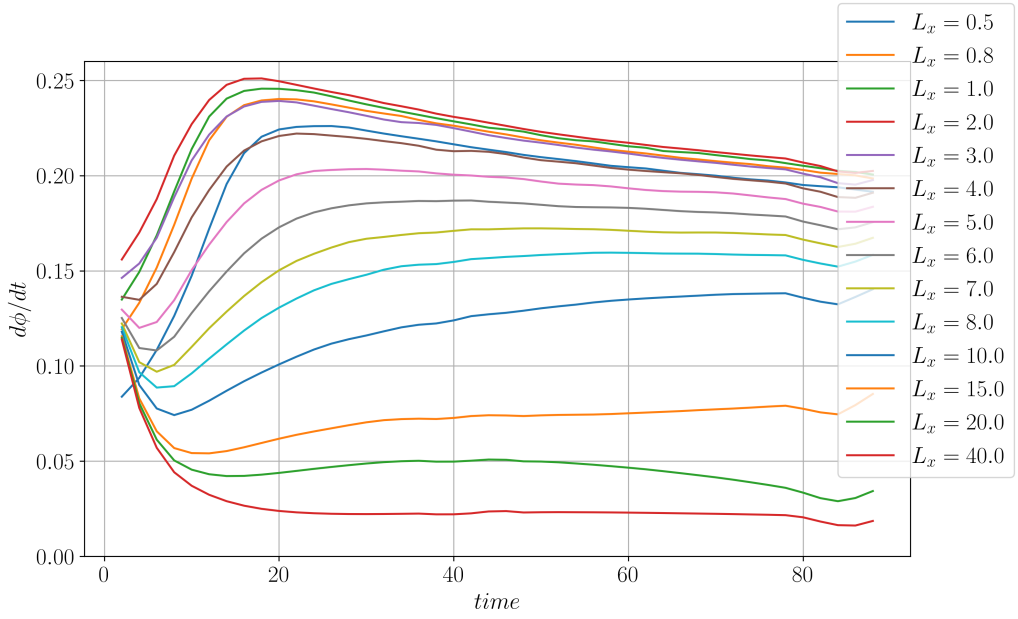

Figure 4.15: Reconnection rate, as a function of time, for different aspect ratios of the diffusion region.

the reconnected electric field (ηj_y) as red dots, both as a function of L_x. This allows us to check that these two ways of calculating the reconnection rate give us similar enough values so that we can use them interchangeably.

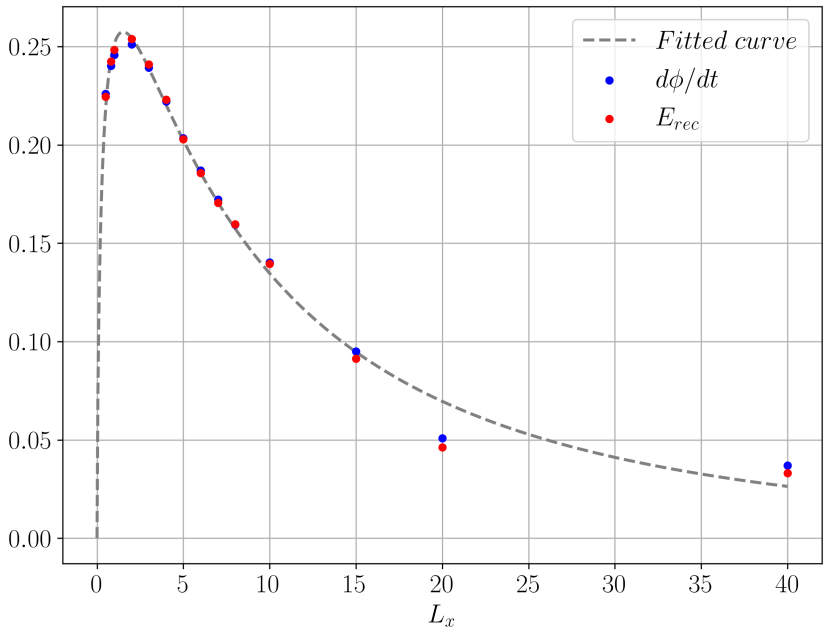

Figure 4.16: Peak reconnection rate, as a function of η_1, as blue dots, peak reconnected electric field, as a function of η_1, as red dots and fitted function as the grey dashed line.

In this plot, we can also see how the reconnection rate increases with the aspect ratio for values smaller than 2, and then decreases again. The grey dashed line shows a fit to the data using a functional form:

$$f(L_x) = aL_x e^{-\left(\frac{L_x}{b}\right)^c} \tag{4.4}$$

where $a = 4.838$, $b = 0.026$ and $c = 0.299$. The functional form is chosen, and thus does not have a direct physical interpretation. However, in the limits $L_x \to 0$ and $L_x \to \infty$ the function goes to 0, which coincides with our data. We can also speculate on the physical significance of the obtained values. Since the reconnection rate has units of V/m, the value of a must have dimensions of Volts. The value of b must have units of length. The parameter c determines how quickly the function converges.

In the next subsections, we will investigate why the reconnection rate has a maximum for an aspect ratio of 2.

4.3.2 Study of the diffusion region for different shapes of the resistive spot

In the previous subsection, we showed that the reconnection rate peaks for an aspect ratio equal to 2. To determine why the reconnection rate peaks at this specific aspect ratio, we investigate current density profiles and the separatrix opening angles for various aspect ratios.

In Figure 4.17, we show the current density (j_y) and the reconnection rate (ηj_y) for three different values of L_x. Both quantities are plotted as function of x in panel 4.17a and as function of z in panel 4.17b. For the values of L_x we have chosen $L_x = 2$, a greater value ($L_x = 5$) and a lower value ($L_x = 0.5$).

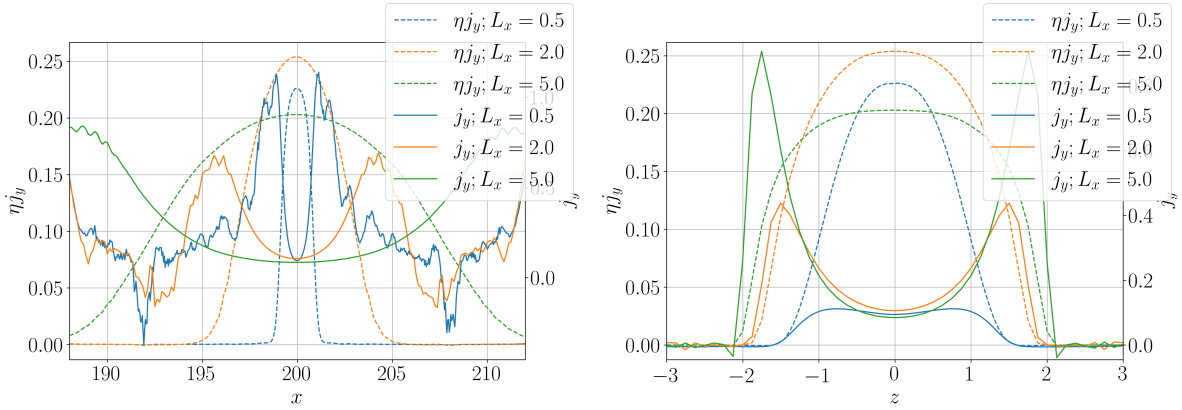

(a) $z = 0$ (b) $x = 200$

Figure 4.17: j_y as solid lines and ηj_y as dashed lines, as a function of x and z for $L_x = [0.5, 2, 5]$ ($L_z = 1$) at the time when the reconnection rate is higher for each of them

Both panels show that the reconnection rate (dashed lines at the center value) for $L_x = 2$ is higher compared to the other two values. Since the resistivity is equal for the three cases, the difference in the rate must correspond to a higher j_y at the X point. This is evident looking at the orange solid line at the center of both panels.

We also note that in panel 4.17a, the distribution of the current density is significantly different for the three choices of L_x. This directly reflects the influence of the resistive shape on the gradients of the magnetic field. Along the x direction, peaks of different magnitude can be observed for the 3 values of L_x. The highest current density is seen adjacent to the X point for $L_x = 0.5$, while the orange line ($L_x = 2$) profile is slightly wider and has a lower peak magnitude. For $L_x = 5$, the current density is distributed over a larger area. Hence, the distance between the peaks adjusts to the width of the resistive region for each of the cases.

In panel 4.17b, we can see a clear bifurcation of the current density for $L_x = 2$ and $L_x = 5$. The location of the peaks for $L_x = 5$ is located further from the center compared

to $L_x = 2$ which suggests that the length of the diffusion region has an impact on the current profile in the z-direction at $x = 200$. This is even more evident for $L_x = 0.5$ which is even narrower in the z-direction and does not have any bifurcation signatures. Note that $L_z = 1$ for all three cases. Since the current density depends on gradients along both directions, this suggests that the shape of the diffusion region leads to a reconfiguration of the magnetic field profile such that j_y is reduced at the center for smaller values of L_x. Next, we will analyze the behavior of the magnetic field to explain the reason for this.

Figure 4.18 shows the contribution of the different terms of the induction equation (eq. 3.10) for the 3 values of L_x represented in Figure 4.17, at times of peak reconnection rate. The left column shows the terms inducing a B_z component in a cut along the x-direction, while the right column shows the contributing terms to B_x along the z-direction. As we can see in Figure 4.18, the temporal change of B_x is negligible, since, at these times, the system has already established the magnetic field's structure and, consequently, neither the magnetic field nor the current density change significantly.

The green line represents the advection of magnetic flux. For the three cases, this contribution is positive for $z > 0$ (panels on the right-hand side), which means that it tries to increase B_x as field lines are transported towards the reconnection region. For $x > 200$ (panels on the left-hand side), the advective term contribution is negative, which means that it would decrease B_z, since B_z is positive here. For $x < 200$ the direction of B_z in newly reconnected field lines is opposite, and the positive contribution would also act to reduce B_z. Intuitively, one can imagine that if we shut off the resistivity, the ideal components would advect the newly reconnected field lines away with no possibility of generating new reconnected field lines. In such a hypothetical scenario the inflow region would start piling up magnetic flux, which would eventually mitigate the inflow velocity, and finally, the system would evolve into a thicker stable current sheet. In the panels on the left-hand side, we see that the contribution from the advective terms gets smaller as we increase L_x. The strength of B_z decreases for larger L_x. This was discussed in Section 2.6, and can also be explained by Gauss law: The divergence of the magnetic field is zero: $\nabla \cdot B = 0 \rightarrow B_z \sim \frac{B_x L_z}{L_x}$.

The blue and orange lines represent the contribution of the diffusive terms. Since $\partial B/\partial t = 0$, the sum of all the terms in the induction equation must balance. In all the panels in Figure 4.18, it is possible to see how the term $-\nabla\eta \times \mathbf{j}$ has a larger contribution compared to the term $-\eta\nabla \times \mathbf{j}$. The reason for this is that we are using a resistivity with a large magnitude ($\eta_1 = 8$), so the impact of the gradient of the resistivity must be large. This term, represented with the blue line, is negative (for $z > 0$) in the panels on the right-hand side, meaning that, in the inflow region, it tries to diffuse the magnetic field away from the reconnection region. The orange line, representing the term $-\eta\nabla \times \mathbf{j}$, has a negative contribution at first, but turns positive just after. This characteristic behavior was discussed in Section 4.2.2 (Figure 4.11). In the x-direction, panel 4.18a shows how the blue line has a positive contribution for $x > 200$, peaking at around $x = 200.5$, while the orange line has a negative contribution. This means that the gradient of η in the x direction tries

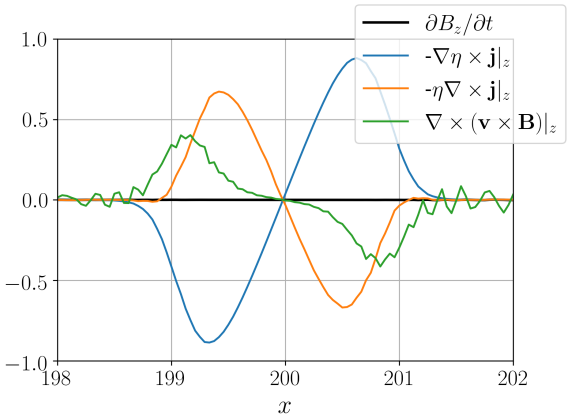

(a) $z = 0$, $L_x = 0.5$

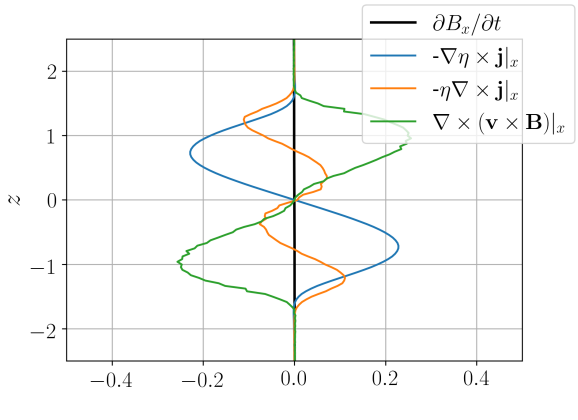

(b) $x = 200$, $L_x = 0.5$

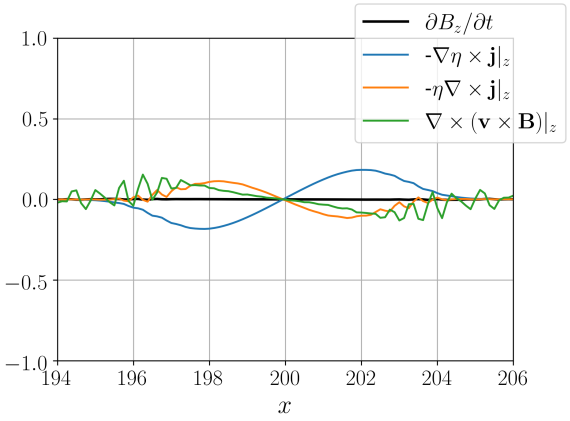

(c) $z = 0$, $L_x = 2$

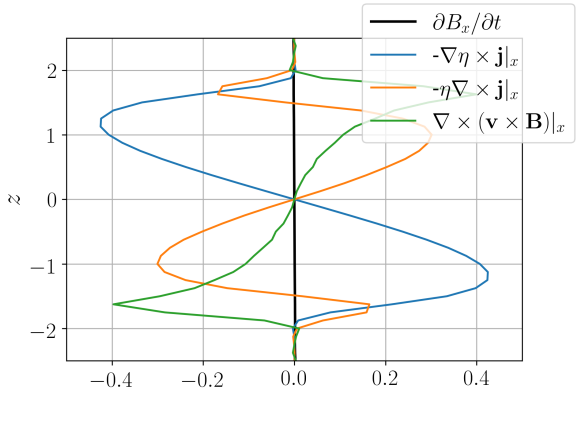

(d) $x = 200$, $L_x = 2$

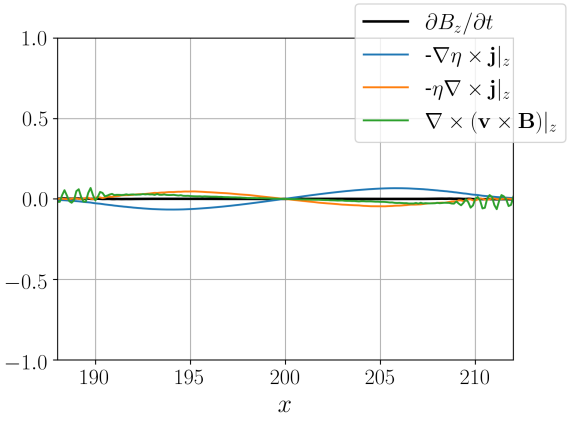

(e) $z = 0$, $L_x = 5$

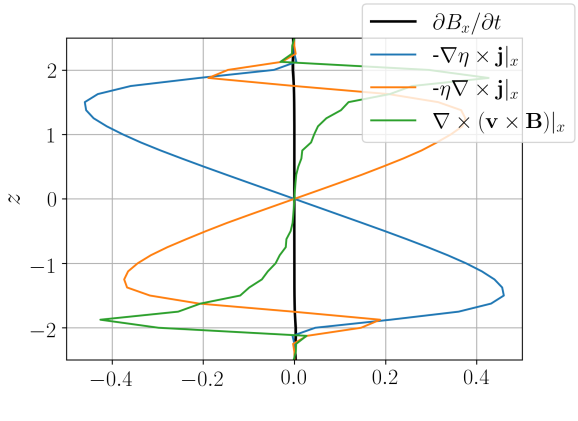

(f) $x = 200$, $L_x = 5$

Figure 4.18: Contribution of the different terms of the induction equation, as a function of x (panels on the left side) and z (panels on the right side), for 3 different values of L_x.

to increase B_z at the edges of the diffusion region, while the curl of j_y tries to oppose this behaviour. The short extent in the x-direction of the resistive spot, corresponds to a very strong η gradient and, consequently, a large B_z close to the X line, unlike the cases where $L_x > 2$. The profile and shape of these two diffusive terms depend on the current density profile. As we observed in Figure 4.17, changing L_x not only changes the current profile in the x-direction, but also has a significant contribution to the profile in the z-direction.

To understand how changing L_x influences the current profile and magnitude, Figure 4.19 shows the magnitude of B_x as a function of z and B_z as a function of x for our 3 values of L_x. For $L_x = 5$, which corresponds to an elongated resistivity, the gradient of B_x has a steeper slope (resulting in a lower current density) in the central region, which results in a smaller gradient of B_z in the outflow (Figure 4.19b). For $L_x = 2$, the gradient of both B_x and B_z get larger, and even stronger for $L_x = 0.5$. Notice that for $L_x = 0.5$, there is a large enhancement of B_z close to the X point, as we described above.

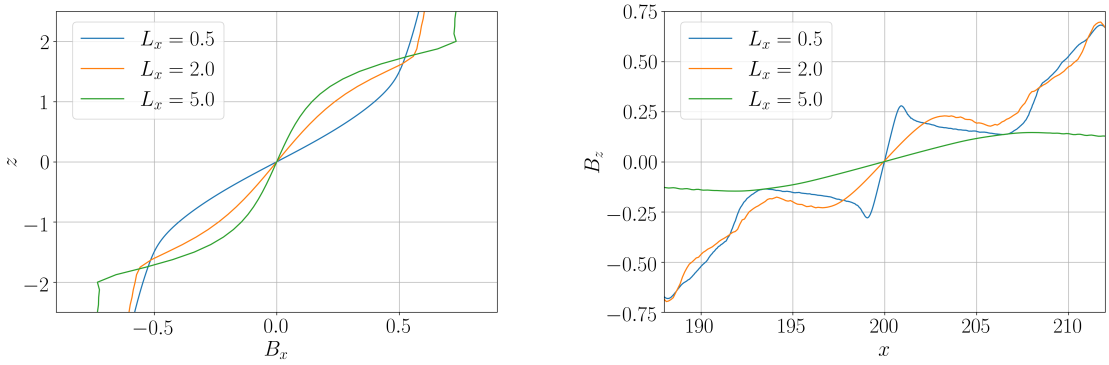

(a) $x = 200$ (b) $z = 0$

Figure 4.19: B_x and B_z for the 3 different values of L_x studied at their times of peak rate.

For all values of L_x, the term $-\nabla\eta \times j_y$ is responsible for the majority of the local changes of B. Thus, the shape of the resistive region has a significant influence on the distribution of the magnetic field, and in turn, the current density. For $L_x > 2$, B_x has a smaller gradient in the center region, resulting in a lower current density, while for $L_x < 2$, B_z is important, also resulting in a lower current density. In order to understand how this restructuring of the magnetic field affects the magnitude of the current density, we look in detail at the profiles of the magnetic field components that result in the y-directed current density. Figure 4.20 shows the contribution of $\frac{\partial B_x}{\partial z}$ and $-\frac{\partial B_z}{\partial x}$ to the current density for the cases $L_x = 0.5$, $L_x = 2$ and $L_x = 5$ as a function of x (panels on the left side) and z (panels on the right side). From these plots, it is clear that the reduction in j_y in the center for the case $L_x = 0.5$ is due to a large increase in the gradient of B_z close to the reconnection point (panels 4.20a and 4.20b). For $L_x = 5$, the contribution of $\partial B_z/\partial x$ is very small, but

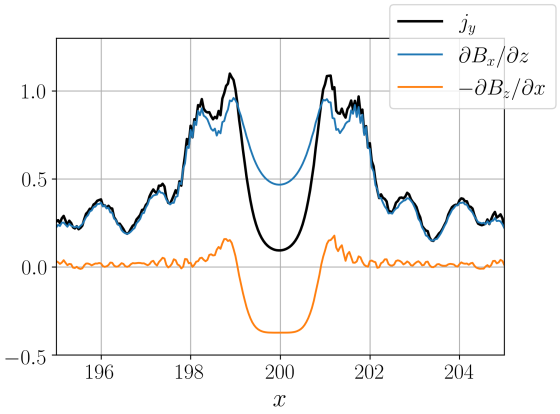

(a) $z = 0$, $L_x = 0.5$

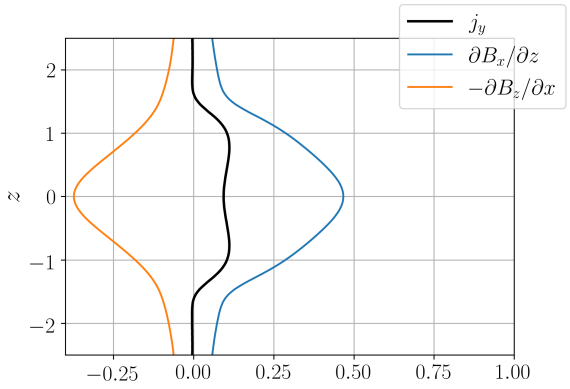

(b) $x = 200$, $L_x = 0.5$

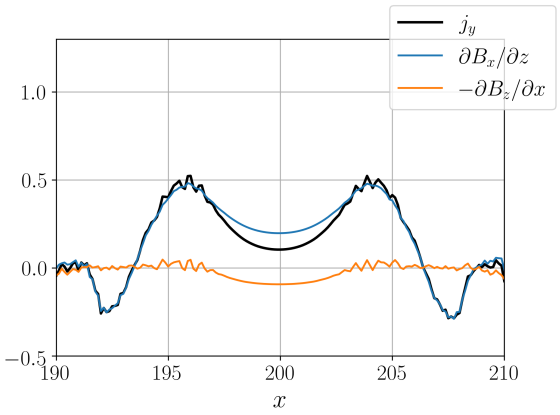

(c) $z = 0$, $L_x = 2$

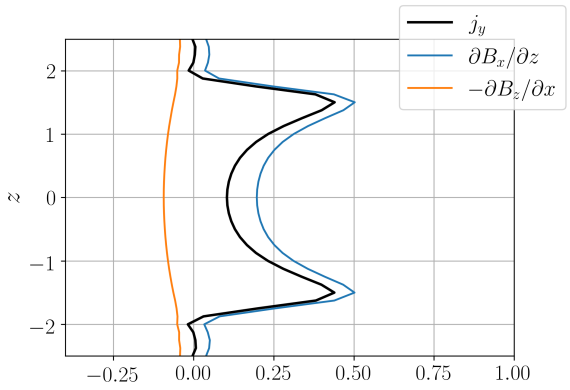

(d) $x = 200$, $L_x = 2$

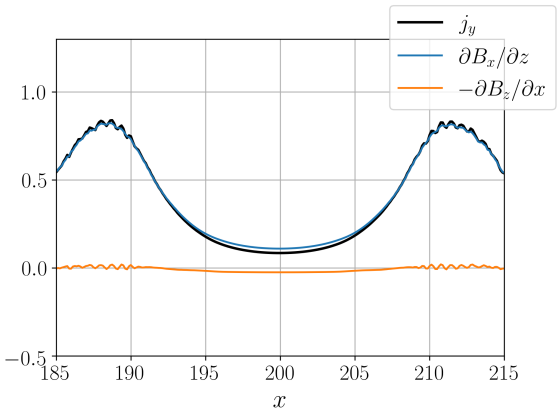

(e) $z = 0$, $L_x = 5$

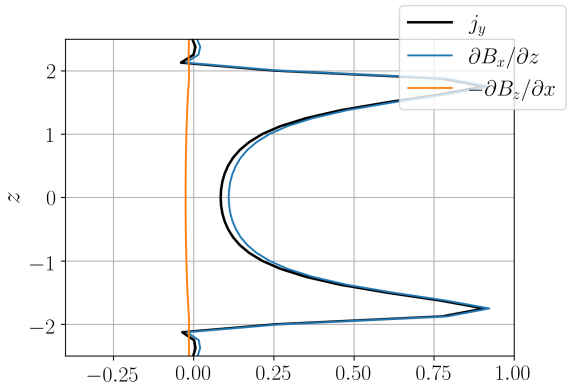

(f) $x = 200$, $L_x = 5$

Figure 4.20: Contribution of the terms $\frac{\partial B_x}{\partial z}$ and $-\frac{\partial B_z}{\partial x}$ to the total current density j_y, as a function of x and z, for 3 different values of L_x. Very small aspect ratios correspond to a reduction of j_y in the center.

the contribution of $\partial B_x/\partial z$ is also very small (see panels 4.20f and 4.20e), resulting in a lower current density than for $L_x = 2$. Thus, the case $L_x = 2$, reaches the right balance between the two terms to have the highest current density in the central region, resulting in a faster reconnection rate.

To summarize, we've seen that the bifurcation of the current sheet occurs when the magnitude of the resistivity is so large that the gradient of B_x is pushed towards the boundary of the resistive region. The magnitude of the resistivity is $\eta_1 = 8$ for all three cases, but for the case $L_x = 0.5$ the bifurcation is reduced, as shown in Figure 4.17b. The reason for this is that for most cases, which have larger L_x, B_z is very small near the diffusion region, making B_x the main contributor to j_y. However, for $L_x = 0.5$, the incoming magnetic flux, which is primarily in the x-direction above and below the x-line, must be converted into B_z within our diffusion region. In terms of the induction equation, the $j_y \partial\eta/\partial x$ is the dominating term (see panel 4.18b). This is because the region is so small that a strong η gradient exists throughout the diffusion region. This produces a strong increase in B_z close to the x-line, that reduces the total amount of current density, slowing down reconnection in its turn. This explains the reduction in j_y observed in panel 4.17b. Since $j_y = \nabla \times \mathbf{B}|_y = \frac{\partial B_x}{\partial z} - \frac{\partial B_z}{\partial x}$, the second term on the right-hand side will effectively reduce j_y.

Impact of the aspect ratio on the opening angle

The increase in B_z for very small values of L_x is tied to a deformation of the magnetic field lines as they move towards the diffusion region. Figure 4.21 shows schematically how would the magnetic field lines look like for a large aspect ratio (panel 4.21a) and for a small aspect ratio (panel 4.21b).

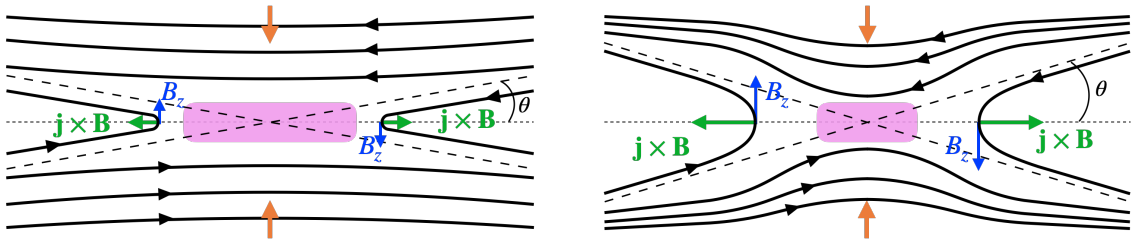

Figure 4.21: (a) Sketch of the magnetic field lines for a large aspect ratio. (b) Sketch of the magnetic field lines for a small aspect ratio. The inflow field lines for a small aspect ratio bend more while approaching the diffusion region. This results in a larger opening angle of the separatrix.

For a large aspect ratio, the magnetic field lines approach the diffusion region with mainly a B_x component, which, as illustrated in Figure 4.20a, results in a thin and elongated current sheet. The outflow is driven by the tension force ($\mathbf{j} \times \mathbf{B}$), which can be

approximated as $j_y B_z$ in this region. For a thin, elongated current sheet, B_z is small, the outflow is limited, and the reconnection rate will be adjusted self-consistently.

For a small aspect ratio, the magnetic field lines in the inflow bend more. The B_z component in the outflow is larger (as illustrated in Figure 4.20b) and the tension force increases, increasing the outflow speed and the reconnection rate. However, if the aspect ratio keeps getting smaller, $L_x < 2$, j_y decreases too much and the tension starts getting smaller again, as discussed above.

The Sweet-Parker scaling, discussed in Section 2.6, considers the effective inflow to be equal to the ambient conditions. This approximation does not take into account the deformation of the magnetic field as it expands towards the diffusion region. This expansion will influence the effective tension of newly reconnected field lines.

Liu et al. [2017] studied why magnetic reconnection usually has a maximum rate of the order of 0.1 across different systems. The author suggested that the maximum local rate, for a low-β plasma, where β is defined as ratio of magnetic pressure to the plasma pressure, is determined by an optimal opening angle of the separatrix. The angle corresponding to the peak rate was found to be 17.22°, corresponding to a reconnection rate of 0.2. We can think of the opening angle as the one made by the separatrix with the x axis.

The existence of an optimal angle can be understood as follows. For small opening angles ($\theta \approx 0°$), the diffusion region will be long and thin, which will bring us back to a case similar to the Sweet-Parker approximation where due to very elongated reconnected field lines the z component of the magnetic field is very small, as it is shown in Figure 4.21a. The $\mathbf{j} \times \mathbf{B}$ force driving the outflow can be written as:

$$\mathbf{j} \times \mathbf{B}|_{outflow} = B_z \left[\frac{\partial B_x}{\partial z} - \frac{\partial B_z}{\partial x} \right], \tag{4.5}$$

where the first term in the right side represents the magnetic tension and, the second term, the magnetic pressure. If B_z is very small, the ouflow speed will be limited due to a small $\mathbf{j} \times \mathbf{B}$ force. Thus, the reconnection rate will be slow. For $\theta \approx 45°$, the current density is zero ($j_y = \partial B_z/\partial x - \partial B_x/\partial z = 0$), by symmetry. This means that the tension force balances the magnetic pressure force since $\frac{\partial B_x}{\partial z} = \frac{\partial B_z}{\partial x}$, and equally in the inflow direction - effectively stopping reconnection. Consequently, there has to exist an intermediate angle which corresponds to the fastest reconnection rate, optimizing the system.

Since large aspect ratios in the diffusion region are associated with small opening angles, and small aspect ratios are related to larger opening angles, we expect that our runs with different aspect ratios should consistently have different opening angles.

To demonstrate this, we have plotted the magnetic field lines for 4 different values of the aspect ratio including the case for $L_x = 2$, which corresponds to the maximum reconnection rate. The result is shown in Figure 4.22. The dashed lines represent the contour of η at a value 0.1, which illustrates the profile of the diffusion region. These are plotted in the

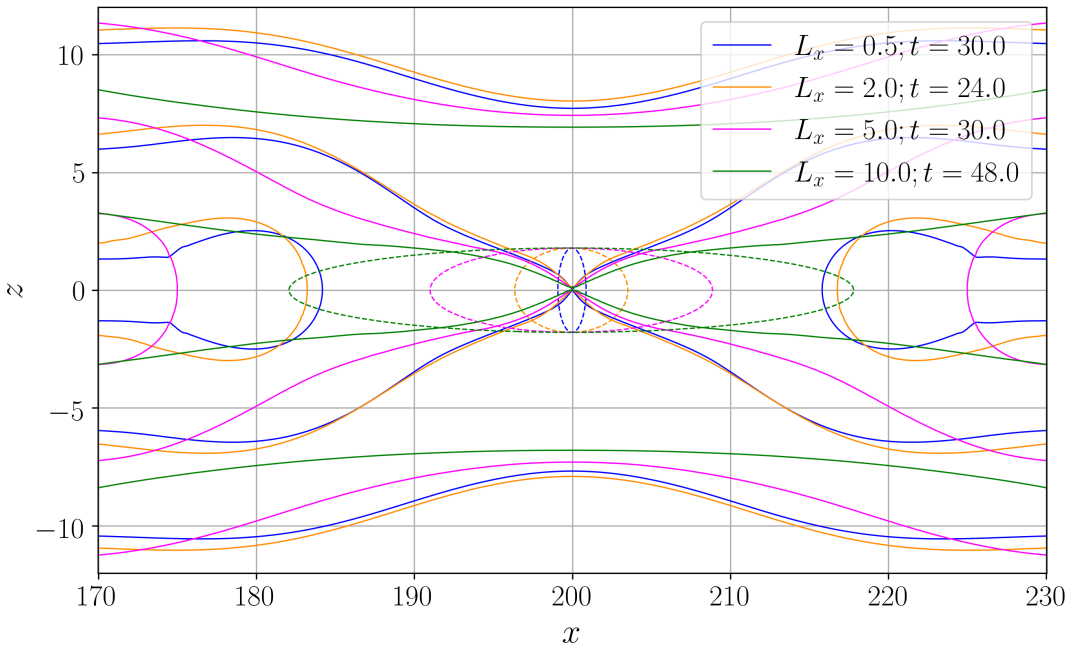

Figure 4.22: Magnetic field lines around the diffusion region as solid lines, and contour of η at a value 0.1 as dashed lines for 4 different values of L_x at their peak rate time. Changing the aspect ratio has an influence on the geometry of the reconnected field lines, which in turn determines how efficient the $\mathbf{j} \times \mathbf{B}$ force can transport flux away.

same color as the corresponding field lines (solid lines).

Looking into the inflow region, we note that for $L_x = 10$, the magnetic field line that is approaching the reconnection region has almost no B_z component, consistent with its resistivity with a large aspect ratio. The field line corresponding to $L_x = 5$, shows some deformation as it expands towards the diffusion region. Finally, the field lines for $L_x = 0.5$ and $L_x = 2$ show a significant bending in the same region, as expected for smaller aspect ratios.

If we take a closer look into the magnetic field lines that are reconnecting, we notice that they cannot be considered straight lines such as the separatrices that have been illustrated (e.g. Figure 4.21). Far from the reconnection region, the reconnecting field lines bend due to the expanding outflow structure that can be observed in Figure 4.1. Also, from careful inspection they also deform as they penetrate the diffusion region, this is most clearly seen for $L_x = 0.5$.

For this reason, it is not straightforward to define the opening angle. We chose to quantify the opening angle between the edge of the diffusion region and the beginning of the outflow structure. That is, we choose a region far enough away from the reconnection

point to avoid the local deformation there, but not so far that it is affected by the outflow structures.

The opening angle corresponding to our highest rate is obtained for $L_x = 2$, and it corresponds to a value of $\sim 15°$. The reconnection rate obtained for this value is around 0.25. This is close to the analytically predicted value of 17°, suggested by *Liu et al.* [2017]. Regardless of a precise quantification, a clear trend is observed. As L_x increases from 10 to 2 the opening angle increases, which consistently means that the outflow driving force increases, and consequently the reconnection rate increases. However, for values between $L_x = 2$ to $L_x = 0.5$ the opening angle decreases, meaning that the rate decreases. This is consistent with the reduction of j_y as discussed above. The current density, the outflow force and velocity, the reconnection rate, and the opening angle are of course coupled and self-consistently constantly regulated between microscopic and macroscopic scales. Thus, we have here demonstrated that, to maximize the reconnection rate, the system must reconfigure itself, so that an optimum opening angle is achieved.

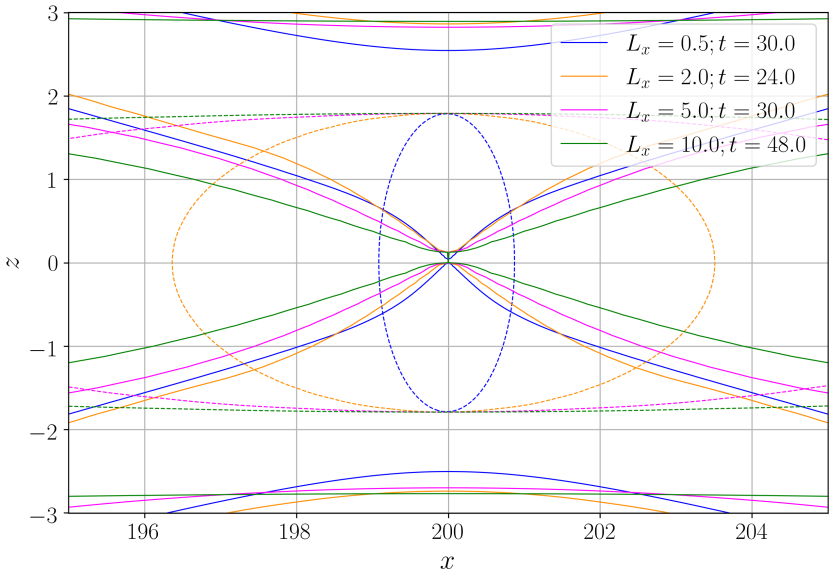

Figure 4.23: Magnetic field lines around the diffusion region as solid lines, and contour of η at a value 0.1 as dashed lines for 4 different values of L_x at their peak rate time. Inside the diffusion region, the opening angle for $L_x = 0.5$ is larger than for the other cases.

Even though we would have expected a larger opening angle for smaller values of L_x this does not fit the conclusion from above. In Figure 4.23, we take a closer look at the deformation of the field lines as they penetrate the diffusion region. Inside the diffusion region, the blue line ($L_x = 0.5$) exhibits a larger opening angle compared to the other cases. However, as we move outside the diffusion region the angle changes and becomes smaller.

This suggests that the opening angle is not determined by the local microscopic properties alone, but instead also includes contributions from the larger scales. Such a conclusion is also suggested by *Liu et al.* [2017], and this supports the hypothesis that the rate is also limited and to some degree controlled by macroscopic properties.

Chapter 5

Discussion

In this chapter, we are going to discuss some properties of MHD scaling, as well as the impact of the grid resolution and time resolution in our analysis. We want to verify that, as we should expect from the characteristics of MHD scaling, changing the size of the resistive spot in our system does not have any impact in the results, as long as the Lundquist number is kept equal and the ratio between the size of the resistive spot and the width of the current sheet is maintained. To do so, we will analyse two additional runs (see magenta dots in Figure 3.2). Moreover, we will verify that both the grid resolution and the time resolution that we use in our analysis are sufficient for the study.

5.1 Scaling relations

Ideal MHD has no inherent scale. That means that no equation explicitly quantifies the length scale of the system. Resistive MHD is, however, characterized by a specific scale. The added resistivity in Ohms law determines how quickly the field diffuses over a specific length scale ($\tau_d = L^2/\eta$). Thus, changing the size of our diffusive region will effectively alter the characteristic length scale of our problem.

To understand our code and analyze these scaling relations in MHD, we execute three new runs, in which we change the size of the resistive spot, but trying to keep all the ratios between quantities invariant. The aspect ratio for the three runs compared is kept at 1, and the values of L_x and L_z are changed accordingly. Figure 5.1 shows the profile of the resistive spots for the 3 different sizes that we are studying.

By changing the gradient scale length L_z, we are effectively also altering all relevant derived gradients in this direction. This includes the current, time and velocity ($t = L/v$), and the system size. Another scale introduced in the simulation, part of our initial

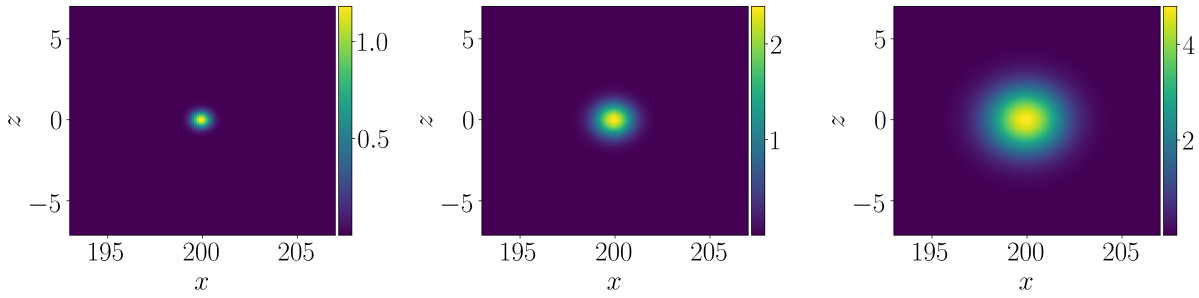

(a) $L_x = L_z = 0.5$ (b) $L_x = L_z = 1$ (c) $L_x = L_z = 2$

Figure 5.1: Shape of the resistivity or diffusion region for the 3 different runs

conditions, is the current sheet width. For all previous runs, the width is kept equal to L_z (=1). When we increase or decrease L_z, this width must be changed consistently. For example, for $L_z = 2$, the current sheet width must match. Otherwise, due to the scaling of the system the current sheet would appear as a current sheet with half the thickness compared to the $L_z = 1$ case. A current sheet with half the thickness would contain half the mass and, thus, be less inert. Similarly for $L_z = 0.5$, the current sheet would appear as twice the thickness and be much more inert compared to the previous runs.

An important quantity is the relation between the Alfvenic convection electric field and the diffusion electric field, defined by the lundquist number:

$$S = \frac{\lambda v_A}{\eta} \tag{2.23}$$

The lundquist number in itself does not have a dimension, which means that the right hand side of equation 2.23 is also dimensionless. In our case, λ is picked to be the significant dimensionless gradient scale length, which corresponds to L_z in our case. This means that by changing L_z, the value of η needs to be changed in accordance in order to maintain the relation. Additionally, changing the scale length of the resistivity also changes the ratio between the relevant gradient scale length, L_z, and the system size. This implies that even if the resistivity magnitude is changed in order to keep S the same, the effective system size can be twice as large for $L_z = 0.5$ as for $L_z = 1$. However, the system size is big enough so that we don't have to worry about the influence of the boundary conditions. Thus, even if we double L_z in size, and we double the width of the current sheet and the magnitude of the resistivity in accordance, there will still be enough space in x, so that the flux doesn't pile up, and enough space in z, so that we don't spend all the available flux.

Table 5.1 shows the quantities that have been changed in order to maintain the scaling relation.

where τ is the characteristic time, and τ_0 represents the specific time scale used for all previous runs.

	η_1	L_x	L_z	B_{x0}	ρ_0	j_{y0}	τ
Run 1	4	0.5	0.5	$\tanh(z/0.5)$	$1/\cosh^2(z/0.5) + \rho_{lobe}$	$1/\cosh^2(z/0.5)$	$0.5\tau_0$
Run 2	8	1	1	$\tanh(z)$	$1/\cosh^2(z) + \rho_{lobe}$	$1/\cosh^2(z)$	τ_0
Run 3	16	2	2	$\tanh(z/2)$	$1/\cosh^2(z/2) + \rho_{lobe}$	$1/\cosh^2(z/2)$	$2\tau_0$

Table 5.1

Figure 5.2 shows the reconnection rate, $d\phi/dt$, as a function of time, for the 3 different runs.

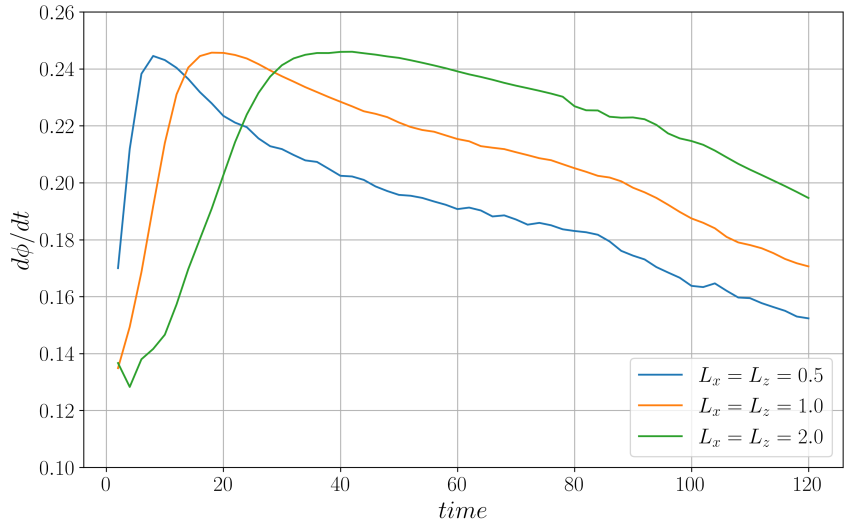

Figure 5.2: Reconnection rate, as a function of time, for the 3 different runs.

We can appreciate how the 3 runs reach a similar peak reconnection rate, but the case $L_x = 0.5$ reaches it at around $t = 10$, the case $L_x = 1$ at around $t = 20$ and the case $L_x = 2$ reaches the peak reconnection rate at around $t = 40$. The derived characteristic time scale is $\tau = L_z/v_A$, thus, changing the characteristic scale length consistently affects the derived characteristic timescale. This is the reason why there is a difference in the time the reconnection rate takes to reach its peak, and the relation between the times is a proof of that ($2t_{L_z=0.5} \approx t_{L_z=1} \approx 0.5t_{L_z=2}$).

We conclude then, that in MHD, we can reproduce the same analytical scenario if the rates between the quantities are maintained the same inside the domain. Thus, when studying the reconnection rate for three different sizes of the resistive spot, the result will be the same for any size, as long as we maintain the relations between all the needed quantities and the size of the domain is big enough.

5.2 Grid resolution impact

When investigating the impact that different shapes of the resistive spot have on the reconnection rate, we are required to make some runs with small values of L_x. It seems reasonable, then, to get concerned about the fact that the box resolution may not be enough to give a precise enough result for the reconnection rate.

To verify that the obtained result does not depend on the resolution, we executed two additional runs, with the same conditions but with different resolution of the simulation domain.

As mentioned, the box resolution that we want to use for our analysis is 3200×1600 cells. The two additional runs are made with two times and three times this grid size, see table 5.2. We choose the run with the smallest L_x for the comparison, as this run has the shortest characteristic gradient scale length and would be most susceptible to changes in the resolution. In table 5.2, we have written the values of the magnitude of the resistivity (η_1), the values of L_x and L_z which determine the shape of the resistivity, the size of the domain (x and z), and number of grid cells for the z axis (n_z) and x axis (n_x) for the three different runs.

	η_1	L_x	L_z	x	z	n_z	n_x
Run 1	8	0.5	1	[0,400]	[-100,100]	1600	3200
Run 2	8	0.5	1	[0,400]	[-100,100]	3200	6400
Run 3	8	0.5	1	[0,400]	[-100,100]	4800	9600

Table 5.2

In Figure 5.3, we have plotted the reconnection rate obtained with the 3 different grid resolutions.

Some variations between the runs can be appreciated for the initial timesteps in Figure 5.3, but otherwise the reconnection rate remains the same for the three different resolutions.

Higher resolution means that the simulation can resolve smaller structures. To demonstrate this, in Figure 5.4, we show the current density around the diffusion region tor the three different resolutions.

Comparing the current density for the different resolution reveals significant differences. The magnitude of the current density is very different between the runs. We can also observe different structures in similar regions, e.g. the cut at $z = 0$ has two zones of negative j_y in the Figure 5.4b at around 198 and 202, that do not exist in the other two figures.

These consequences of changing the resolution, though, appear to be unimportant for our study, as we showed with Figure 5.3. A higher resolution means that the code resolves

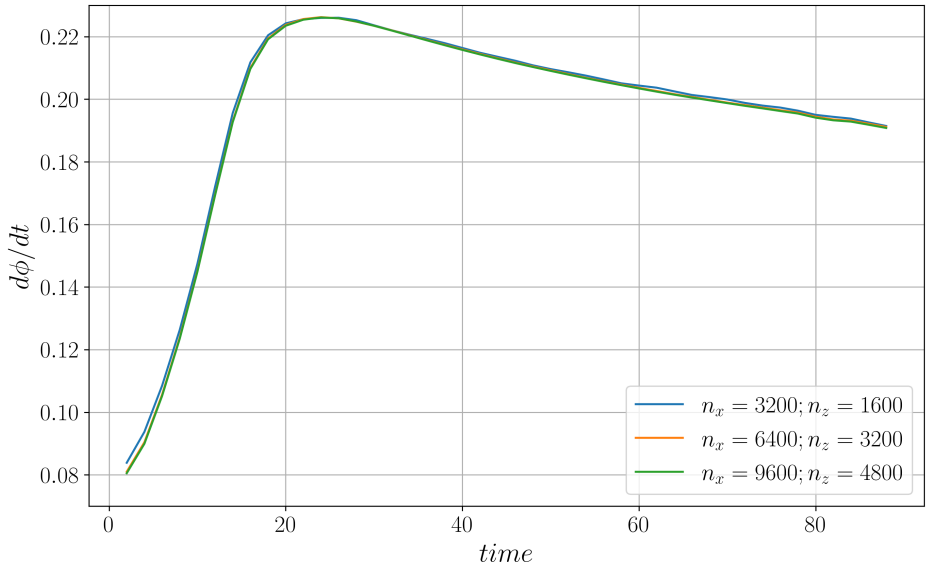

Figure 5.3: Reconnection rate, as a function of time, for the three cases specified in table 5.2

structures at smaller scales, as demonstrated in figures 5.4a and 5.4c, but these smaller structures do not influence the larger scale energy conversion or rate.

Based on the comparison, we conclude that our resolution is sufficient. Increasing the resolution has no significant impact on the rate, which means that the overall dynamics in the entire system behaves the same. This means that the solution has converged at a lower resolution. Higher resolution means higher computational cost, and for the problem at hand, this result suggests that our chosen resolution is more than adequate.

In our study, we used a resolution of 9600×4800 for the case where $L_x = 0.5$ and $L_z = 1$, since it can provide a better quality in figures like 4.22 or 4.17a and the computational cost was acceptable, but the rest of the runs have been made with the normal resolution of 3200×1600.

5.3 Time resolution impact

The code runs on the Alfvén timescale $t = L/v_A$, where the characteristic length, L, is the distance an Alfvén wave can travel in a time unit. The timestep used is a value chosen

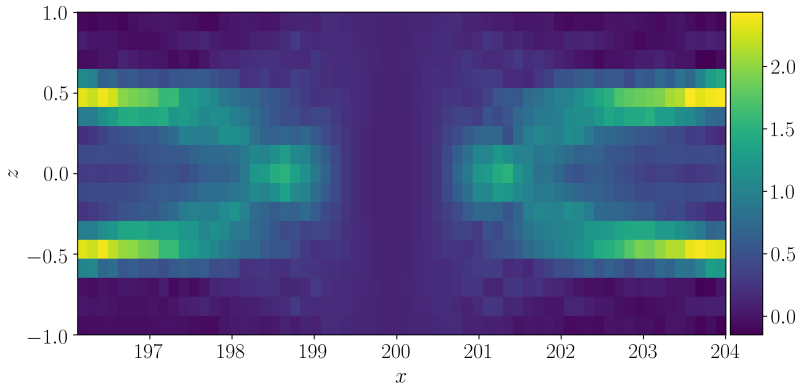

(a) Box resolution: 3200×1600

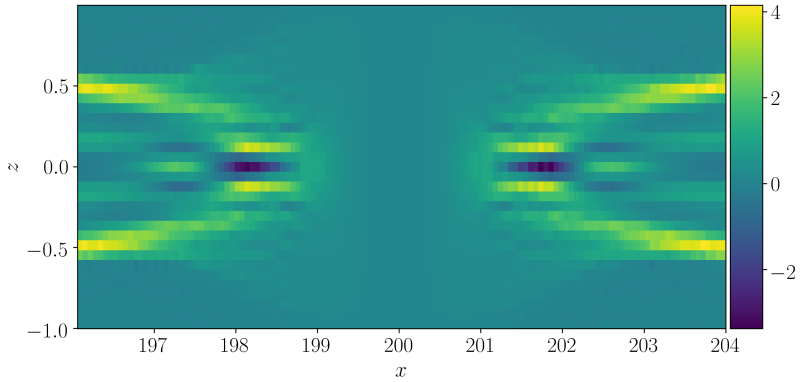

(b) Box resolution: 6400×3200

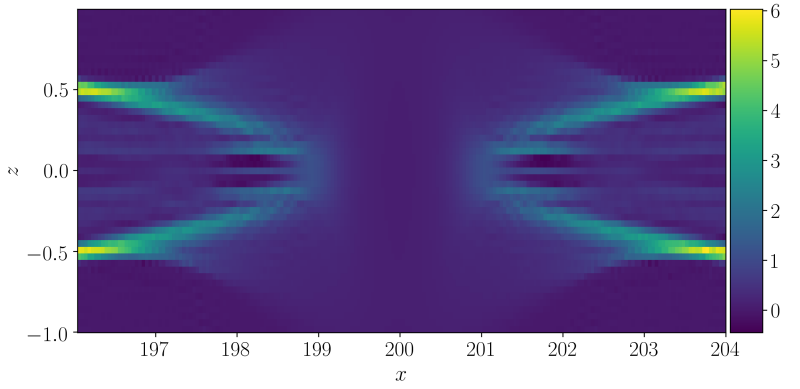

(c) Box resolution: 9600×4800

Figure 5.4: Pixelated view around the X point of the current density at $t = 26$ for $L_x = 0.5$ and $\eta_1 = 8$

to be significantly smaller than the time an Alfvén wave needs to travel across one grid cell. The time required to do so is $t = 0.125$, and the timestep chosen is 10 times smaller: $dt = 0.0125$.

In order to prove that the timestep chosen is small enough to not produce any irregularities in the data obtained, we have run the simulation for $\eta_1 = 1$, $L_x = 5$ and $L_z = 1$ with a timestep corresponding to $dt = 0.006$, less than half than the value used for our simulations. The reconnection rate obtained for both time resolutions is shown in Figure 5.5.

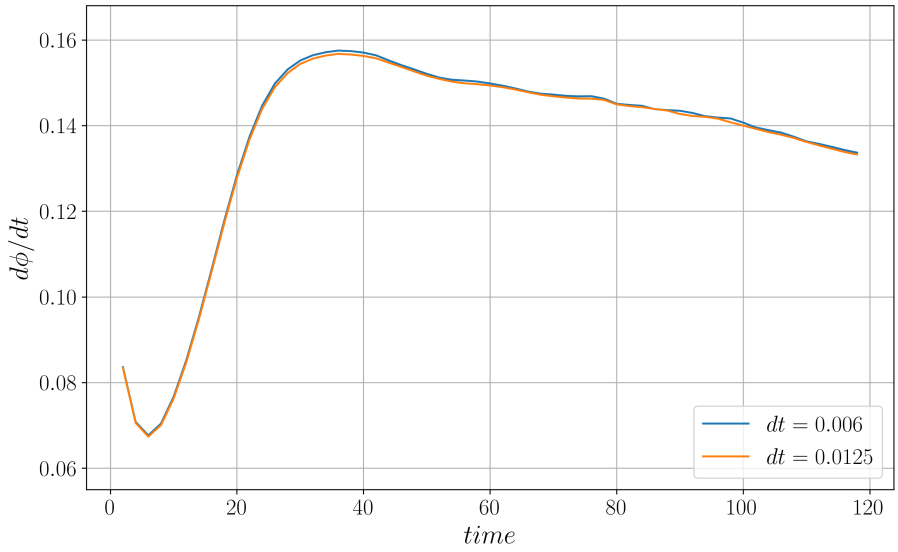

Figure 5.5: Reconnection rate, as a function of time, for the two different time resolutions

This figure shows almost no difference between both resolutions, which means that the time resolution used is small enough for our study.

Chapter 6

Summary and Key Findings

The goal of this thesis was to determine how fast magnetic reconnection can occur by varying the magnitude and shape of a localized resistivity. To do so, we first introduced some plasma environments, such as the solar wind and the magnetosphere, where magnetic reconnection can operate. We then introduced the concept of *plasma* and the necessary equations to describe its behaviour in space, as well as the magnetohydrodynamic (MHD) equations, in which the plasma is treated as a single fluid and the state of our system is described by macroscopic variables. In our case, we are using the resistive MHD equations, in which several assumptions have been made. The assumptions include considering that the plasma is composed of electrons and only one species of ion, and that the sum of both charges is approximately the same (quasineutrality). We are also considering timescales and lengthscales in which we can neglect most of the terms in Ohm's law (equation 2.18). This way, we can consider the resistive MHD equations near the diffusion region, and ideal MHD equations elsewhere.

In this same chapter, we defined magnetic reconnection as the fundamental process by which magnetic field lines of opposite polarity reconfigure to a lower energy state, explosively converting magnetic energy to particle energy. This process was described in detail and we also presented the Dungey Cycle, which explains the magnetospheric dynamics from magnetic reconnection between the interplanetary and terrestrial magnetic fields. Later, the expression *reconnection rate* was described and the *diffusion region* was introduced. We also introduced some theoretical models of magnetic reconnection, giving special attention to the Sweet-Parker model, which is considered as the simplest way of describing magnetic reconnection. Finally, we discussed the reconnection rate problem as the main motivation for this study.

In order to obtain the data needed for the analysis, we used a 2.5D resistive MHD simulation based on a simple Harris sheet equilibrium. In Chapter 3, we introduced in detail the setup of our simulation. Some characteristics of the code were presented, such as the size of our domain, the boundary and initial conditions, and the location and form of the resistive spot. The code solves the MHD equations in the conservational form, and the

equations were presented together with a detailed explanation of the integration method used to solve them.

The analysis was made out of a total of 31 runs that were split into 2 different studies. In Chapter 4, we first showed the general behaviour of a sample run to demonstrate how the ensemble of runs are analysed. Here, we described the time evolution of the current density and we plotted the components of the velocity together with the magnetic energy and pressure. These plots provided evidence of how, during magnetic reconnection, magnetic energy is being converted to kinetic and thermal energy. By analysing the two different components of the resistive Ohms law around the diffusion region, we showed that outside the diffusion region, the term $\mathbf{v} \times \mathbf{B}$ dominates, while the resistive term is the only contributor to E_y at the center. Then, we presented the results corresponding to our two studies.

In the first study, we investigated 16 different values for the magnitude of the resistivity (η_1), keeping its aspect ratio constant. The amount of reconnected flux for each of the η_1 values was plotted together with the variation of the reconnection rate. We found that the reconnection rate increases with the magnitude of the resistivity, but only to a certain limit - most likely determined by macroscopic quantities such as the inflow speed, outflow speed or the opening angle. The system has the freedom to change the distribution of the magnetic field and, studying the current density profile and the contribution of the different terms of the induction equation, we concluded that, for large values of η_1, the gradient of the magnetic field is pushed towards the boundary of the resistivity, diffusing away from the center of the diffusion region. This implies a bifurcation of the current sheet, thereby restricting j_y at the center and preventing the reconnection rate from increasing.

The goal of the second study was to investigate the impact of changing the shape of the resistive spot on the reconnection rate. 16 additional runs were used for this objective. We noticed a clear trend in the increase of the reconnection rate as the aspect ratio was getting larger, but found that this trend did not hold for $L_x \lesssim 2$. Thus, the highest reconnection rate was found for $L_x = 2$. Studying the current density for this value of the aspect ratio, and 2 other values around it, as well as the contribution of the resistive terms to the profile of $\mathbf{B}$, we concluded that, for aspect ratios smaller than 2, the gradient of η is so sharp that the x-component of the magnetic field (B_x) is converted into B_z. The induction of B_z in the diffusion region is governed by the resistive terms in the induction equation. Due to the limited extent of the resistivity in the x-direction (for small values of L_x), B_z must be induced over a small finite region. The associated current density effectively reduces the j_y component at the center, which reflects the reduction of the reconnection rate by $E_y = \eta j_y$.

Later, we related this variation in the components of the magnetic field to a deformation of the field lines near the X point, and we compared the shape of the field lines for 4 different values of L_x. We could verify how the opening angle of the separatrix is related to the shape of the resistive spot, and that the largest opening angle ($\simeq 15°$) corresponded to the aspect ratio with a fastest reconnection rate. We also noticed that the largest opening

angle corresponded to the smallest aspect ratio inside the diffusion region, but this does not happen at larger scales, which suggested that the opening angle is not only determined by local microscopic properties, but also by larger scales effects.

In Chapter 6, we discussed three different characteristics of our simulation which are of special interest or concern. First, we discussed the property of MHD simulations that allow us to work in dimensionless units. Here, we obtained proof that keeping an invariant Lundquist number in runs with different resistivities, results in a similar reconnection rate if we also keep the rate between all the necessary quantities, such as the current sheet width or the time scale. Second, we discussed the grid resolution of our simulation domain. We showed that increasing the resolution has no significant impact on the reconnection rate and concluded that the resolution used is sufficient. Finally, we discussed the time resolution. We compared two different runs with different time resolutions and showed that the time resolution used in our simulations is more than adequate.

Let's summarize the findings of our analysis:

- The effectivenes of the reconnection process increases with the magnitude of the resistivity, but only to a certain limit which is most likely determined by larger-scale system properties.

- The distribution of the system undergoes major changes near the diffusion region when increasing the magnitude of the resistivity. These include the displacement of the magnetic field gradient to the edges of the diffusion region, decreasing the current density in the center and preventing an increase in the reconnection rate.

- The peak reconnection rate corresponds to an optimal aspect ratio value of the resistive spot. This corresponds to a value of $L_x = 2$ (for $L_z = 1$).

- For $L_x > 2$, the tension force decreases with increasing L_x, reducing the outflow speed and the reconnection rate.

- For $L_x < 2$, the gradient of η in the x-direction is so sharp that B_x is too rapidly converted to B_z, reducing j_y at the center and decreasing the reconnection rate.

- The opening angle of the outflow magnetic field lines is strongly tied to the shape of the diffusion region.

- Inside the resistive region, a smaller aspect ratio corresponds to a larger opening angle.

- Outside the diffusion region, the largest opening angle is reached for the peak rate ($L_x = 2$).

6.1 Key Findings

To end this chapter, we present the main key findings of this thesis.

The present study shows that:

- Even when inserting very strong resistive spots with varying shapes, there appears to be a maximum rate of reconnection the system can support.
- A sub-optimal choice of resistivity magnitude or shape of the resistive spot leads to lower overall reconnection rates.

These results have two important implications:

- The reconnection rate depends significantly on properties of the diffusion region, even if the size of that region is much smaller than the system. This is a new insight, which may be a counterpoint to the assertion that the reconnection rate is independent on the diffusion region physics.
- Even though this has not been proven strictly, there are very strong indications that there is a maximum reconnection rate, which cannot be exceeded irrespective of the diffusion region physics. It appears exceedingly likely that this rate limitation is due to larger-scale system properties rather than properties of the diffusion region.

Chapter 7

Future Work

7.1 Coupling between large and small scales

We have presented strong indications that a maximum reconnection rate exists. This rate cannot be exceeded even when we allow the field to diffuse much quicker than it can be transported into the region. Thus, larger-scale properties must play a controlling role in limiting the allowed rate. However, no strict proof has been presented, and there is still a lot of work to do in order to achieve a better understanding of the coupling between large and small scales.

Since the reconnection rates found in this thesis are on the same order as the peak rates found in particle models, this suggests that our current framework is applicable for studying these large-scale limitation as well. This large-scale process limiting the rate could be related to how the systems freedom resolves an optimum opening angle, as discussed in Section 4.3.2, which in turn suggests that the maximum outflow velocity allowed is somehow restricted. Such an investigation is a formidable task, but we now have the necessary tools to pursue such a challenge.

7.2 Three-dimensional MHD

The present study uses a 2.5D resistive MHD model to perform the analysis. A natural extension of our investigation is to perform three-dimensional simulations to determine whether this enhanced freedom results in a similar limitation of the reconnection rate.

Can we achieve the same rates in 3D, if not - what limits the rate? What is the most efficient resistive shape in 3D?

7.3 Beyond resistive MHD

Our current resistive MHD scheme represents the simplest model that can be used to study magnetic reconnection self-consistently. It has the advantage that we can easily control the magnitude and shape of the diffusion region, in addition to being computationally cheap. However, kinetic effects beyond two-fluid descriptions cannot be described by fluid models, and other models such as Particle-In-Cell (PIC) simulations must be used for these purposes. Thus, it could bring some better understanding to the matter to extend this study to kinetic plasmas.

7.4 Related studies

A prediction model incorporating both magnitude and shape of the diffusion region could be developed. Such a model could quantify how the different shapes and magnitude unified influences the efficiency of magnetic reconnection. Such an analysis, which would require many additional simulations, could further optimize the peak reconnection rate.

Bibliography

Akasofu, S.-I. (1964), The development of the auroral substorm, *Planetary and Space Science*, *12*(4), 273–282, doi:https://doi.org/10.1016/0032-0633(64)90151-5.

Alfven, H. (1940), On the motion of a charged particle in a magnetic field, *Ark. Mat. Astron. Fys. Swedish Academy of Science*, *27A*.

Alfvén, H. (1942), Existence of Electromagnetic-Hydrodynamic Waves, *Nature*, *150*(3805), 405–406, doi:10.1038/150405d0.

Baumjohann, W., and R. A. Treumann (2012), *Basic Space Plasma Physics*, revised ed., Imperial College Press, doi:10.1142/P850.

Birn, J. (1980), Computer studies of the dynamic evolution of the geomagnetic tail, *Journal of Geophysical Research: Space Physics*, *85*(A3), 1214–1222, doi:https://doi.org/10.1029/JA085iA03p01214.

Birn, J., and M. Hesse (2005), Energy release and conversion by reconnection in the magnetotail, *Annales Geophysicae*, *23*, 3365–3373, doi:10.5194/angeo-23-3365-2005.

Birn, J., and E. W. Hones Jr. (1981), Three-dimensional computer modeling of dynamic reconnection in the geomagnetic tail, *Journal of Geophysical Research: Space Physics*, *86*(A8), 6802–6808, doi:https://doi.org/10.1029/JA086iA08p06802.

Birn, J., R. Sommer, and K. Schindler (1975), Open and closed magnetospheric tail configurations and their stability., *apss*, *35*(2), 389–402, doi:10.1007/BF00637005.

Birn, J., M. Hesse, and K. Schindler (1996), Mhd simulations of magnetotail dynamics, *Journal of Geophysical Research: Space Physics*, *101*(A6), 12,939–12,954, doi:https://doi.org/10.1029/96JA00611.

Birn, J., J. F. Drake, M. A. Shay, B. N. Rogers, R. E. Denton, M. Hesse, M. Kuznetsova, Z. W. Ma, A. Bhattacharjee, A. Otto, and P. L. Pritchett (2001), Geospace environmental modeling (GEM) magnetic reconnection challenge, *Journal of Geophysical Research: Space Physics*, *106*(A3), 3715–3719, doi:https://doi.org/10.1029/1999JA900449.

Biskamp, D. (1986), Magnetic reconnection via current sheets, *Physics of Fluids*, *29*(5), 1520–1531, doi:10.1063/1.865670.

Burch, J. L., and R. B. Torbert (2016), *Magnetospheric Multiscale: A Mission to Investigate the Physics of Magnetic Reconnection*, Springer.

Burch, J. L., T. E. Moore, R. B. Torbert, and B. L. Giles (2016), Magnetospheric Multiscale Overview and Science Objectives, *Space Science Reviews*, *199*(1-4), 5–21, doi: 10.1007/s11214-015-0164-9.

Cai, H. J., and L. C. Lee (1997), The generalized Ohm's law in collisionless magnetic reconnection, *Physics of Plasmas*, *4*(3), 509–520, doi:10.1063/1.872178.

Cassak, P. A., Y.-H. Liu, and M. A. Shay (2017), A review of the 0.1 reconnection rate problem, *Journal of Plasma Physics*, *83*(5), 715830,501, doi:10.1017/S0022377817000666.

Chen, F. F., and H. Torreblanca (2006), Introduction to plasma physics and controlled fusion, 2nd edition.

Comisso, L., and A. Bhattacharjee (2016), On the value of the reconnection rate, *Journal of Plasma Physics*, *82*(6), 1–10, doi:10.1017/S002237781600101X.

Dungey, J. W. (1961), Interplanetary magnetic field and the auroral zones, *Physical Review Letters*, *6*, 47–48, doi:10.1103/PhysRevLett.6.47.

Gekelman, W., P. Pribyl, Z. Lucky, M. Drandell, D. Leneman, J. Maggs, S. Vincena, B. Van Compernolle, S. K. P. Tripathi, G. Morales, T. A. Carter, Y. Wang, and T. DeHaas (2016), The upgraded large plasma device, a machine for studying frontier basic plasma physics, *Review of Scientific Instruments*, *87*(2), 025,105, doi:10.1063/1.4941079.

Giovanelli, R. G. (1947), Magnetic and Electric Phenomena in the Sun's Atmosphere associated with Sunspots, *Monthly Notices of the Royal Astronomical Society*, *107*(4), 338–355, doi:10.1093/mnras/107.4.338.

Goldston, R. J., and P. H. Rutherford (1995), *Introduction to Plasma Physics*, Plasma physics laboratory Princeton University.

Gonzalez, W., and E. Parker (2016), *Magnetic Reconnection: Concepts and Applications*, vol. 427, Springer, doi:10.1007/978-3-319-26432-5.

Gonzalez, W. D., J. a. Joselyn, Y. Kamide, H. W. Kroehl, G. Rostoker, B. T. Tsurutani, and V. M. Vasyliunas (1994), What is a geomagnetic storm?, *Journal of Geophysical Research*, *99*(A4), 5771, doi:10.1029/93JA02867.

Huang, Y.-M., and A. Bhattacharjee (2013), Plasmoid instability in high-lundquist-number magnetic reconnection, *Physics of Plasmas*, *20*, 055,702, doi:10.1063/1.4802941.

Ji, H., and W. Daughton (2011), Phase diagram for magnetic reconnection in heliophysical, astrophysical, and laboratory plasmas, *Physics of Plasmas*, *18*(11), 111,207, doi: 10.1063/1.3647505.

Ji, H., T. Carter, S. Hsu, and M. Yamada (2001), Study of local reconnection physics in a laboratory plasma, *Earth and Planetary Science Letters - EARTH PLANET SCI LETT*, *53*, 539–545, doi:10.2172/786575.

Klimontovich, Y. (1969), The statistical theory of non-equilibrium processes in a plasma, *MIT Press*.

Kulsrud, R. (2001), Magnetic reconnection: Sweet-parker versus petschek, *Earth, Planets and Space*, *53*, doi:10.1186/BF03353251.

Kuznetsova, M. M., M. Hesse, L. Rastätter, A. Taktakishvili, G. Toth, D. L. De Zeeuw, A. Ridley, and T. I. Gombosi (2007), Multiscale modeling of magnetospheric reconnection, *Journal of Geophysical Research: Space Physics*, *112*(10), 1–15, doi:10.1029/2007JA012316.

Liu, Y.-H., M. Hesse, F. Guo, W. Daughton, H. Li, P. A. Cassak, and M. A. Shay (2017), Why does Steady-State Magnetic Reconnection have a Maximum Local Rate of Order 0.1?, *Physical Review Letters*, *118*(8), 1–6, doi:10.1103/PhysRevLett.118.085101.

McPherron, R. L. (1979), Magnetospheric substorms, *Reviews of Geophysics*, *17*(4), 657–681, doi:https://doi.org/10.1029/RG017i004p00657.

Parker, E. N. (1957a), Newtonian development of the dynamical properties of ionized gases of low density, *Physical Review*, *107*(4), 924–933, doi:10.1103/PhysRev.107.924.

Parker, E. N. (1957b), Sweet's mechanism for merging magnetic fields in conducting fluids, *Journal of Geophysical Research*, *62*(4), 509, doi:10.1029/JZ062i004p00509.

Parker, E. N. (1958a), Interaction of the Solar Wind with the Geomagnetic Field, *Physics of Fluids*, *1*(3), 171, doi:10.1063/1.1724339.

Parker, E. N. (1958b), Dynamics of the Interplanetary Gas and Magnetic Fields, *Astrophysical Journal*, *128*, 664.

Parker, E. N. (1963), The Solar-Flare Phenomenon and the Theory of Reconnection and Annihiliation of Magnetic Fields., *apjs*, *8*, 177, doi:10.1086/190087.

Parks, G. K. (2004), *Physics of space plasmas. An introduction.*, Advanced Book Program.

Petschek, H. E. (1964), Magnetic Field Annihilation, in *NASA Special Publication*, vol. 50, p. 425.

Rostoker, G., S.-I. Akasofu, J. Foster, R. Greenwald, A. Lui, Y. Kamide, K. Kawasaki, and R. McPherron (1980), Magnetospheric substorms - definition and signatures, *Journal of Geophysical Research*, *85*, 1663–1668, doi:10.1029/JA085iA04p01663.

Russell, C. T. (1972), The configuration of the magnetosphere, in *Critical Problems of Magnetospheric Physics*, vol. 1, edited by E. R. Dyer, Sol. Terr. Phys., Natl. Acad. of Sci. Washington, D.C.

Russell, C. T. (1993), Magnetic fields of the terrestrial planets, *Journal of Geophysical Research: Planets*, *98*(E10), 18,681–18,695, doi:https://doi.org/10.1029/93JE00981.

Russell, C. T. (2000), The solar wind interaction with the Earth's magnetosphere: a tutorial, *IEEE Transactions on Plasma Science*, *28*(6), 1818–1830, doi:10.1109/27.902211.

Schindler, K. (1972), A self-consistent theory of the tail of the magnetosphere, in *Earth's Magnetospheric Processes*, edited by B. M. McCormac, pp. 200–209, Springer Netherlands, Dordrecht.

Shay, M. A., J. F. Drake, B. N. Rogers, and R. E. Denton (1999), The scaling of collisionless, magnetic reconnect ion for large systems, *Geophysical Research Letters*, *26*(14), 2163–2166, doi:10.1029/1999GL900481.

Sonnerup, B. (1970), Magnetic-field re-connexion in a highly conducting incompressible fluid, *Journal of Plasma Physics*, *4*(1), 161–174, doi:10.1017/S0022377800004888.

Sweet, P. A. (1958), The Neutral Point Theory of Solar Flares, in *Electromagnetic Phenomena in Cosmical Physics*, vol. 6, edited by B. Lehnert, p. 123.

Tóth, G., I. Sokolov, T. Gombosi, D. R. Chesney, C. Clauer, D. D. Zeeuw, K. Hansen, K. Kane, W. Manchester, R. Oehmke, K. G. Powell, A. Ridley, I. Roussev, Q. Stout, O. Volberg, R. Wolf, S. Sazykin, A. Chan, T. Yu, and J. Kóta (2005), Space weather modeling framework: A new tool for the space science community, *Journal of Geophysical Research*, *110*.

Tóth, G., B. van der Holst, I. V. Sokolov, D. L. De Zeeuw, T. I. Gombosi, F. Fang, W. B. Manchester, X. Meng, D. Najib, K. G. Powell, Q. F. Stout, A. Glocer, Y.-J. Ma, and M. Opher (2012), Adaptive numerical algorithms in space weather modeling, *Journal of Computational Physics*, *231*(3), 870–903, doi:https://doi.org/10.1016/j.jcp.2011.02.006, special Issue: Computational Plasma Physics.

Ugai, M., and T. Tsuda (1977), Magnetic field-line reconnexion by localized enhancement of resistivity: Part 1. evolution in a compressible mhd fluid, *Journal of Plasma Physics*, *17*(3), 337–356, doi:10.1017/S0022377800020663.

Vasyliunas, V. M. (1975), Theoretical Models of Magnetic Field Line Merging , 1, *Reviews of Geophysics and Space Physics*, *13*(1), doi:10.1029/RG013i001p00303.

Vasyliunas, V. M. (2005), Time evolution of electric fields and currents and the generalized Ohm's law, *Annales Geophysicae*, *23*(4), 1347–1354, doi:10.5194/angeo-23-1347-2005.

Yeh, T., and W. Axford (1970), On the re-connexion of magnetic field lines in conducting fluids, *Journal of Plasma Physics*, *4*, 207–229.

Zenitani, S., M. Hesse, and A. Klimas (2009), Two-fluid magnetohydrodynamic simulations of relativistic magnetic reconnection, *The Astrophysical Journal*, *696*(2), 1385–1401, doi: 10.1088/0004-637x/696/2/1385.